

OPTICAL PROPERTIES OF WIDE BANDGAP III-NITRIDE-
AND ZINC OXIDE-BASED EPILAYERS,
ALLOYS, AND HETEROSTRUCTURES

By

BRIAN DEAN LITTLE

Bachelor of Arts in Physics
Hendrix College
Conway, Arkansas
1994

Master of Science in Photonics
Oklahoma State University
Stillwater, Oklahoma
1997

Submitted to the Faculty of the
Graduate College of the
Oklahoma State University
in partial fulfillment of
the requirements for
the Degree of
DOCTOR OF PHILOSOPHY
December, 2000

COPYRIGHT


By

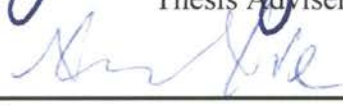
Brian Dean Little

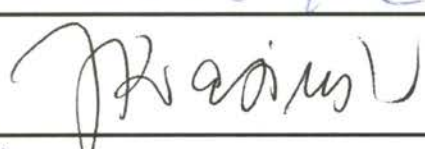
December, 2000

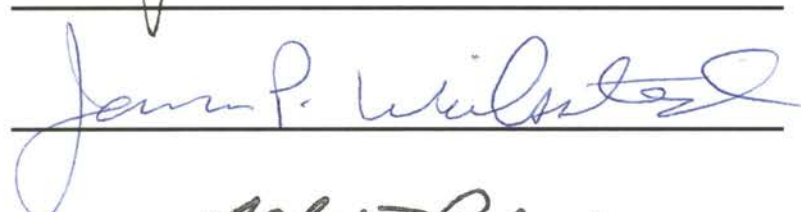
OPTICAL PROPERTIES OF WIDE BANDGAP III-NITRIDE-
AND ZINC OXIDE-BASED EPILAYERS,
ALLOYS, AND HETEROSTRUCTURES


Thesis Approved:



Thesis Adviser








Dean of the Graduate College

ACKNOWLEDGEMENTS

First and foremost, I would like to thank my advisor, Dr. Jin-Joo Song, for her support during my years in graduate school. She provided me with the working environment to perform experiments on state-of-the-art samples using top-of-the-line equipment. Her expertise has prepared me well for my professional future. I would also like to thank the members of my advisory committee for the time and guidance they have provided me: Dr. Jim Wicksted, Dr. Xin-Cheng Xie, and Dr. Jerzy Krasinski.

I would like to sincerely thank Dr. Wei Shan, whose unparalleled skill in the lab provided me with a solid foundation for my research. I would also like to thank Mike Lucas of the OSU Physics and Chemistry Machine Shop for his proficiency in making all the bizarre little odds and ends I needed from time to time. My great appreciation goes to the secretaries in the Physics Department and the CLPR who make life so much easier for all of us on a daily basis, especially Carol Wicksted and Susan Cantrell.

I owe a huge debt of gratitude to the Physics Department at Hendrix College for the excellent preparation I received during my undergraduate years. Dr. Richard Rolleigh, Dr. Pradip Bandy, and Dr. Robert Dunn are all outstanding educators and talented scientists.

I would like to express my thanks to all of Dr. Song's students and postdocs who have helped me in many diverse ways over the years: Dr. Seon-Ju Hwang, Dr. Gil-Han Park, Dr. Yong Hoon Cho, Dr. Yong Hwan Kwon, Dr. Bahman Taheri, Dr. John Hays, Dr. Xiao-Hua Yang, Dr. Sang Kee Shee, Gordon Gainer, Jack Lam, Chan-Kyung Choi, and Tomoya Sugahara. Dr. Art Fischer and Dr. Ted Schmidt deserve special thanks for showing me the ropes, teaching me how to be a successful physicist, being great friends, and putting up with my antics over the years. Graduate school would not have been as much fun without them.

I would like to acknowledge the vital role my friend, roommate, and colleague Dr. Serge (or is it Sergiy?) Bidnyk has played in my education. We have learned much from each other during our time in Stillwater, and contrary to popular belief, I believe we are both the better for it.

There are many other people worth mentioning who made my life at OSU much more interesting: Ulf Nobbmann, Fritz Fedler, Mark O'Steen, Von Whitley, Dr. John Gelder, Jeromy Rezac, Dr. Scott Stoodley, Dr. Chris Schult, Brandon Neal, Stephen King, and Xu Sheng just to name a few.

I would be remiss not to acknowledge my best group of friends in the world for all the support and encouragement they have given me. Dr. Chris and Kirsten Collins, Dr. Adam and Heather Gray, Lee and Samantha Harrison, and Mark and (soon-to-be) Laurence Sandoval. I wouldn't have gotten where I am without their friendship. They allowed me to get away from the hustle and bustle of graduate school whenever I needed to and always make me feel truly at ease. The great memories I have of our time together have helped me make it through some pretty tough times.

Finally, I would like to thank the two people who made this possible: my mom and dad. I will never be able to sufficiently express to them my thanks for everything they have given me. I love them with all my heart, and this thesis is dedicated to them.

TABLE OF CONTENTS

Chapter	Page
I. INTRODUCTION	1
History of GaN Research.....	9
History of ZnO Research	13
Organization of This Thesis.....	16
Important Definitions.....	18
List of Acronyms	19
List of Constants and Symbols	21
II. GENERAL PROPERTIES OF THE III-NITRIDES AND ZnO, GROWTH METHODS, AND IMPORTANT DEVICE STRUCTURES	23
Crystal Properties.....	23
Band Structure and Alloys	29
Growth Techniques.....	38
Structures	40
III. EXPERIMENTAL METHODS USED TO CHARACTERIZE WIDE BANDGAP SEMICONDUCTORS	47
Photoluminescence	48
Temperature Dependent PL	49
Power Dependent PL	51
Pressure Dependent PL	52
Time-Resolved PL	53
Photoluminescence Excitation	54
Absorption.....	60
Reflectance.....	67
Photoreflectance.....	68
Photoconductivity	74
Stimulated Emission and Lasing.....	79
IV. EXCITONS IN GaN.....	85
Binding Energy for the Intrinsic Excitons in Wurtzite GaN.....	85

Excitons and Strain in GaN Epilayers	92
Excitonic Photoconductivity in GaN Epilayers	97
V. EXPERIMENTAL INVESTIGATIONS OF III-NITRIDE ALLOYS AND HETEROSTRUCTURES	101
Optical Properties of $\text{In}_x\text{Ga}_{1-x}\text{N}$ Alloys	101
High Pressure Studies of the III-Nitrides	110
Dynamics of Photoexcited Carriers in AlGaN/GaN Double Heterostructures	120
Excitation Wavelength Dependence of Stimulated Emission/Lasing from AlGaN/GaN Separate Confinement Heterostructures	130
Comparison of Emission from Highly Excited (In,Al)GaN Thin Films and Heterostructures	140
VI. EXPERIMENTAL INVESTIGATIONS OF ZnO	145
Comparison of the Structural and Optical Properties of Bulk and Epitaxial ZnO Crystals	146
Stimulated Emission Properties of ZnO	153
VII. SUMMARY	156
BIBLIOGRAPHY	159
APPENDICES	169
APPENDIX A – PUBLICATIONS AND PRESENTATIONS	170
APPENDIX B – LASER INDUCED EPITAXIAL LIFTOFF	176

LIST OF TABLES

Table	Page
I. World market forecast for high temperature electronics by semiconductor type.....	7
II. Fundamental properties of the III-Nitrides and ZnO	26

LIST OF FIGURES

Figure	Page
1. Conversion chart between units commonly used to describe the color of light in the range of interest of this thesis	8
2. Schematic of the wurtzite crystal structure.....	27
3. Bandgap energy versus lattice constant for several important semiconductors	28
4. Band structure of wurtzite GaN.....	35
5. First Brillouin zone of a wurtzite crystal lattice.....	36
6. Structure and symmetries of the lowest conduction band and the uppermost valence bands in wurtzite GaN at the Γ point.....	37
7. Schematic diagram of single and multiple quantum well structures	43
8. Schematic design of a GaAs/AlGaAs double heterostructure	44
9. Schematic drawing and energy-band diagram of a typical separate confinement heterostructure.....	45
10. Several important semiconductor device structures: (a) multiple quantum well SCH, (b) graded-index SCH, (c) ridge waveguide LD, and (d) buried-heterostructure LD	46
11. Typical experimental setups for PL and PLE measurements	56
12. Schematic of surface and edge emitting geometries.....	57
13. Temperature dependence of the excitonic PL emission from a 7.2 μm GaN epilayer grown on sapphire by MOCVD	58
14. Typical time-resolved PL experimental setup	59

15. Experimental setups for the measurement of absorption, reflectance, and photoreflectance	63
16. Absorption spectra of a 0.38 μm -thick GaN sample at selected temperatures from 100 K to 475 K.....	64
17. Theoretical fit to the 10 K absorption spectra of a 0.38 μm GaN epilayer.....	65
18. Absorption spectra for 50 nm and 100 nm InGaN epilayers at RT and 10 K.....	66
19. 10 K reflectance data from a 3 μm GaN epilayer and RT reflectance taken from a 1.9 μm GaN epilayer	71
20. Refractive index at RT for several GaN films of different thickness grown on sapphire by MOCVD	72
21. PR spectra of an $\text{In}_{0.13}\text{Ga}_{0.87}\text{N}$ epilayer as a function of temperature	73
22. Typical setup for the measurement of photoconductivity.....	76
23. Typical results of photoconductivity measurements.....	77
24. Photoconductivity spectra for GaAs epitaxial layers of various thickness.....	78
25. Typical stimulated emission/lasing experimental setup	82
26. SE spectrum of a 4.2 μm GaN sample at various excitation intensities above the SE threshold	83
27. RT stimulated and spontaneous emission spectra from an InGaN/GaN MQW sample	84
28. 10 K reflection spectra taken near the bandedge of a 7.2 μm GaN/sapphire sample, a 4.2 μm GaN/sapphire sample, and a 3.7 μm GaN/SiC sample	90
29. 10 K PR spectra taken from a 7.2 μm GaN/sapphire sample and 3.7 μm GaN/SiC sample.....	91
30. The measured in-plane GaN lattice constant (a) versus the lattice constants in the growth direction (c).....	95
31. The measured free-exciton transition energies from the GaN samples used in this work as a function of strain in the growth direction and relative in-plane (biaxial) strain	96

32. Comparison of 10 K PC and PL data from a 0.4 μm GaN epilayer and absorption from a 0.38 μm GaN epilayer grown on sapphire by MOCVD.....	99
33. Photoconductivity spectrum of a 0.4 μm GaN epilayer (bottom) and a fit to this data using Equation 3-15 (bottom).....	100
34. PR (upper curve) and PL (lower curve) spectra of an $\text{In}_{0.14}\text{Ga}_{0.86}\text{N}$ sample at 10 K	106
35. Temperature dependence of the interband transition energy of the $\text{In}_{0.14}\text{Ga}_{0.86}\text{N}$ sample.....	107
36. Bandgaps of various samples measured by PR at 10 K and RT vs. their alloy concentrations	108
37. Temporal variation of the alloy PL peak for an $\text{In}_{0.08}\text{Ga}_{0.92}\text{N}$ sample at selected temperatures	109
38. 10 K PL spectrum taken from an $\text{Al}_{0.35}\text{Ga}_{0.65}\text{N}$ epitaxial layer at atmospheric pressure	115
39. Near-bandedge PL from the $\text{Al}_{0.35}\text{Ga}_{0.65}\text{N}$ sample at selected pressures.....	116
40. Peak position of the PL emission from an $\text{Al}_{0.05}\text{Ga}_{0.95}\text{N}$ sample as a function of applied pressure at RT	117
41. 10 K PL spectra of the InGaN alloy samples at atmospheric pressure.....	118
42. Pressure dependence of the near-bandedge PL transition energy at 10 K for the InGaN alloys and GaN.....	119
43. 10 K PL spectra taken from an $\text{Al}_{0.03}\text{Ga}_{0.97}\text{N}/\text{GaN}$ DH grown on sapphire (top) and an $\text{Al}_{0.1}\text{Ga}_{0.9}\text{N}/\text{GaN}$ DH grown on SiC (bottom)	126
44. PL of an $\text{Al}_{0.03}\text{Ga}_{0.97}\text{N}/\text{GaN}$ DH grown on sapphire, showing the fast quenching of the GaN-related luminescence signal with increasing temperature.....	127
45. Temporal evolution of the spectrally integrated PL for the AlGaN cladding and GaN active regions of an $\text{Al}_{0.1}\text{Ga}_{0.9}\text{N}/\text{GaN}$ DH sample grown on SiC at 10 K.....	128
46. Temporal evolution of the spectrally integrated PL for the AlGaN cladding and GaN active regions of an $\text{Al}_{0.03}\text{Ga}_{0.97}\text{N}/\text{GaN}$ DH sample grown on sapphire at 10 K.....	129
47. 10 K PL of the AlGaN/GaN SCH.....	134

48. Typical RT lasing spectrum of the AlGaIn/GaN SCH structure.....	135
49. Typical 10 K lasing spectra of the SCH.....	136
50. Power dependence of the luminescence from the SCH at 10 K, showing the onset of lasing	137
51. Results of various experiments on the SCH sample at RT	138
52. SE/lasing at RT seen simultaneously from the GaN buffer layer and the active region for a near-resonant pumping wavelength.....	139
53. RT SE spectra at pump intensities above and below the SE threshold, I_{th} , for AlGaIn layers with alloy concentrations of (a) 17% and (b) 26%	143
54. Power dependence of the SE from the AlGaIn alloy samples at RT	144
55. Temperature dependent PL of a ZnO epilayer grown on sapphire with no buffer layer.....	148
56. 5 K PL spectrum of a ZnO epilayer grown by MBE using a MgO buffer layer .	149
57. PL spectra of a bulk ZnO crystal at selected temperatures from 10 to 110 K	150
58. XRD results from a ZnO epilayer grown on sapphire by MBE	151
59. XRD results from a bulk ZnO crystal	152
60. Spectra of ZnO epilayers at RT for several pumping intensities above and below the SE threshold	154
61. Integrated intensity of the RT emission from ZnO epilayers vs. pump intensity .	155
B-1. Illustration of the laser induced epitaxial liftoff process	179

CHAPTER I

INTRODUCTION

The group-III Nitrides, including of the binary compound Gallium Nitride (GaN) and its alloys with Indium Nitride (InN) and Aluminum Nitride (AlN), have received an incredible amount of attention over the past few years. Much of this attention is due to the recent realization of high brightness blue and green light emitting diodes (LEDs) and violet laser diodes (LDs), all of which use InGaN alloy active regions.¹ InGaN-based LEDs have found applications in large outdoor full color displays, where they provide the green and blue components of the required RGB color scheme (red-green-blue), and also in traffic lights, where the electrical power consumption is only 1/10 that of incandescent bulbs and the lights are brighter, more directional, and last 1000× longer.[‡] The violet LDs, which are expected to become commercially available in the near future (engineering samples were distributed in 1999), are anticipated to have a plethora of innovative uses. The most notable examples include high-density optical data storage and high-resolution printing, both of which take advantage of the fact that the shorter wavelength of the violet LDs can be focused to a smaller spot size in comparison to conventional red LDs.

According to a recent report by Elsevier Advanced Technology (Oxford, UK),² the market for GaN and related wide bandgap materials in the near future will be dominated by optoelectronic devices. The 1999 market for blue-green LEDs was \$325

[‡] As evidence of the significantly increased efficiency of LED-based traffic lights compared to filament light bulbs, Traffic Technology Inc. of Scottsdale, AZ has recently offered to provide their Unilight LED traffic signals free to every city, state, and county in the US in exchange for the money saved on energy costs during the first five years of operation. These savings have been estimated at \$1000 per year per intersection.

million, whereas that for violet diode lasers was \$46 million, and the white LED market was already worth \$88 million. By 2004, these numbers are expected to have grown to \$614 million, \$87 million and \$270 million, respectively. The market for these products is growing at a rate of over 20% per year. In addition, this estimate may be conservative because devices such as white LEDs and violet laser diodes are in the early part of their growth cycle and are expected to show very strong growth rates.

The optical storage market consumed over 260 million lasers in 1998, making it by far the biggest commercial application for LDs. This figure was expected to top 300 million in 1999, and there is no indication of this market slowing down in the foreseeable future. The technology used for reading data from CDs, which has been in place for over 10 years now, employs 780 nm AlGaAs LDs to read a feature size of 1.6 μm , allowing a maximum capacity of 650 MB on a single disk. The next generation of optical data storage is the DVD, which uses 650 nm AlGaInP LDs to read 0.74 μm features, with a maximum capacity of 4.7 GB. The next generation of DVDs, to be called HD-DVDs, will use 410 nm InGaN or second harmonic generation (SHG - see below) LDs. These violet LDs will allow the feature size to be shrunk down to 0.24 μm , thereby increasing the maximum single-side capacity of HD-DVDs to 15 GB. The main competitor for the InGaN/GaN material system in the development of violet/blue LDs for the optical data storage market is the SHG LD, which has been around for several years.³ Matsushita's version of this laser uses an Mg-doped LiNbO₃ waveguide to frequency-double the output from a 100 mW distributed Bragg reflector (DBR) laser at 850 nm. The second harmonic output at 425 nm has a power of 15 mW. This doubled DBR setup has a couple of advantages over the III-Nitride-based LD: (1) it is an established technology, and (2) it is easier to tightly focus onto the surface of the disk. Even though SHG LDs have been available to optical storage manufacturers for some time, they have not made a significant impact on the market. Most of the major manufacturers have been holding out for III-Nitride LDs because of their superiority over SHG LDs in several key aspects. First, III-Nitride-based LDs are more compact than the SHG lasers, and are better suited to mass production. Secondly, the SHG device requires precise adjustment of the laser source and the waveguide. Finally, the optical head in a typical DVD player is usually

budgeted at 5-10% of the total system cost, which means the laser must make up only 1-2%. It is unlikely that SHG LDs can meet this low-cost criterion in the near-term.

In addition to these core applications for Nitride-based optoelectronic devices, a variety of other novel uses are envisioned for these materials. They include high temperature/power/frequency electronics, field emission devices (*e.g.* flat-panel displays with enhanced durability, brightness, and viewing angle), underwater and satellite-to-satellite communications, environmental and chemical sensing, and medical applications. Table I, which forecasts the market for high temperature electronics from 1998 to 2008, illustrates the huge market potential for III-Nitride-based devices. In the high power/frequency electronics arena, GaN-based high electron mobility transistors (HEMTs – used in wireless communications applications such as cellular phones) have recently been produced with output powers up to 40 W at a frequency of 10 GHz by Cree, Inc.⁴ GaN-based HEMTs have an intrinsic advantage over other materials due to their extremely high breakdown voltage. While GaAs-based devices are only capable of a maximum microwave output power of 1.5 W/mm and those based on SiC can reach 4.3 W/mm, GaN-based devices can achieve up to 9.8 W/mm.⁵ In the same report, Cree announced the first GaN monolithic microwave integrated circuit (MMIC), with a pulsed radio frequency (rf) output power of 20 W at 9 GHz, exceeding the highest rf output power of GaAs MMICs. AlGaIn HEMTs, which are more robust than their GaN cousins, are currently capable of operating at a modulation frequency of 30 GHz, but this is expected to increase to 50 GHz in the near future. White LEDs, which can be created by coating a blue LED with a broadband yellow-emitting phosphor, have great potential to capture a significant portion of the global lighting market, which is currently valued at a staggering \$12 billion per year. In spite of the costly initial investment, the increased electrical efficiency and long lifetime of white LEDs compared to filament light bulbs allow a significant reduction in operating costs over time.

Another area in which the III-Nitrides have already proven themselves an important material system is that of photodetectors (PDs). Rather than have an applied electrical current cause the emission of light, as in an LED or LD, a PD absorbs light and produces a current proportional to the absorbed light intensity. By choosing an appropriate material for the absorption region, the PD can be made sensitive only to

ultraviolet (UV) light. Furthermore, by tuning the absorption to a specific band of wavelengths in the UV that is absorbed in Earth's upper atmosphere, the PD can be made insensitive to sunlight. This is called a "solar-blind" device. The AlGaIn alloy system, described in detail in later sections, is perfectly suited to this application. Since no photons with the detection wavelength can penetrate the atmosphere, any photons detected – and hence any current produced – by the PD must be of terrestrial origin. To achieve this performance in other material systems, complicated and expensive filter systems must be employed. Solar-blind PD technology is very useful to the military for tracking aircraft and missiles. These devices have become commercially available only in the past couple of years, and are now readily available from a variety of different companies dealing in photonics equipment.

Many of the above-mentioned technologies are in the early stages of development and new applications and techniques based on the III-Nitrides are constantly being introduced. Because of the sheer volume of research groups working with this material, it is difficult to envision what imaginative breakthroughs might be made in the near future. The group-III Nitrides represent an ever-increasingly active area of scientific research.

This chapter will give a short history of the research on the III-Nitrides that has led to the realization of practical Nitride-based optoelectronic devices, then give a history of research on a similar material - Zinc Oxide. Finally, the organization of this thesis will be described, followed by some *Important Definitions* that will be useful in later sections.

In this manuscript, several different formats will be used to describe the color of photons of light. This can be somewhat confusing at times, but is necessary for several reasons. First, different spectroscopic equipment is usually calibrated in different units. In a given experimental setup, the laser output might be expressed in wavelength, the width of the laser line in frequency, the spectrometer in inverse wavelength, and the response of the detector in photon energy. Secondly, the physical constants of semiconductors are often expressed in different units: phonon energies are given in inverse wavelength, bandgaps (described in detail in Chapter II) in photon energy, and lasing mode spacing in frequency. The most commonly used format in this thesis will be photon energy, which is defined as the energy one electron gains upon being accelerated

across a potential difference of one Volt. Photon energy is expressed in electron volts (eV), and is related to the basic SI unit of energy – the Joule (J) – by the following expression: $1 \text{ eV} = 1.602 \times 10^{-19} \text{ J}$. This choice of units makes life much easier for physicists dealing with semiconductor optoelectronics because it scales exactly with the bandgap energy. The next most common format will be wavelength (λ), usually expressed in nanometers ($1 \text{ nm} = 10^{-9} \text{ m}$). To switch between these two most common formats, we make use of (1) the equation giving the energy of a photon and (2) the simple relationship between wavelength and frequency, $c = \nu\lambda$, where c is the speed of light in a vacuum ($3 \times 10^8 \text{ m/s}$) and ν is the frequency in Hertz ($1 \text{ Hz} = 1 \text{ s}^{-1}$):

$$E = h\nu = hc/\lambda. \quad (1-1)$$

In this expression, E is the photon energy in eV and h is Planck's constant ($4.136 \times 10^{-15} \text{ eV}\cdot\text{s}$). In more usable form, this becomes:

$$E \text{ (in eV)} = 1239.8424 / \lambda \text{ (in nm)}. \quad (1-2)$$

A less commonly used unit is inverse wavelength, commonly referred to as wavenumber and expressed in units of cm^{-1} . To convert photon energy to wavenumber, Equation 1-2 transforms to:

$$E \text{ (in eV)} = \text{wavenumber (in cm}^{-1}\text{)} / 8065.5412. \quad (1-3)$$

Conversions between other units can be accomplished by combining the formulae given above. For convenience, a conversion chart between these units in the range of interest of this thesis is provided in Figure 1.

Temperatures will be presented in two different formats in this thesis. The first is the everyday Celsius or centigrade scale, measured in degrees ($^{\circ}\text{C}$), and defined by the freezing point (0°C) and boiling point (100°C) of pure water at sea level. However, the most commonly used temperature scale in much of the scientific community is the Kelvin, or absolute, temperature scale, which is measured in Kelvins (K). Kelvins have the same relative magnitude as degrees Celsius, but the zero point of this scale is set at the theoretically lowest temperature achievable in our universe: absolute zero (-273.15

$^{\circ}\text{C}$). Thus, the Kelvin scale is just the Celsius scale shifted upwards by 273.15 degrees. Water freezes at 273.15 K and boils at 373.15 K (note that there is no such thing as a negative temperature in the Kelvin scale). Room temperature (RT – usually taken to be 25°C) corresponds to 295.15 K, but is often rounded up to 300 K.

Device Type	Market (\$ million)		
	1998	2003	2008
Silicon, Silicon on insulator (SOI)	155.7	308.8	667.2
III-V Devices (GaAs, InAs, InSb)	20.6	60.8	183.2
Wide Bandgap Devices (GaN, SiC, diamond)	0.9	7.2	36.2
Total	177.2	376.8	887.1

Table I. World market forecast for high temperature electronics by semiconductor type. From Ref [6].

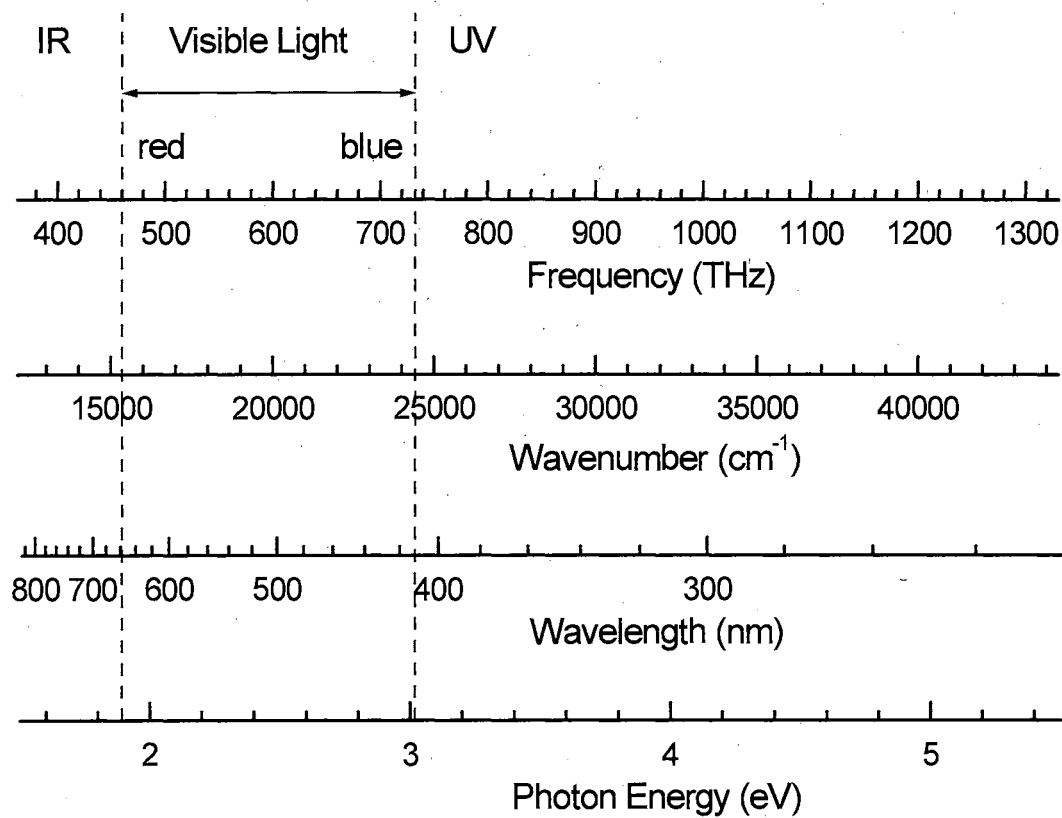


Figure 1. Conversion chart between units commonly used to describe the color of light in the range of interest of this thesis.

History of GaN Research

The first reports on GaN were published in 1971, and dealt with low quality metal-insulator-semiconductor LEDs fabricated by J. Pankove.⁷ These LEDs were not successfully commercialized because the quality of the layers was low and *p*-doping in this material had yet to be achieved.

In 1986, Akasaki *et al*⁸ achieved the successful growth of high quality GaN thin films by employing buffer layers between the substrate (sapphire in this case) and the epilayer, an idea first proposed by Yoshida *et al*.⁹ These buffer layers provide nucleation sites for the growth of GaN, which grows in the form of islands around the sites. The islands eventually coalesce and 2-dimensional (2D) growth occurs thereafter, giving rise to a high quality epitaxial film. This study showed that GaN could be grown with a quality sufficient to allow the further development of optoelectronic devices. However, there were still several large obstacles to overcome, the most daunting of which were related to doping and contact fabrication.

Perhaps the most crucial advance in III-Nitride research came in 1989 with the successful *p*-doping of GaN by Amano *et al*.¹⁰ When it is not intentionally doped with an extrinsic atomic species, GaN exhibits an intrinsic *n*-type conductivity due to the nature of the dislocations and imperfections present in the crystal structure. This background electron concentration is typically $[n] \sim 10^{18} \text{ cm}^{-3}$ and is thought to arise mainly from nitrogen vacancies in the III-Nitride crystal lattice (denoted by V_N). Early attempts to grow *p*-type GaN (*p*-GaN) were unsuccessful, resulting in highly resistive and compensated material. Amano *et al* discovered in 1988 that low-energy electron beam irradiation (LEEBI) somehow enhanced the blue luminescence signal from Mg-doped GaN films (denoted by GaN:Mg). Hall measurements revealed that the LEEBI treatment had activated the Mg dopants and created *p*-type material. Soon after the successful realization of *p*-GaN by Amano, the fabrication of a *p-n* junction LED was

demonstrated.¹¹ In 1992, Nakamura *et al* found that Mg was compensated by atomic hydrogen impurities in the crystal, and that the process of annealing the LEEBI-treated GaN:Mg in an N₂ environment could significantly decrease the resistivity of the sample.¹²

Early reports on making metallic contacts to GaN demonstrated success using as-deposited Al and annealed Au contacts.¹³ In conjunction with the ability to successfully grow a *p-n* junction, this allowed the first demonstration of a III-Nitride-based LED by Nakamura *et al*.¹⁴ This device was just a simple GaN *p-n* homojunction with a somewhat poor quality, but before long, traditional double heterostructure (DH) LEDs with significantly enhanced emission intensity were realized.¹⁵ These DHs employed an InGaN active region. For the long-lifetime high quality devices demonstrated more recently, lower contact resistivities achieved by using multilayer metallization schemes have been employed. For example, Nakamura *et al* consistently obtain good results using Ni/Au *p*-contacts and Ti/Al *n*-contacts on their devices.¹

Further refinements in growth techniques and device fabrication by Nichia Chemical Industries (who use sapphire substrates) and Cree Inc. (who use SiC substrates) resulted in the commercialization of high quality bright and efficient blue and green LEDs in the mid-1990s.⁶ However, short wavelength III-Nitride-based LDs were still out of reach. Nakamura *et al* from Nichia were the first to observe laser emission from a III-Nitride-based heterostructure; they used pulsed current injection in their experiments as opposed to optical pumping.¹⁶ Their structure consisted of an InGaN/GaN multiple quantum well (MQW) gain region, GaN light-guiding layers, and AlGaIn cladding layers (see the *Structures* section in Chapter II). Edge emitting facets for the LD were produced by reactive ion etching (RIE). A lasing peak occurred at 417 nm for pulsed currents larger than 1.7 A, corresponding to a threshold current density of 4 kA/cm². The pulse width and period were 2 μs and 2 ms, respectively. These LDs had short operation

⁶ Nichia has also recently commercialized a UV LED utilizing a GaN active region. Model Nos. NSHU-550E and NSHU-590E exhibit an output power of 7 mW at 370-375 nm for the recommended 10 mA driving current, and 1 mW at the maximum recommended current of 15 mA. These units are being made available only to end users and OEMs at the moment, due to the danger UV light poses for human vision. They are being produced in limited quantity and are currently very expensive (\$30 each).

lifetimes - they failed after only a few milliseconds of exposure to a constant driving current.[‡]

The next major breakthrough in III-Nitride research was the continuous wave (cw) operation of InGaN active region LDs by Nichia, which was accomplished by adjusting the growth technique and conditions, ohmic contact properties, and doping profile. These lasers had a lifetime of around one second at RT, but this increased to 30 minutes when the samples were cooled to 233 K. After much modification to the growth technique, most notably epitaxial lateral overgrowth (ELOG, *a.k.a.* ELO or lateral epitaxial overgrowth – LEO)¹⁷⁻¹⁸, a lifetime of more than 10,000 hours was finally achieved. The ELOG technique consists of growing a mask (SiO_2 ,^{18,19} Si_3N_4 ,²⁰ or SiN_x ²¹) by plasma-enhanced chemical vapor deposition (PECVD) over a GaN layer, then performing RIE to etch the mask and expose stripes in the underlying GaN. The resulting structure is then subjected to another round of GaN growth, but during this step the GaN grows only on the exposed stripes because it can't nucleate on the mask regions. After a certain amount of growth – usually a few μm – in the *c*-direction (vertically outward from the substrate surface), lateral growth is enhanced by changing the growth conditions. This causes the horizontal expansion (parallel to the substrate surface) and eventual coalescence of the GaN stripes. This laterally grown material is essentially free of the threading dislocations that normally plague GaN grown in the *c*-direction.

Reaching this 10,000 hour lifetime allowed the commercialization of Nichia's violet LD. Engineering samples were distributed in 1999, and full-scale production is imminent. Research is currently underway to improve the cost and lifetime of these devices, as well as to extend the operating wavelength of III-Nitride-based LDs both further into the visible and deeper into the UV. Since the first demonstration of this Nitride-based violet LD by Nichia, several other companies and university research groups have reported pulsed and/or cw operation of their own blue/violet LDs. This list

[‡] Using pulsed currents for these experiments is helpful for two reasons. First, the lifetime of the device is lengthened because for each second of pulsed operation the current is only present for: $2 \mu\text{s}$ per pulse \times $(2 \times 10^{-3})^{-1}$ pulses = 1 ms. This effectively increases the lifetime of the device by 1000 \times . Second, the device has time to cool down between pulses. This has the effect of further increasing the operating lifetime since the most common failure mechanism of LDs is related to the propagation of crystalline defects (dark lines) at high operating temperatures. However, for an LD to be commercially viable, continuous operation is required with a lifetime greater than approximately 10,000 hours.

includes Cree,^{22,23} the University of California at Santa Barbara,^{24,25} Fujitsu,²⁶ Sony,²⁷ Toshiba,²⁸ Xerox,²⁹ Toyoda Gosei (a business unit of the Japanese car manufacturer Toyota),³⁰ Matsushita,³¹ and SDL.³² However, none of these devices has demonstrated the long lifetime or reliability needed for commercialization. The challenges facing these competitors are not getting any easier, either, since Nichia now holds patents on several proprietary growth processes and has shown the resolve to defend them. They recently filed a patent infringement lawsuit against Toyoda Gosei dealing with the technology of blue LEDs on sapphire substrates. The Tokyo District Court subsequently approved Nichia's claim that Toyoda Gosei infringed on its patent (awarded in February 1998 for a blue LED using GaN compounds). The court ordered Toyoda Gosei to cease manufacturing and marketing the LEDs and to pay ¥100 million (\$900,000) to Nichia. In late 1999, Nichia took out a patent infringement injunction against Sumitomo Electric Industries to prevent it from distributing GaN-based LED products made by Cree.[§]

[§] On September 22, 2000, Cree Inc. filed a suit against Nichia alleging infringement on U. S. patent No. 6,051,849 entitled "Gallium Nitride Semiconductor Structures Including a Lateral Gallium Nitride Layer That Extends From an Underlying Gallium Nitride Layer," which was issued to North Carolina State University in April 2000 and is licensed to Cree under a June 1999 agreement pursuant to which Cree obtained rights to a number of LEO and related techniques. In its complaint, Cree alleges that Nichia is infringing the patent by, among other things, importing, selling, and offering for sale in the U. S. certain GaN-based LEDs covered by one or more claims of the patent. The lawsuit seeks damages and an injunction against infringement. North Carolina State University is a co-plaintiff in the action.

History of ZnO Research

Zinc Oxide (ZnO) has garnered much attention recently due to its potential for use in blue/UV light emitters. ZnO has a much more colorful history than the Nitride family, in the sense that it has been an important industrial material in a variety of applications for many years. In powdered form, ZnO has been used for years in fluorescent light bulbs, as a white pigment, and as a filler for rubber products. It has also recently found a niche in the solar photovoltaic industry as a transparent front electrode for multijunction solar cells.³³ Because it has a lattice mismatch of only 2% with GaN, ZnO can be used as a buffer layer for the growth of III-Nitrides.³⁴

Up to now, ZnO-based light emitting devices have eluded researchers, mainly due to a large intrinsic background *n*-type carrier concentration. Most attempts to achieve *p*-type doping have failed due to the compensation effect.^{35,36} Several preliminary reports have been published on the successful fabrication of *p*-ZnO,³⁷ but the growth mechanisms are not well understood and are thus difficult to control. In addition, the sample resistivity for these films is too high. *Ab initio* electronic band structure calculations by Yamamoto *et al* have studied the effect of N-doping;³⁸ as an O-substituting species, N should act as an acceptor in ZnO. They concluded that codoping with Al, Ga, or In should enhance the incorporation of N acceptors and lower the resistivity. Aoki *et al* recently created a ZnO *p-n* diode by excimer laser doping using thin Zn₃P₂ layer grown on top of a bulk *n*-ZnO crystal.³⁹ They used the excimer laser to decompose the Zn₃P₂ and diffuse the atoms into the underlying ZnO. The resultant ZnO:P is *p*-type, as evidenced by diode-like I-V curves.

This situation should sound very familiar to the reader, since it was exactly the case for GaN in the mid-to-late 1980s. It is likely that this obstacle will suffer a similar fate as it did with GaN, and ZnO devices will eventually begin to reach the optoelectronics market, maybe even stealing some of the sunshine away from the III-

Nitrides in the process. This will likely occur in the same way it did for GaN. First, the quality of the material needs to be increased significantly to lessen the defect density and hence the free electron concentration. Secondly, a 21st century analogue of Amano needs to come along and discover an efficient way of creating *p*-type ZnO material. Then the “Nakamuras” of the ZnO community will take over, tweaking the growth processes and device structures, and will eventually succeed in fabricating a high quality *p-n* junction. Where it goes from there will depend on the cost-efficiency of ZnO-based optoelectronic devices compared to the tried-and-true III-Nitride technologies, and on the availability of applications in which ZnO either has no other competitor or offers a significant operational advantage.

One of the above-mentioned issues that needs to be addressed before ZnO-based devices become plausible is that of contacts. To the author’s knowledge, no reports have been published in the literature yet on creating *p*-type contacts to ZnO, since the *p*-ZnO reported in the literature thus far is too resistive. However, significant progress has been made on *n*-type contacts very recently by Kim *et al.*⁴⁰ They deposited Ti/Au contacts on Al-doped ZnO and measured the current-voltage (I-V) curves and specific contact resistivity (ρ_c). They found that the applied contact scheme led to ohmic behavior (*i.e.* a linear I-V response) and low-resistivity contacts ($\rho_c = 2 \times 10^{-4} \Omega\text{-cm}^2$). These results paint a very optimistic picture of the future for ZnO-based optoelectronic research.

Much of the recent research on ZnO has focused on the large exciton binding energy in this material: 60 meV (almost three times that of GaN). Excitonic gain mechanisms could potentially dominate at room temperature in ZnO-based LDs, leading to low lasing thresholds and hence efficient UV LDs. Stimulated emission/lasing in ZnO has been observed by several groups, including the author’s (see Chapter VI). These reports deal with bulk ZnO,⁴¹ epilayers grown on sapphire by molecular beam epitaxy (MBE),⁴² self-assembled microcrystallites on sapphire by laser MBE,⁴³ and polycrystalline films on amorphous fused silica by laser ablation.⁴⁴

Another interesting application for ZnO crystals lies in the field of telecommunications. Erbium atoms have a characteristic emission peak at 1.54 μm , which is within the wavelength range of minimum loss for silica optical fibers.⁴⁵ It has been demonstrated that doping Er atoms into a wide bandgap host material is an effective

way to enhance the Er-related emission.⁴⁶ In addition, oxygen codoping has been shown to increase the emission efficiency.⁴⁷ For these reasons, ZnO:Er has emerged as an extremely attractive host/dopant material system for the development of novel optoelectronic devices for use in telecommunications. In local networks, planar amplifiers fabricated from this material would be useful because they allow signal amplification over a much shorter distance than the currently used Erbium-doped fiber amplifiers (EDFAs), which are typically several meters long.⁴⁸ In addition, this technology would allow the integration of planar amplifiers, optical couplers, splitters, and wavelength division multiplexers (WDMs) on a single chip.^{49,50} ZnO:Er thin films have been successfully fabricated by pulsed laser deposition, and sharp and intense photoluminescence peaks at 1.5377 μm were observed.⁵¹ As discussed above, more work on the doping and contact properties of ZnO and related materials needs to be done before functional optoelectronic devices become a reality.

Yet another dopant-related application for ZnO lies in the area of field emission displays (FEDs). FEDs are one of the most promising candidates for creating bright flat panel displays with a wide viewing angle. Oxide phosphors have garnered much support over the conventional sulfide phosphors due to their higher stability in a high vacuum environment and a lower emission of contaminating gases.⁵² ZnO:Eu is a known red light emitting material, but progress in creating a usable phosphor with this material has been plagued by a broad green emission from the host lattice. Recently, ZnO:EuCl₃ phosphors have been shown to exhibit red emission while simultaneously quenching the broadband green emission from the ZnO host crystal.⁵³

The amount of research on ZnO is sure to increase rapidly in the next few years, as the growth capabilities and knowledge of the growth mechanisms and the physical properties of ZnO becomes more mature. In addition, as III-Nitride technology becomes more established and basic research spreads to new avenues, ZnO is sure to capture a larger portion of the research community's interest.

Organization of This Thesis

This monograph will describe the contribution of the author to the study of the optoelectronic and material properties of the group-III Nitrides and ZnO. The first chapter of this thesis, which you have just been reading, gives an introduction to the III-Nitrides that details the technological importance of this material system by listing current and future applications of III-Nitride-based optoelectronic devices. It also gives a history of the basic research on GaN that culminated in the commercialization of the violet LD by Nichia. Next, a history of the research performed on ZnO will be presented. An explanation of the different ways used to refer to the color of a photon will then be given, with a detailed definition of the different units involved and their relations to one another. The Kelvin temperature scale will be briefly introduced. Finally, the organization of the rest of this thesis will then be described, followed by a list of useful definitions, a list of acronyms, and a list of constants and symbols.

Chapter II is designed to familiarize the reader with the basic physical properties of the group-III Nitrides and ZnO. In addition, the relevant semiconductor materials, growth techniques, and structures that will be discussed in later chapters will be presented here.

Chapter III will present an inventory of the various experimental techniques used by the author to perform the research presented in this thesis. A detailed explanation of each experiment is given, along with typical results, with emphasis placed on the experiments that will be discussed in later chapters.

Chapter IV gives a detailed description of several research projects completed by the author to study the intrinsic optical properties of GaN epilayers. Intrinsic Excitons in GaN will be presented first, followed by Excitons and Strain in GaN Epilayers, and finally Photoconductivity Spectroscopy of GaN Epilayers.

Chapter V presents the results of research projects designed to study alloys and heterostructures of the III-Nitride material system. In order of presentation, they include: Optical Properties of $\text{In}_x\text{Ga}_{1-x}\text{N}$ Alloys, High-Pressure Studies of the III-Nitrides, Dynamics of Photoexcited Carriers in AlGaN/GaN Double Heterostructures, Excitation Wavelength Dependence of Stimulated Emission/Lasing from AlGaN/GaN Separate Confinement Heterostructures, and Comparison of Emission from Highly Excited (In,Al)GaN Thin Films and Heterostructures.

Chapter VI gives a detailed description of several research projects completed by the author to study the ZnO material system. In order of presentation, they are: Stimulated Emission Properties of ZnO, and Comparison of the Structural and Optical Properties of Bulk and Epitaxial ZnO Crystals.

Chapter VII will summarize the results presented in this thesis and make some predictions for the future of III-Nitride and ZnO research.

Appendix A gives a list of publications and presentations that were generated from the research contained in this thesis.

Appendix B will give an overview of the laser induced epitaxial liftoff technique.

Important Definitions

Before we move into the main body of this thesis, a few definitions are in order. This is intended to provide the novice reader with a definition of some important terminology and provide the expert reader with the author's connotation of it. Indeed, several of the terms presented here are often misused in the literature and research community. Hopefully this section will serve to prevent confusion in later chapters.

1. 6H-SiC – One of several different polytypes of crystalline silicon carbide, it is commonly used as a substrate for III-Nitride growth and is the only polytype that will be discussed here
2. Bulk material – pure semiconductor material that is grown without using a substrate, but typically requires a small high quality “seed” crystal to begin the growth process; often used as a substrate itself for further epitaxial growth (this term is commonly and somewhat confusingly used to differentiate a relatively thick epilayer of pure material from a complex structure or an alloy – this manuscript will not use this term in that fashion)
3. Epilayer or Epifilm – a layer of semiconductor material ranging in size from Å to μm grown by an epitaxial technique on a substrate, either homoepitaxially or heteroepitaxially
4. Heteroepitaxy – the growth of a certain semiconductor material on a substrate of different material (*e.g.* ZnO on GaN)
5. Homoepitaxy – the growth of a certain semiconductor material on a substrate of identical material (*e.g.* GaN on bulk GaN)
6. MOCVD – MetalOrganic Chemical Vapor Deposition, also commonly referred to as OrganoMetallic Vapor Phase Epitaxy (OMVPE) and MetalOrganic Vapor Phase Epitaxy (MOVPE)

List of Acronyms

2DEG – two-dimensional electron gas
CCD – charge coupled device
cw – continuous wave
DBR – distributed Bragg reflector
DAC – diamond anvil cell
DVD – digital video disk or digital versatile disk
EDFA – erbium-doped fiber amplifier
ELO or ELOG – epitaxial lateral overgrowth
FED – field emission display (device)
FWHM – full width at half maximum
HBT – heterojunction bipolar transistor
HEMT – high electron mobility transistor
HFET – heterojunction field effect transistor
HVPE – hydride vapor phase epitaxy
IR – infrared
I-V – current-voltage
LED – light emitting diode
LEEBI – low-energy electron beam irradiation
LEO –lateral epitaxial overgrowth, same as ELO and ELOG
LD – laser diode
LMBE – laser molecular beam epitaxy
LO – longitudinal optical (in reference to a phonon)
LT – low temperature
MBE – molecular beam epitaxy
MMIC – monolithic microwave integrated circuit

MOCVD – metalorganic chemical vapor deposition
MQW – multiple quantum well
OMA – optical multichannel analyzer
PD – photodetector, photodiode
PECVD – plasma-enhanced chemical vapor deposition
PL – photoluminescence
PLD – pulsed laser deposition
PLE – photoluminescence excitation
PMT – photomultiplier tube
PR – photoreflectance
RIE – reactive ion etching
rf – radio frequency
RT – room temperature
TEM – transmission electron microscopy
QW – quantum well
SCAM – ScAlMgO_4
SCH – separate confinement heterostructure
SE – stimulated emission
SHG – second harmonic generation
SVPT – seeded vapor phase transport
TIPL – time-integrated photoluminescence
TRPL – time-resolved photoluminescence
UV – ultraviolet
WDM – wavelength division multiplexing
XRD – X-ray diffraction

List of Constants and Symbols

<u>Symbol</u>	<u>Description</u>	<u>Units</u>	<u>Value</u>
c	Speed of light in a vacuum	--	2.998×10^8 m/s
C_{ij}	Elastic stiffness constants	GPa	--
D	Diffusion coefficient	cm^2/s	--
D_i	Deformation potentials	eV	--
E	Energy	eV	--
E_g	Bandgap energy	eV	--
E_C	Bottom of the conduction band	eV	--
E_V	Top of the valence band	eV	--
h	Planck's constant	--	4.136×10^{-15} eV-s
\hbar	Planck's constant/ 2π	--	0.6582×10^{-15} eV-s
I_{th}	SE/lasing threshold	kW/cm^2	--
k_B	Boltzmann's constant	--	8.617×10^{-5} eV/K
$k_B T$	Thermal energy	meV	25.8 meV at RT
L_b	Barrier width	nm	--
L_w	Well width	nm	--
M	Reduced effective exciton mass	in terms of m_o	--
m_e^*	Electron effective mass	in terms of m_o	--
m_h^*	Hole effective mass	in terms of m_o	--
m_o	Electron rest mass	--	9.109×10^{-31} kg

N_D	Density of donor sites	cm^{-3}	
N_A	Density of acceptor sites	cm^{-3}	
n	Refractive index	--	--
$[n]$	Density of free electrons	cm^{-3}	--
$[p]$	Density of free holes	cm^{-3}	--
P	Pressure	GPa	--
T	Temperature (absolute)	$^{\circ}\text{C}$ (K)	--
u	Poisson's ratio	--	--
V_N	Nitrogen vacancy	--	--
v_d	Carrier drift velocity	cm/s	--
α	Absorption coefficient	cm^{-1}	--
Δ_{CR}	Crystal field splitting	eV	--
Δ_{LT}	Longitudinal-transverse polariton splitting	eV	--
Δ_{SO}	Spin-orbit splitting	eV	--
ϵ	Dielectric constant	--	--
ϵ_{\parallel}	Strain in the a -plane of wurtzite	--	--
ϵ_{\perp}	Strain in the c -plane of wurtzite	--	--
λ	Wavelength	nm	--
ρ_c	Specific contact resistivity	$\Omega\text{-cm}^2$	--
τ_{eff}	Effective carrier lifetime	ns, ps	--
τ_D	Effective carrier capture time	ns, ps	--
τ_{NR}	Nonradiative carrier lifetime	ns, ps	--
τ_R	Radiative carrier lifetime	ns, ps	--

CHAPTER II

GENERAL PROPERTIES OF THE III-NITRIDES AND ZnO, GROWTH METHODS, AND IMPORTANT DEVICE STRUCTURES

Wide bandgap semiconductors possess many interesting and technologically important physical properties that can be explored by a wide range of experiments. This chapter will provide a general introduction to the crystal properties and band structure of semiconductors relevant to this thesis focusing on the key characteristics of the III-Nitrides and ZnO. The experimental apparatus corresponding to much of the research detailed in later chapters will be presented with a comprehensive explanation of the physical processes involved along with typical data from relevant samples.

Crystal Properties

GaN, InN, AlN, and ZnO are tetrahedrally coordinated semiconductors which are known to form in three different crystal structures: wurtzite (hexagonal), zincblende (cubic), and rocksalt. The most thermodynamically stable structure for all four materials is wurtzite, and is the only one that will be considered here. The wurtzite crystal structure can be thought of as two interpenetrating hexagonal close-packed sublattices, one of each atomic species, offset from each other in the c -direction by approximately $5/8$ of the cell height (c -lattice constant). A graphical depiction of the wurtzite structure is shown in Figure 2. The physical constants presented in this section are summed up in Table II.

The a lattice constants for GaN, InN, AlN, and ZnO are 3.189, 3.548, 3.112, and 3.252 Å, respectively. This information is depicted in Figure 3, which plots the lattice constant versus bandgap energy (see next section) for several important wide bandgap semiconductors. The lattice parameters become critically important when considering substrates for epitaxial growth. A mismatch in lattice constants between substrate and epilayer can cause dislocations, which severely detract from the quality of the epitaxially grown material. Besides the lattice parameter, there are many other important aspects to be considered when choosing a substrate for the growth of the III-Nitrides and ZnO, such as bandgap, electrical conductivity, and cleavability.

As mentioned before, the early GaN blue LEDs fabricated by Pankove were not successfully commercialized because (1) the quality of the layers (and hence the intensity and efficiency of light emission) was low, due mainly to the lattice mismatch between substrate and epilayer, and (2) p -doping in this material had yet to be achieved. The first problem has no perfect solution. There is simply no readily available host material with a lattice constant identical to that of GaN, a condition that has historically been required for the growth of high quality semiconductor epilayers. The most commonly used substrates for III-Nitride growth are (0001) sapphire (also referred to as c -plane sapphire) and 6H-silicon carbide (hereafter referred to as SiC, see *Important Definitions* in the previous chapter). However, each of these substrates has several important shortcomings. Both have a significantly large lattice mismatch with GaN: the former has a mismatch of 14.8% while the latter has a mismatch of 3.3% (see Table II). From Figure 3, it can be seen that the lattice mismatch between sapphire and GaN is much larger than 14.8%. This apparent contradiction has a simple explanation. When GaN grows on sapphire, the crystal lattice is rotated by 30° in the growth plane, which accounts for a factor of two reduction in lattice mismatch. Because of this rotation, however, the cleave planes of sapphire do not line up with those of the epitaxial GaN film, making the cleaving of laser cavities impossible. In addition, the high resistivity of sapphire prohibits any backside electrical contact to devices grown on this substrate. SiC, on the other hand, is an electrically conductive material that allows backside contacts. SiC also exhibits a much larger potential for heat dissipation in optoelectronic devices – the thermal conductivity of SiC at RT is larger than ANY metal! However, the bandgap energy of SiC is less than

that of GaN, absorbing any light emitted towards the substrate by the epilayer (thereby decreasing the overall emitted intensity of LEDs) and interfering with transmission measurements which are important for optically characterizing samples (see Chapter III). In addition to the difference in lattice constants, both of these substrate materials have a significantly different thermal expansion coefficient than GaN, which can lead to a cracking of the epilayers when the samples are cooled down from the high temperatures (~ 1050 °C) required for growth (for sapphire, $\Delta a/a = 7.5 \times 10^{-6} \text{ K}^{-1}$ and $\Delta c/c = 8.5 \times 10^{-6} \text{ K}^{-1}$; for SiC, $\Delta a/a = 4.2 \times 10^{-6} \text{ K}^{-1}$ and $\Delta c/c = 4.68 \times 10^{-6} \text{ K}^{-1}$; for the III-Nitrides and ZnO, see Table II).

In the case of substrates for the epitaxial growth of ZnO, a problem similar to that of GaN is found. ZnO and GaN have very similar lattice constants, meaning that the use of sapphire and SiC substrates will not allow the growth of lattice matched ZnO layers. This leads to an unusually high density of threading dislocations and defects in the resultant material, which can manifest itself as an increased background free electron concentration and a difficulty to produce *n*-type material. However, recent work by Ohtomo *et al* has shown that the use of a new substrate material known as ScAlMgO₄ (SCAM), which has a lattice mismatch of only 0.09% with ZnO, gives rise to very high quality ZnO epilayers. At RT, these layers had an electron mobility comparable to that of ZnO grown on sapphire, but exhibited a significantly lower *n*-type carrier concentration. The samples also possessed an enhanced crystalline quality as determined by X-ray diffraction measurements.

	GaN	AlN	InN	ZnO
Bandgap E_g (eV at 300 K)	3.39	6.2		3.35
(eV)	3.503 (1.6 K)	6.28 (5 K)	1.9	3.42 (0 K)
Temperature coefficient dE_g/dT (eV/K)	-6.0×10^{-4}		-1.8×10^{-4}	
Pressure coefficient dE_g/dP (eV/kbar)	4.2×10^{-3}			
Lattice constants a (Å)	3.186	3.1114	3.5446	3.252
c (Å)	5.178	4.9792	5.7034	5.213
Thermal expansion $\Delta a/a$ (K $^{-1}$)	5.59×10^{-6}	4.15×10^{-6}	5.7×10^{-6}	8.25×10^{-6}
$\Delta c/c$ (K $^{-1}$)	3.17×10^{-6}	5.27×10^{-6}	3.7×10^{-6}	4.75×10^{-6}
Thermal conductivity κ (W/cm K)	1.35	2		0.6
Refractive index n (at 1 eV)	2.33		2.56	1.92
	2.67 (3.4 eV)	2.15 (3 eV)		
Dielectric constants ϵ_0	10.4	9.14	15.3	8.75
ϵ_∞	5.5	4.84	9.3	3.75
Melting temperature (K)	2791	3487	2146	2248
Lattice mismatch with:				
GaN	0%	2.4%	10.6%	2%
Sapphire	14.8%	12.5%	25.4%	18%
SiC	3.3%	1.0%	14.0%	5.5%

Table II. Fundamental constants of GaN, InN, AlN, and ZnO. Blank cells represent unknown data. Adapted from Refs. [54, 55].

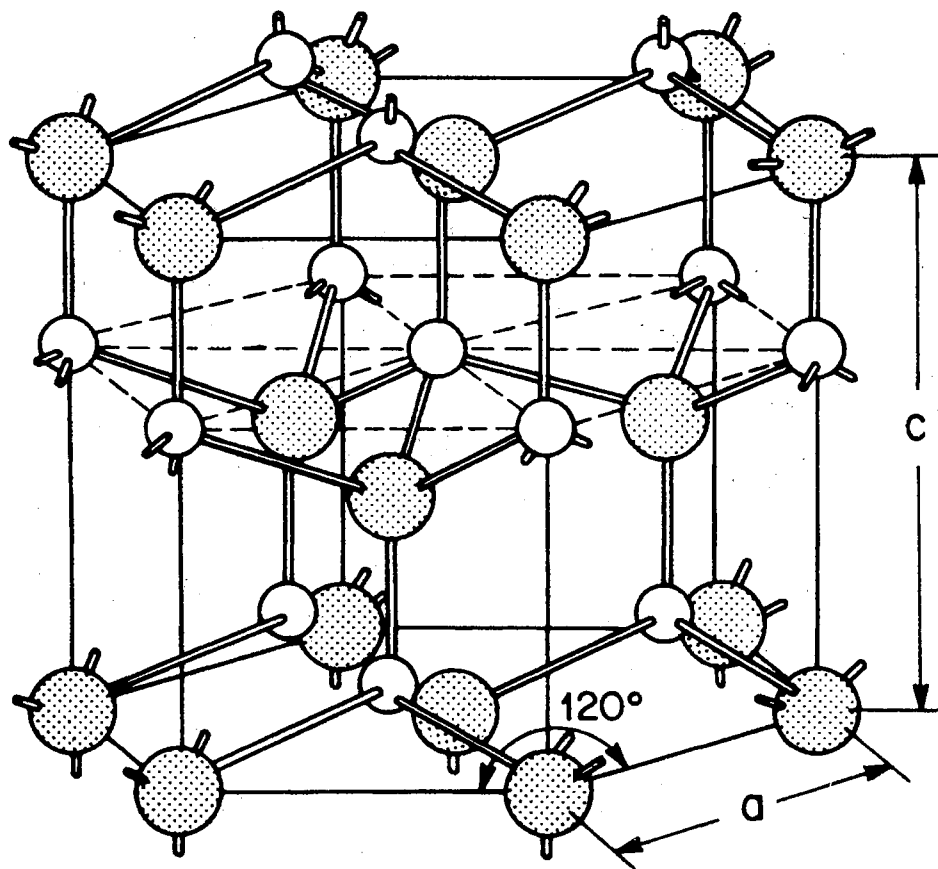


Figure 2. Schematic of the wurtzite crystal structure. Adapted from Ref [56].

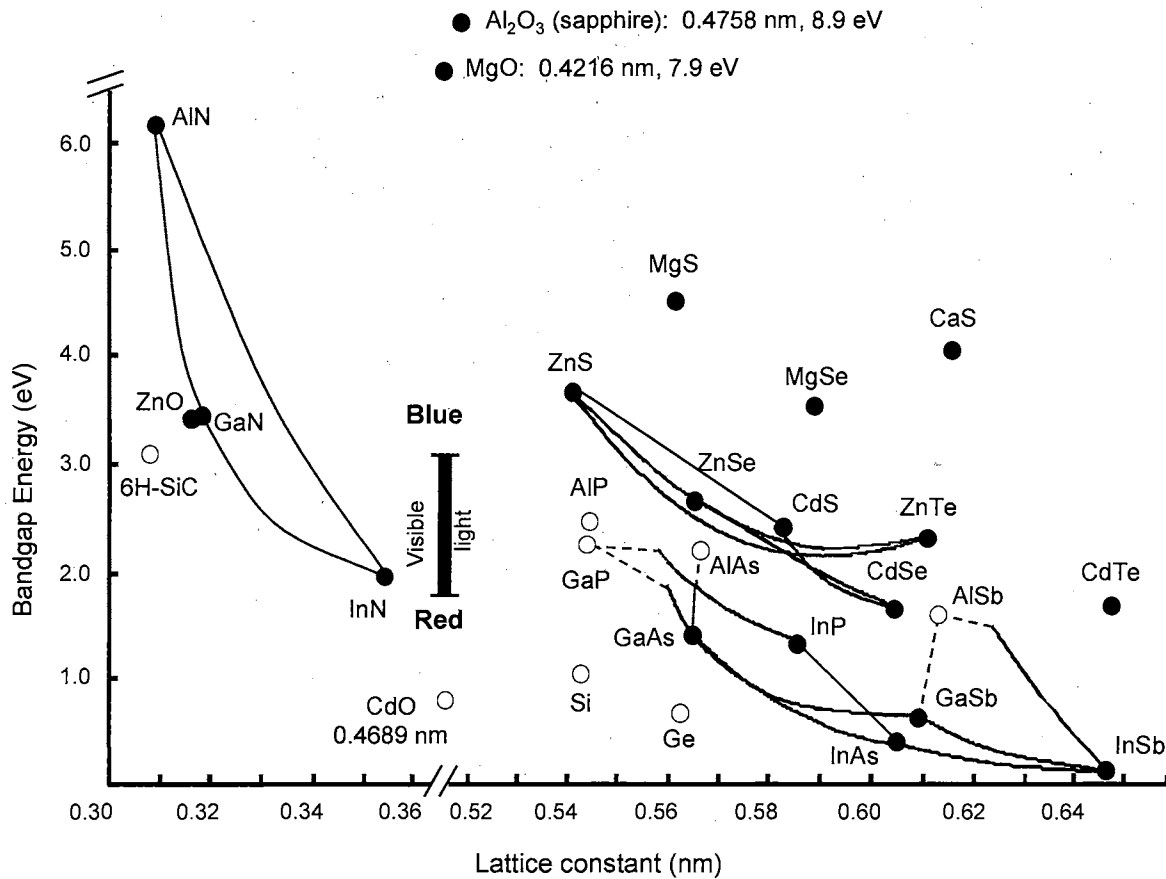


Figure 3. Bandgap energy versus lattice constant for several important semiconducting materials. Direct gap materials are denoted with a solid circle, while indirect gaps are denoted with an open circle. Solid lines connect several important alloy systems: solid lines are used for direct gap alloys, and dashed lines for indirect gap alloys. For reference, the bar in the middle of the figure depicts the spectral energy range occupied by visible light.

Band Structure and Alloys

Intrinsic semiconductors (those which are not intentionally doped with impurities) are characterized by a forbidden region in which no energy states exist. This region is bounded on the low energy side by the valence band and on the high energy side by the conduction band. The magnitude of this forbidden region is commonly referred to as the bandgap energy. For a perfect semiconductor at temperatures near absolute zero, the valence band is completely full of electrons that are bound to their respective lattice sites. The conduction band, however, is completely vacant. When an electron is promoted to the conduction band by a contribution of energy (from electrical injection, optical pumping, thermal excitation, *etc.*), it is no longer bound to a lattice site and is free to move about the crystal as it deems fit.

A complete representation and explanation of the band structure of semiconductors is beyond the scope of this thesis, but there is an abundance of reviews of this topic in the literature. For completeness, the band structure of GaN is presented in Figure 4. This figure presents the energies of various valence and conduction bands versus their position in reciprocal space (*a.k.a.* k -space, where k represents momentum). This gives us some very valuable information – all of the allowable energies that holes and electrons may possess. The indices on the abscissa refer to certain points in k -space. Figure 5 presents a graph of the first Brillouin zone (the reciprocal space equivalent of the crystal lattice) for the wurtzite crystal structure showing those points. The research presented in this thesis deals almost exclusively with optical transitions near $k = 0$, known in Group Theory circles as the Γ point. This is illustrated in Figure 5, where the Γ point can be seen in the middle of the hexagon at the point $k_x = k_y = k_z = 0$.

For wurtzite structures, there are several physical circumstances that cause the valence band to split into three separate bands. This situation is illustrated in Figure 6.

First, the valence band splits into two bands due to crystal field splitting. The higher energy band of these two then splits into two separate bands due to spin-orbit splitting. As a final result of these two splittings, the valence band is left splintered into three separate bands, labeled from high to low energy (top to bottom in the figure) as the A, B, and C bands, respectively. These bands each have their own distinct properties, such as exciton binding energy and selection rules for optical interaction. Under the right circumstances, all three bands can be observed by optical measurements (see Chapter III). Unless otherwise specified, whenever the bandgap of a semiconductor is referred to, it is always the lowest of these split bands – the A band in the case of wurtzite materials. Keep in mind that the “lowest” bandgap energy (the difference between the lowest energy conduction band and the highest energy valence band) does not coincide with the “lowest” energy valence band. Because excited carriers always relax down to the lowest energy levels available, the A band is the most physically important of the three bands for light emitting device applications. (For a split valence band, we should say the *holes relax upwards* to the *lowest energy state* available.)

Even if it runs the risk of being a bit remedial, there are several interesting properties of semiconductors that should be pointed out from Figure 4. We can see from the figure that both the highest valence band energy and the lowest conduction band energy occur at the Γ point. This is the defining characteristic of a direct gap semiconductor. This property allows us to promote an electron from the valence band to the conduction band with the absorption of a photon, which has very little momentum. For an indirect gap material, we would have to rely on interaction with a phonon (a quantum of lattice vibration) to conserve the momentum of the transition. Additionally, in a direct gap material an electron can relax from the conduction band to the valence band (emitting a very useful photon in the process) without having to rely on the absorption or emission of a phonon to conserve momentum. This latter property is a necessity for efficient light emitting devices, e.g. LEDs and LDs. Despite this fact, poorly performing SiC blue LEDs had been commercialized for quite some time before Nichia’s III-Nitride breakthrough, due to the lack of alternative blue light emitting devices.⁵⁷

GaN, InN, and AlN have room temperature direct bandgaps (for the A band) of 3.4, 1.9, and 6.2 eV, respectively. Alloying GaN with InN or AlN to create the ternary alloys $\text{In}_x\text{Ga}_{1-x}\text{N}$ and $\text{Al}_x\text{Ga}_{1-x}\text{N}$ (where the subscripts give the alloy content of each component) allows a continuous tuning of the bandgap from 6.2 eV in the deep UV to 1.9 eV in the red. This range of tunability is far superior to any other family of semiconductor alloys for optoelectronic applications in the UV and visible spectral regions (see Figure 3). Some preliminary work has been performed on the AlInN alloy system, but the quality of the resulting samples has thus far been very poor.⁵⁸ The nomenclature of this system is still in a state of confusion; different reports have called the same alloy $\text{Al}_x\text{In}_{1-x}\text{N}$ and $\text{Al}_{1-x}\text{In}_x\text{N}$. As an example of the alloying technique, consider a mixture of 20% InN and 80% GaN. This alloy is called $\text{In}_{0.2}\text{Ga}_{0.8}\text{N}$ and has a bandgap near 3.1 eV at RT, obtained by a simple linear extrapolation of the RT bandgaps of InN and GaN. (In practice, a linear extrapolation does not sufficiently describe the behavior of the bandgap with alloy concentration – see the following paragraph.) In this family of materials, the nitrogen atom always occupies the anion lattice site. Therefore the sum of the cation ratios for any alloy must equal unity (20% + 80% = 100% in the example given above, or more generally, $x + (1 - x) = 1$). Now, on the other hand, say we want to grow a III-Nitride semiconductor with a bandgap of 5 eV. We can't use InGaN, since adding InN to GaN decreases its bandgap. In this case, we must create an alloy of AlN and GaN. A simple calculation using a linear extrapolation tells us that we need an alloy of 57% GaN and 43% AlN, or $\text{Al}_{0.43}\text{Ga}_{0.57}\text{N}$. Alternatively, we could use the AlInN alloy system, where we would need an alloy of 72% AlN and 28% InN, or $\text{Al}_{0.72}\text{In}_{0.28}\text{N}$.

A physical constant called the bowing parameter slightly complicates the calculation of the bandgap energies of semiconductor alloys. This constant arises because of differences in the atomic radii and binding forces in the alloy. This bowing effect can be seen graphically in Figure 3, where the bandgaps of alloy systems are shown by a line connecting the two constituent materials. Bowing is represented by a curved line. In general, the bandgap energy of a semiconductor alloy can be described by the following empirical equation:

$$E_g(x) = f(x) + bx(1-x), \quad (2-1)$$

where x is the alloy content, b is the bowing parameter, and $f(x)$ is simply the linear interpolation of the bandgap in the absence of bowing:

$$f(x) = (1-x)E_g(0) + xE_g(1). \quad (2-2)$$

The properties of the ternary III-Nitride alloys InGaN and AlGaIn have been intensely studied for several years. The most reliable data taken to date gives the following values for the bowing parameter for these alloy systems: for AlGaIn, $b = 0.62 \pm 0.45$ eV,[‡] for InGaIn, $b = 4.1$ eV.[§] One of the few reports published on the AlInN alloy system suggests the following equation to describe its bowing characteristics: $E_g(x) = 1.75 + 2.2x - 5.6x^2 + 9.1x^3$, where x denotes the AlN concentration (they call the alloy $\text{Al}_x\text{In}_{1-x}\text{N}$).⁵⁹ As will be discussed in later chapters, alloying usually causes a spreading out of the band edge in most semiconductors due to local fluctuations in potential. This is commonly referred to as a “band tail,” and can have a very strong effect on the optical and electrical properties of the alloy sample.

In addition to the ternary III-Nitride alloys listed above, there has been a substantial amount of research on the quaternary alloy AlInGaIn.^{60,61} By carefully choosing the alloy concentrations of the constituent materials, not only can the bandgap energy be tuned, but the lattice constant can be incrementally changed as well. Technical growth issues notwithstanding, the AlInGaIn alloy system should allow independent tuning of the bandgap anywhere between 1.9 and 6.2 eV and the a lattice constant anywhere between 3.1114 and 3.5446 Å. While a ternary alloy is represented in Figure 3

[‡] The large variation in values reported here for the bowing parameter in AlGaIn alloys stems from a detailed study by Lee *et al* given in Ref. [62]. In addition to growing and performing experiments on their own alloy samples, they reviewed the results of more than 20 reports on the bowing parameter of AlGaIn alloys. Their findings suggested a dependence of bowing parameter on the growth method employed. Directly nucleated or buffered growth of AlGaIn on sapphire at temperatures greater than 800 °C was found to lead to stronger bowing ($b > 1.3$ eV) while growth initiated using low temperature (LT) buffer layers on sapphire followed by high temperature growth led to weaker bowing ($b < 1.3$ eV).

[§] The value given here is for a relaxed InGaIn film.⁶³ Recent reports indicate that the bowing parameter of InGaIn is compositionally dependent and decreases with increasing In content.⁶⁴ In this referenced report, McCluskey *et al* experimentally determined the bowing parameter of strained $\text{In}_{0.1}\text{Ga}_{0.9}\text{N}$ layers to be 3.8 eV. They further performed first-principles calculations that gave values of $b = 4.8, 3.5,$ and 3.0 eV for In alloy compositions of $x = 0.0625, 0.125,$ and $0.25,$ respectively.

by a line between two materials, a III-Nitride quaternary alloy could occupy any position in the area enclosed by the InGaN, AlGaIn, and AlInN curves. This allows the engineering of lattice-matched heterostructures or novel structures that are subject to an adjustable amount of in-plane stress (*a.k.a.* piezoelectric doping). The use of AlInGaIn quaternary alloys could drastically enhance the properties of heterojunction field effect transistors (HFETs) by reducing lattice mismatch, which would increase 2D electron transport and decrease noise levels.⁶⁵

ZnO has a direct bandgap of 3.35 eV at RT (for the A band). The situation regarding alloys with ZnO is similar to the III-Nitrides case, but is in a much more immature state of research. The first alloys using ZnO-based materials have only recently been grown, and the quality of these samples still needs much improvement. ZnO can be alloyed with MgO ($E_g = 7.9$ eV, $a = 4.211$ Å) to allow continuous tuning to shorter wavelengths.⁶⁶ (MgO has also been used as a buffer layer in the growth of extremely high quality ZnO epilayers on sapphire).⁶⁷ Mg was shown to have a solubility limit of only $\sim 4\%$ mole fraction in ZnO,⁶⁸ but a more recent study has suggested a value of 15%.⁶⁹ The same study also exhibited the existence of metastable supersaturated alloys in this material system at temperatures below 1000 °C. In another recent study, $Mg_xZn_{1-x}O$ alloys with x values ranging from 0 to 0.36 were shown to exhibit excitonic absorption features at room temperature.⁷⁰ Using these alloys to create device structures was the next logical step in the development of this alloy system, and this was successfully demonstrated by Ohtomo *et al.*⁷¹ They grew ZnO/Mg_{0.2}Zn_{0.8}O superlattices on a sapphire substrate using laser molecular beam epitaxy (LMBE) and observed a blueshift in the 4.2 K photoluminescence spectrum, indicating a quantum-size effect (see the *Structures* section below). Recently, the same group observed excitonic stimulated emission at RT in ZnO/MgZnO alloys with Mg compositions of 12% and 26% characterized by very low threshold values down to 11 kW/cm².⁷² ZnO can be alloyed with CdO ($E_g = 2.28$ eV, $a = 4.689$ Å) to obtain alloys with bandgap energies lower than that of pure ZnO. Reports on this material were very scarce at the time of writing of this thesis, and much progress needs to be made before high quality CdZnO alloys become a reality. Recently, Makino *et al* grew a MQW consisting of Mg_{0.12}Zn_{0.88}O barriers and

$\text{Cd}_{0.004}\text{Zn}_{0.996}\text{O}$ wells. They observed a 5 K photoluminescence peak at 3.235 eV, several hundred meV below the bandgap of ZnO.⁷³

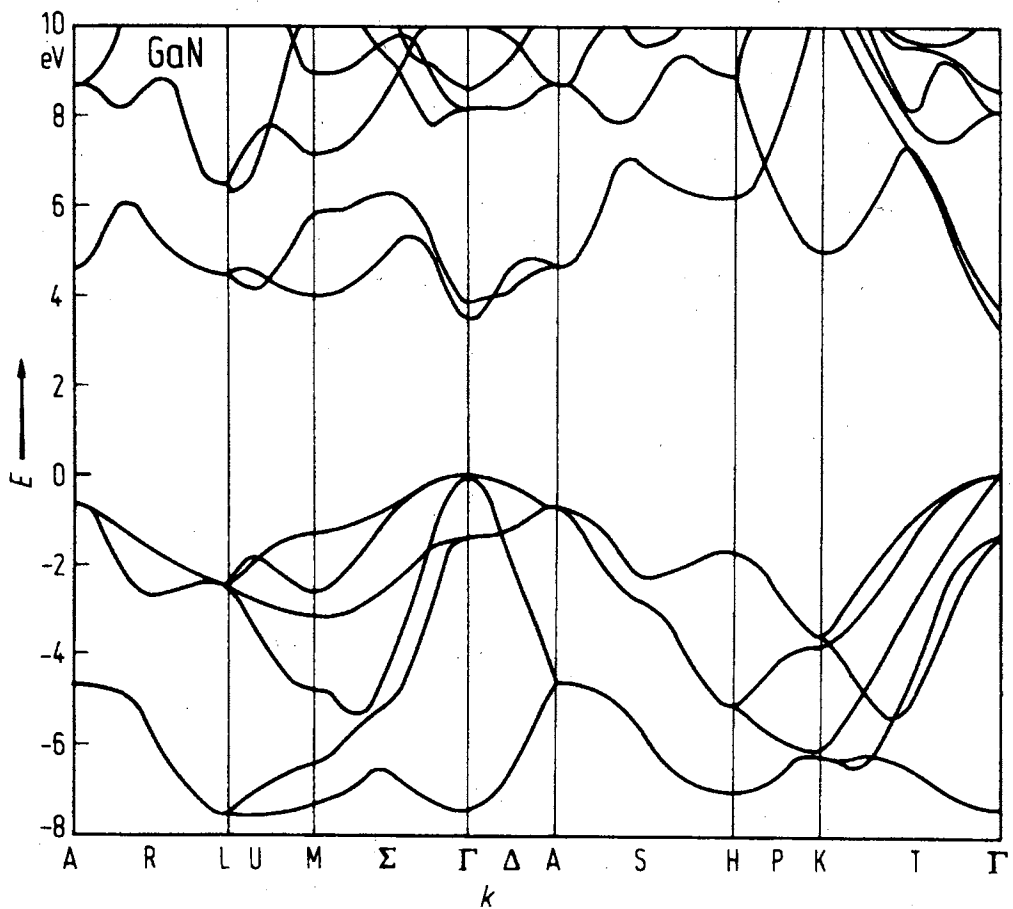


Figure 4. Band structure of wurtzite GaN. Adapted from Ref. [74].

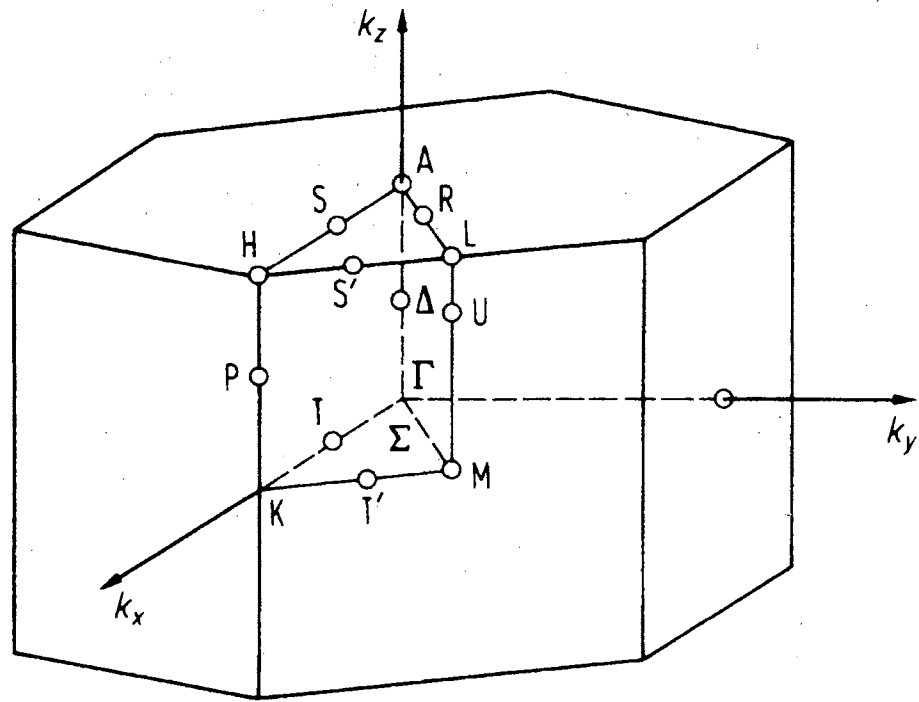


Figure 5. First Brillouin zone of a wurtzite crystal lattice. From Ref. [55].

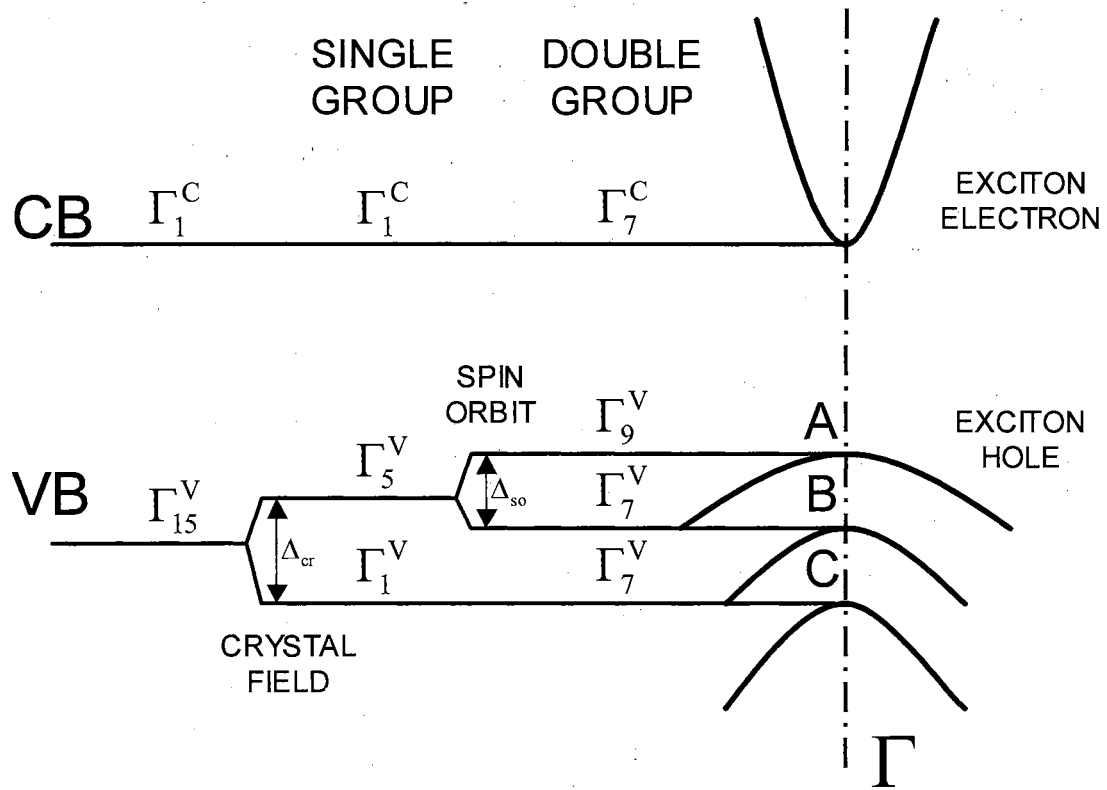


Figure 6. Structure and symmetries of the lowest conduction band and the uppermost valence bands in wurtzite GaN at the Γ point ($k \sim 0$). Adapted from Ref. [75].

Growth Techniques

The techniques used to grow III-Nitride and ZnO samples can be split into two categories: bulk and epitaxial. Bulk growth methods, such as vapor phase transport (VPT), seeded VPT (SVPT) and the hydrothermal method, traditionally use a seed crystal to grow a pure sample of the desired material. This procedure is roughly similar to the elementary experiment of creating sugar crystals from a saturated solution of sugar in water using a single sugar crystal as the seed. Semiconductor samples grown by this method are usually of extremely high crystalline quality, but often suffer from small lateral dimensions. It is common for bulk samples to have thicknesses of several mm (extremely thick compared to the typical epitaxially grown sample thickness of 1-2 μm), but their lateral dimensions are usually limited to the mm regime as well. A group from Tokushima University in Japan has grown hexagonal bulk GaN crystals about 100 μm in diameter by the sublimation method.⁷⁶ Bulk GaN crystals up to 100 mm^2 have been grown by Unipress (High Pressure Research Center of the Polish Academy of Sciences, Warsaw) and exhibit extremely high crystalline quality, as determined by X-ray diffraction, photoluminescence, and transmission electron microscope (TEM) measurements. Homoepitaxial layers of GaN grown on top of these bulk samples by molecular beam epitaxy (MBE) or metalorganic chemical vapor deposition (MOCVD) are of unmatched quality.^{77,78} High quality bulk ZnO samples have been grown using the hydrothermal technique by several groups, including the Air Force Research Laboratory⁷⁹ and Bell Labs.⁸⁰ Recently, Eagle-Picher Laboratories (Miami, Oklahoma) developed a VPT technique to grow bulk ZnO crystals with a 2" diameter. This should pave the way for a large amount of research on the growth of high quality homoepitaxial ZnO and also heteroepitaxial III-Nitride materials⁸¹ due to the small difference in lattice mismatch between ZnO and the III-Nitrides (see Table II).

There are a variety of different epitaxial growth techniques used to grow III-Nitride and ZnO materials. Recently, the best III-Nitride samples have been grown using MOCVD. This technique involves heating a suitable substrate material to high temperatures and flowing a combination of gases, which contain the constituent atoms of the material being grown, across the substrate. Some of the atoms stick to the substrate and arrange themselves in a well-defined crystallographic lattice. The detailed growth kinetics of semiconductors are beyond the scope of this thesis. For a more in-depth discussion of this topic, see Ref. [82]. There are many different variations of the MOCVD growth technique, including horizontal and vertical reactor designs, the two-flow method, and atmospheric and low-pressure growth. In addition, there are many variables related to growth that can be changed to produce different quality samples, such as growth temperature and source precursors. To make matters even more complex, the conditions for optimum growth usually vary from one material to another. For example, the substrate temperature can change substantially for different materials (1050-1100 °C for GaN and AlGaN, ~ 550 °C for InGaN), and can make the growth of alloys and/or heterostructures challenging. High quality epilayers have also been grown using MBE and hydride vapor phase epitaxy (HVPE). MBE is similar to the MOCVD growth technique, but instead of gases flowing across the substrate, it involves sputtering source materials from heated crucibles in an ultrahigh vacuum environment. Both MOCVD and MBE are capable of producing extremely thin epitaxial layers, allowing the controlled growth of complex device structures (see next section). HVPE is important because it allows the growth of samples that are very thick compared to the typical 1-2 μm samples grown by MOCVD or MBE. Pulsed laser deposition (PLD) is another technique that has been used to produce III-Nitride materials, but the quality is usually low compared to other techniques. For ZnO, on the other hand, the best quality samples have been produced by MBE and LMBE. MOCVD and PLD have produced ZnO samples of decent quality.

Structures

There are many complex structures that can be grown by the aforementioned growth techniques. The crystal grower can directly control the alloy composition, dopants, layer thicknesses, and growth temperatures to grow samples for a wide range of potential applications. Some of the most common structures, especially those which are used in the research presented in later chapters, will be introduced here.

One of the most commonly grown structures is the quantum well (QW). A QW consists of a thin layer of semiconductor material, typically on the order of several nm, sandwiched between so-called barrier layers which have a larger bandgap value. This is shown schematically in Figure 7(a), with the well width denoted by L_w . The most common way to create these wells is by epitaxially growing alloy systems, *e.g.* GaAs/Al_xGa_{1-x}As or In_xGa_{1-x}N/GaN for the well/barrier. As mentioned in the previous section, modern growth techniques allow the precise growth of extremely narrow regions with well-defined interfaces. One QW all by itself is referred to as a single quantum well (SQW). When the barrier regions are also relatively thin and there is more than one well, as seen in Figure 7b, the structure is known as a multiple quantum well (MQW). The barrier width is given by L_b . The difference in well and barrier bandgap energies, $\Delta E_g = \Delta E_g(\text{barrier}) - \Delta E_g(\text{well})$, is known as the band offset, and allows carriers to be confined in the well region, a fact that becomes extremely useful when one wishes, say, to create a two-dimensional electron gas (2DEG), generate a population inversion, or simply create a region in which a large number of carriers will reside. Because of the extremely narrow dimensions in the growth direction of SQWs or MQWs and the wave-particle duality nature of electrons, quantized states form according to the laws of quantum mechanics (similar to the infamous “particle in a box” problem). These states have an energy larger than the bandgap energy of the well material due to the quantum confinement effect (see

the quantum states $n = 1, 2, \dots$ in Figure 7(a)). As can also be seen in Figure 7(a), the total band offset ΔE_g can be split into two parts: the valence band offset (ΔE_v) and the conduction band offset (ΔE_c). The ratio of these two offsets is dependent on the materials used in the structure, and is an extremely important parameter in the design of efficient optoelectronic devices. For the GaAs/AlGaAs system shown in the figure here, $\Delta E_v = 0.15 \Delta E_g$, and $\Delta E_c = 0.85 \Delta E_g$, thus $\Delta E_c/\Delta E_v = 5.7$. As will be seen in later chapters, MQWs are very useful structures and are commonly employed as active regions in LEDs and LDs.

Another common semiconductor structure is the double heterostructure (DH), pictured in Figure 8. A DH consists of an active region in the center (similar to that of a QW, but much thicker), and two surrounding cladding layers. The basic design principle of a DH is to combine the confinement of photons with the confinement of carriers. The carrier confinement effect results from the desire of carriers to seek out the lowest energy level available. Once they drift or diffuse into the active region and get rid of their excess kinetic energy, they cannot escape. They are confined to this narrow volume. This effect can be very advantageous for certain devices, as mentioned above for QWs. Optical confinement arises from the difference in refractive index between the active region and the cladding regions. If the materials are chosen correctly, the difference in refractive index between these two layers will cause total internal reflection for light emitted in certain directions. This light will propagate through the sample with minimal loss until it escapes at the end of the cavity. The confinement of light is crucial for LDs, specifically for the efficient extraction of gain from the laser cavity and for keeping the far-field emission pattern relatively small.

Separate confinement heterostructures (SCHs) play an extremely useful role in device physics. A typical SCH structure is shown in Figure 9. As its name suggests, an SCH provides two separate confinement regions – a narrow one in the center of the structure to confine carriers, and a wider one symmetric about the center to confine the output light from the device. The center region, called the active region, consists of a narrow ($\sim 100 \text{ \AA}$) layer of semiconducting material. Both sides of the active region are bordered by thicker layers of material with a larger bandgap energy called waveguide regions. Symmetrically located around the waveguide regions are thick layers of material

with an even higher bandgap energy called cladding regions. By using a widely spaced layer of material with lower index of refraction around the active region to confine the light output of the device, the junction region can be made extremely thin without refracting the emitted light out of the cavity. Thus SCHs combine the quantum effects of QWs and the optical confinement properties of DHs, both of which can be very advantageous for creating efficient devices.

Several other important semiconductor device structures are given in Figure 10. Figure 10 (a) and (b) show a MQW-SCH (an SCH with a MQW for an active region instead of a SQW) and a graded-index SCH (GRINSCH), respectively. Figure 10 (c) and (d) show two widely used index-guided LD structures: a ridge waveguide and buried-heterostructure LD, respectively.

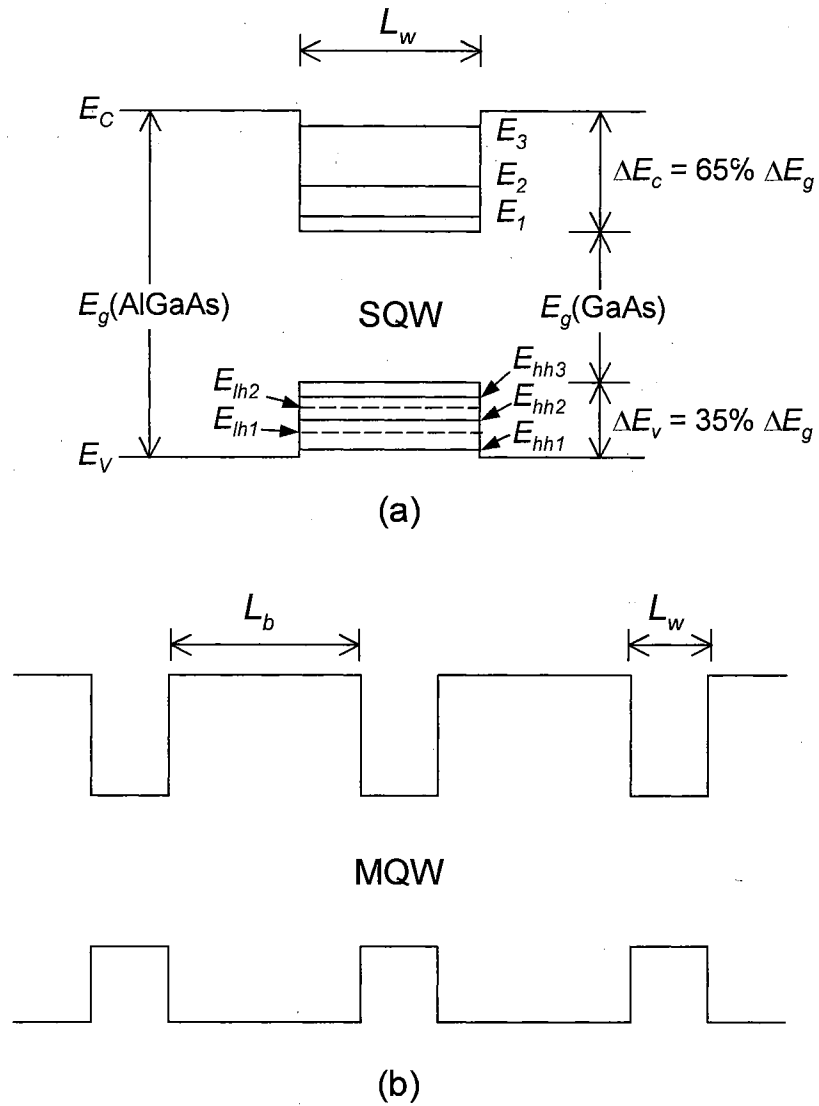


Figure 7. Schematic diagram of (a) single quantum well (SQW) and (b) multiple quantum well (MQW) structures. The quantum confined energy levels in the conduction band are denoted by E_n , where $n = 1, 2, \dots$, and those in the valence band are given as E_{hhn} where $n = 1, 2, \dots$ (for heavy holes) and E_{lhn} where $n = 1, 2, \dots$ (for light holes). Barrier and well width are denoted by L_b and L_w , respectively. The values of conduction band offset (ΔE_c) and valence band offset (ΔE_v) are also given for the GaAs/AlGaAs material system. Adapted from Ref [83].

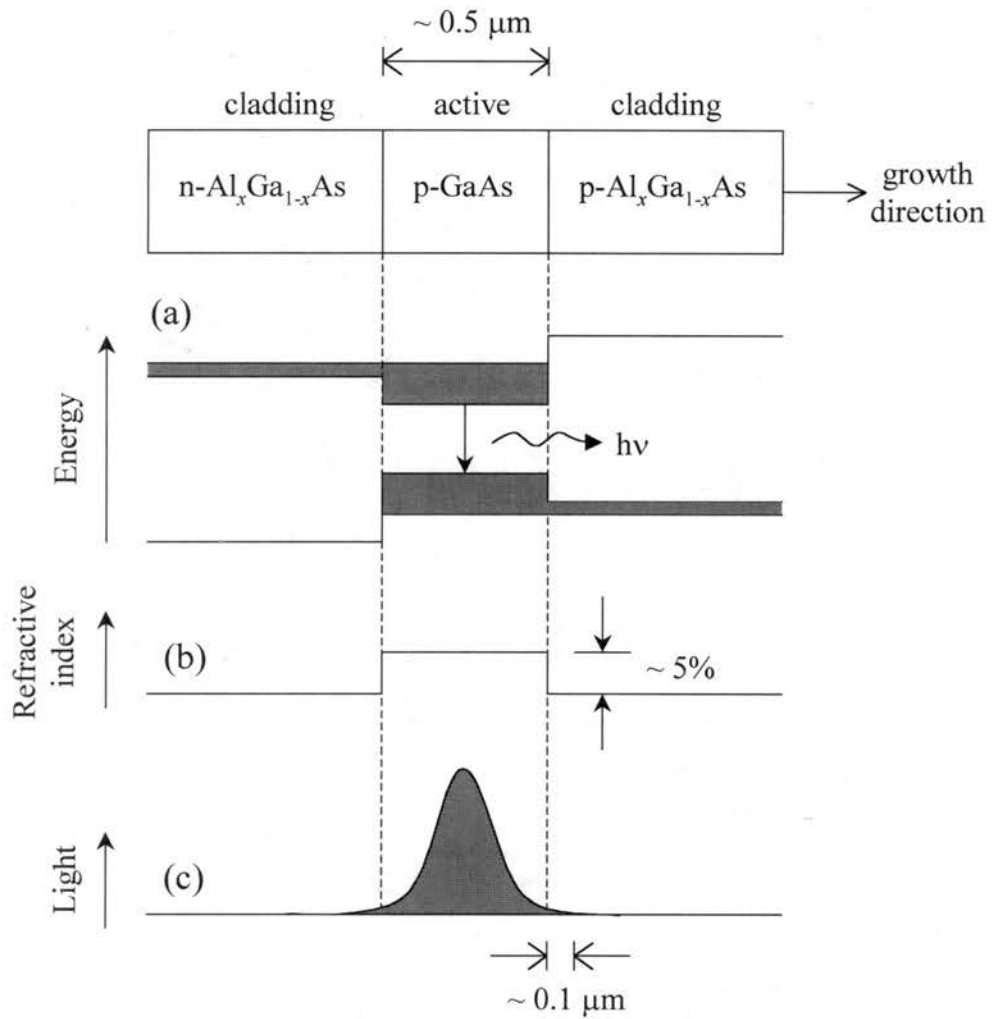


Figure 8. Schematic design of a double heterostructure (DH) fabricated using the GaAs/AlGaAs material system. The dimensions and energy band diagrams of the various layers are given in (a), the change in refractive index is shown in (b), and the confinement of light is given in (c). Adapted from Ref. [84].

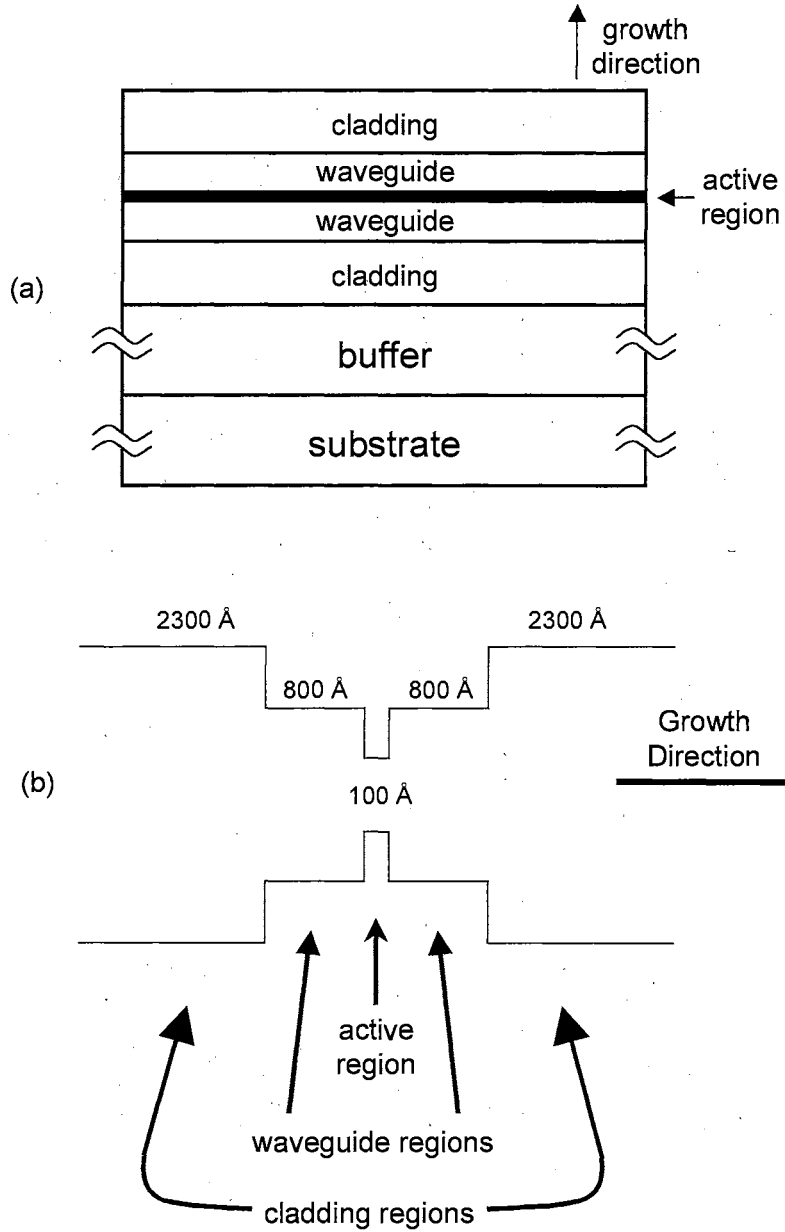


Figure 9. (a) Schematic drawing and (b) energy-band diagram of a typical separate confinement heterostructure (SCH).

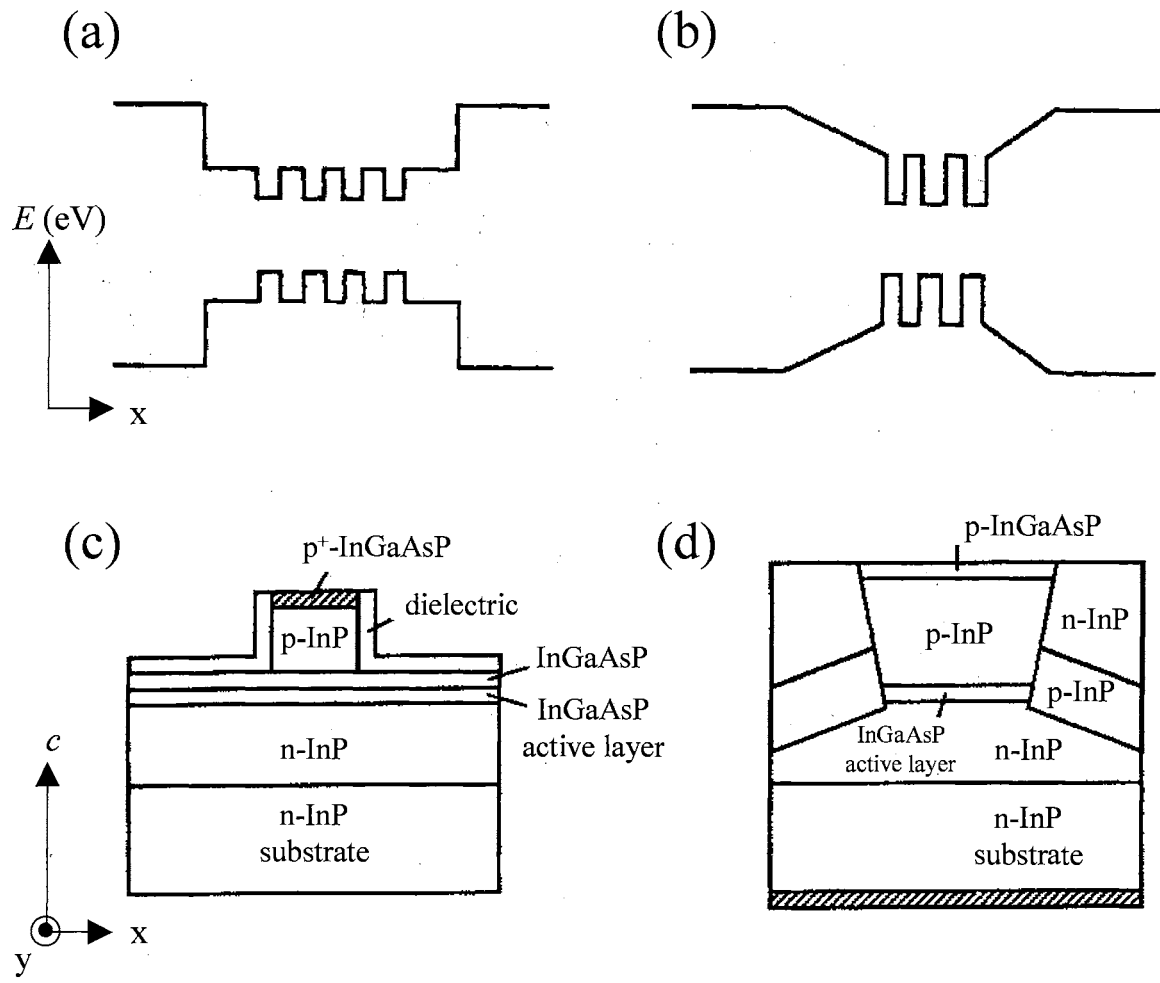


Figure 10. Several important semiconductor device structures: (a) multiple quantum well SCH, (b) graded-index SCH (GRINSCH), (c) ridge waveguide LD, and (d) buried-heterostructure LD. The axes are given on the left side of the figure. For (a) and (b), the graphs represent energy-band diagrams (energy vs. layer thickness). For (c) and (d), the graphs show cross sections of the sample structures in the lateral direction (x) with the growth direction denoted by c . The laser cavities are oriented along the y -axis. Adapted from Ref. [85].

CHAPTER III

EXPERIMENTAL METHODS USED TO CHARACTERIZE WIDE BANDGAP SEMICONDUCTORS

Optical experiments provide researchers with an indispensable tool to characterize semiconductor materials. Studying the interaction of photons with a semiconductor can yield direct insight into the physical processes taking place in the sample. The knowledge gained through these experiments is useful in many ways, particularly in (1) characterizing the optical properties of the material (e.g. refractive index, phonon energies, or exciton binding energy) or (2) assessing the optical quality of the material (e.g. stimulated emission or lasing threshold, luminescence efficiency, or emission wavelength). The latter of these two seems more exciting, since it deals with actual devices, but the former is an extremely useful process. To be able to grow high quality devices, the research community must know the general optical constants of the material they are growing. In fact, a detailed knowledge of these constants is necessary to grow even the most rudimentary device. Basic experiments that study the optical properties of semiconductors form a basis of knowledge that allows us to improve the quality of semiconducting devices and even to grow interesting new materials.

This chapter will introduce several of the most important optical characterization techniques in detail, with an emphasis on the experiments that were used in the research performed by the author that is presented in later chapters. The experiments described here are, in order of presentation, photoluminescence (including temperature, power, and pressure dependence as well as time-resolved), photoluminescence excitation, absorption, reflectance and photoreflectance, and stimulated emission/lasing.

Photoluminescence

Photoluminescence (PL) is perhaps the easiest and most useful of all the optical experiments used to characterize semiconductors. Figure 11 (a) shows the basic PL experimental setup. In PL, a beam of light (usually from a laser) is made incident on a piece of the semiconductor being studied. PL is commonly performed in the surface-emitting geometry, pictured in Figure 12 (a). For studying materials with a bandgap energy in the UV, a HeCd or FReD (frequency-doubled Ar⁺) laser is commonly used, with a cw incident power of several tens of mW. This laser light, which has a photon energy greater than the bandgap of the material being studied, excites electrons in the sample from the valence band to the conduction band. The vacant site left by the excited electron is called a hole, and effectively has a positive charge. When an electron relaxes back down to the valence band (*i.e.* an electron recombines with a hole), a photon is emitted. These photons are collected and focused into a spectrometer, in which a diffraction grating disperses the light emitted from the sample into its constituent wavelengths and focuses a specific range of wavelengths on an output slit leading to a detector. Detection can be accomplished by two techniques, which involve different pieces of equipment. The first technique makes use of a photomultiplier tube (PMT). This device converts incident photons into electrons, amplifies the electrons, then measures the current flowing through a resistor due to these electrons. PMTs are extremely sensitive detectors and have a very good signal-to-noise ratio. Because the photons are converted to electrons, however, a PMT doesn't have the ability to discriminate between photons of different wavelength. Thus, the output slits of the spectrometer are made as narrow as possible and the grating must be scanned (a process which can be quite time-consuming and has kept many a graduate student up many a night). The second technique uses a charge coupled device (CCD), which consists of a two-dimensional array of photodetectors. Because of the array nature of the CCD, by

fully opening the output slits of the spectrometer we can concentrate different wavelengths of light on different pixel areas on the detector. This allows the CCD to take spectrally resolved data in just one step; the grating does not need to be scanned. Although the data acquisition rate is must faster for CCDs, the signal-to-noise ratio and sensitivity are inferior to PMTs.

The information obtained from PL results gives the researcher important insight into the radiative recombination processes in the semiconductor. The wavelength or energy position of the emitted light is usually the most important information gained through PL. This can tell us many important things about the sample, such as the value of strain in epitaxial layers (see Chapter V), the crystallinity of the sample (*e.g.*, wurtzite GaN has a different bandgap energy than zincblende GaN), the composition of alloy materials, and can indicate the presence of quantized levels in SCHs or QWs. The intensity of the emission gives an idea as to the luminescence efficiency, which is important in designing bright light emitting devices. The width of the emission line, measured by the full width at half maximum (FWHM), gives information about the optical quality and homogeneity of the samples.

Much additional information can be gained from PL measurements by changing a specific experimental parameter. This can be done on the sample level, for example measuring the PL position for a series of samples with different alloy concentrations to find the bowing parameter, or measuring the PL intensity for a series of samples grown at different temperatures to optimize the growth conditions. It can also be done on the experimental setup level, for example looking at how the PL intensity or emission energy changes with increasing temperature. Several important experimental PL techniques will now be described.

Temperature Dependent PL

Several different effects can be studied by changing the temperature of the sample for PL measurements. First, we can look at how it affects the PL intensity. This can give us information about the interplay between radiative and nonradiative transitions in the material. Nonradiative transitions become more important as the sample temperature is

increased, thus the PL intensity should decrease. The magnitude of this decrease (which can vary from one order of magnitude up to five) is a measure of the optical quality of semiconductor samples. A variant of this technique allows us to tell the difference between free and bound exciton PL peaks. At low temperature, we may observe several strong and narrow peaks in PL spectra due to excitonic transitions. Sometimes, though, there are multiple peaks and it can be difficult to determine their origin. Because a bound exciton is simply a free exciton bound to an impurity in the lattice, its PL transition energy is slightly lower than that of a free exciton. The energy required to free the bound exciton from its impurity captor is easily supplied via thermal phonons, which have an energy of $k_B T$. Thus, as the sample temperature is increased and more thermal phonons are available with higher energies, the bound excitons will be knocked loose, *i.e.* thermally ionized, into a free exciton or the constituent free carriers. This phenomenon, shown in Figure 13, manifests itself in the relative increase of the free exciton PL peak intensity with increasing temperature compared to the bound exciton intensity.

Secondly, we can study how the PL transition energy changes with temperature. The thermal expansion of the crystal lattice with increasing temperature causes a downward shift of the bandgap. The temperature dependence of the bandgap energy of semiconductors can be well described by the Varshni empirical equation:⁸⁶

$$E_o(T) = E_o(0) - \frac{\alpha T^2}{\beta + T}, \quad (3-1)$$

where $E_o(0)$ is the transition energy at 0 K and α and β are referred to as the Varshni thermal coefficients. As an example, the temperature dependence of PL from an $\text{In}_{0.14}\text{Ga}_{0.86}\text{N}$ epilayer is shown in the main graph in Figure 35. In this sample, $E_o(0) = 3.1438$ eV and the Varshni coefficients are $\alpha = 1 \times 10^{-3}$ eV/K and $\beta = 1196$ K. Knowledge of these parameters can aid in the development of light emitting devices that operate at temperatures significantly above or below RT.

Power Dependent PL

By changing the power (intensity) of the incident pump beam in PL experiments, a couple of different processes can be observed. First, we can use this technique to help identify the origin of various PL emission lines. At low pump intensity, we sometimes see several different closely-spaced peaks from a single sample, making a clear determination of their origin difficult. Often, impurities and defects in the semiconductor will act as donors, acceptors, and may form other types of states within the forbidden gap. These extrinsic states may be of a luminescent nature, giving rise to some of the above-mentioned peaks in the PL spectrum. If we increase the pump intensity, these extrinsic levels will eventually begin to saturate out and have less of an effect on the spectrum because of the significantly smaller density of these states compared to the intrinsic states of the crystal. Second, this technique can allow us to assess the influence of piezoelectric (PZ) fields in the material. PZ fields form because of strain in semiconductor epilayers. These fields cause the bands to bend, which allows phonon-assisted transitions at energies slightly below the bandgap energy. However, excitons and impurity states are situated in this same region just below the bandgap energy. (A redshift in the PL energy with respect to the actual bandgap as discussed here is called a Stokes shift, whereas a blueshift is called an anti-Stokes shift). This has caused much debate in the III-Nitride research community about the origin of the PL emission in InGaN/GaN MQWs, which occurs just below the bandgap energy. Different groups have claimed that the observed Stokes shift in this material system is due to PZ-reduced band-to-band transitions and the recombination of excitons localized at indium fluctuations. In the case of a PZ field, if we increase the pump intensity, we should see a gradual blueshift of the PL emission. This is due to the screening of the PZ field: the presence of a large number of free carriers created by the pump would neutralize the PZ field.

Pressure Dependent PL

PL can also be measured as a function of pressure by making use of a piece of equipment called a diamond anvil cell (DAC). A DAC consists of two high quality polished diamonds with a stainless steel gasket between them. A small hole is drilled through the gasket, in which the sample is placed. In order to accommodate the limited dimensions of the volume available inside the DAC, small chips of the samples with dimensions of approximately $200 \times 200 \times 30 \mu\text{m}^3$ are prepared by mechanical polishing and cutting. The DAC is filled with a pressure medium consisting of a 4:1 mixture of methanol/ethanol, and then pressure is applied with a hydraulic press. Unfortunately, there is no direct way to determine how much pressure has been transmitted to the sample. The pressure must be deduced by measuring the pressure induced luminescence shift of the ruby R1 line from a tiny piece of ruby mounted alongside the sample. For low temperature measurements, the cells may be mounted onto the cold finger of a closed cycle helium refrigerator and cooled down to the desired temperatures. The shift of the luminescence due to pressure, $E(P)$, can be well described by the following linear function:

$$E(P) = E(0) + \alpha P, \quad (3-2)$$

where $E(0)$ is the peak position in eV at atmospheric pressure, α is the pressure coefficient, and P is the pressure in kbar.

PL as a function of applied hydrostatic pressure is an excellent probe for distinguishing between deep and shallow defect states. As will be discussed in more detail later, PL transitions involving shallow hydrogenic impurities shift the same amount as the bandedge under pressure. Deep impurities, however, are not tied to any band and thus exhibit a much smaller energy shift under pressure. This technique has also been used to observe how different bands in semiconductors shift with pressure. For example, Shan *et al* observed a crossover of the Γ and X bands in GaAs/GaAs_{0.68}P_{0.32} strained MQWs by studying the position of the main PL peak with increasing pressure.⁸⁷

Time-Resolved PL

Time-resolved PL (TRPL) is an extremely important tool in semiconductor research that allows us to study the temporal profile of PL spectra. Several major changes must be made to the simple PL setup described in the previous sections to allow for the acquisition of temporally resolved spectra. A typical TRPL setup is shown in Figure 14. It is absolutely necessary that a pulsed laser be used. The pulse duration and repetition rate of this laser can vary, but keep in mind that the minimum temporal resolution of the TRPL system is determined by the following three factors: (1) the laser pulse duration, (2) the reaction time of the detector, and (3) various dispersive elements in the optical path such as spectrometers and lenses. For the first factor, it is necessary to make sure the pulse duration of the laser is considerably shorter than the luminescence lifetime being measured, *i.e.* a picosecond PL signal can't be measured using a nanosecond laser. To satisfy the second factor, the appropriate detector must be used. Several choices exist, including photodiodes (~ 1 ns typical resolution, sampling units available down to several hundred ps), photon counting PMTs (~ 50 ps), and streak cameras (~ 2 ps). The third factor only comes into play when working at the extreme low end of the temporal resolution scale. To attain the minimum resolution possible, it is necessary to keep the pump and collection beam paths as clear as possible. This means using thin lenses and cryostat windows, and even using bandpass filters instead of a spectrometer for spectral resolution. All the TRPL data presented in this thesis was taken using a streak camera. This apparatus allows the simultaneous measurement of PL intensity and wavelength versus time. The software lets us choose the region of this 3D data set to analyze: we can look at the temporal profile of a narrow wavelength range (TRPL) or at a snapshot of the whole spectrum at a certain time (TIPL).

TRPL is important because it provides a direct measurement of the decay time of photoexcited carriers. The measured decay time τ_{eff} is related to both the radiative (τ_R) and nonradiative (τ_{NR}) lifetimes in the semiconductor by the following expression:^{126,128}

$$\frac{1}{\tau_{eff}} = \frac{1}{\tau_R} + \frac{1}{\tau_{NR}}. \quad (3-3)$$

Thus we can use TRPL as a tool to interpret the relative magnitudes of the radiative and nonradiative carrier lifetimes. This is a necessary step in the design, growth, and evaluation of light emitting devices, where short radiative lifetimes and long nonradiative lifetimes detrimentally affect performance.

Photoluminescence Excitation

Photoluminescence excitation (PLE) is an experiment that lets us examine which energy levels in a semiconductor contribute to a certain PL emission line. This is done by setting the detection wavelength at the desired PL line and scanning the excitation source (on the high energy side, since we don't expect to see any upconversion). In a sense, we are probing the higher energy bands to see which ones relax radiatively down to the PL transition in question. The experimental setup is shown in Figure 11 (b). PLE can help classify the recombination mechanisms involved in radiative transitions. For instance, by studying the PLE spectra of GaN epilayers, Shan *et al* determined the relaxation scheme of hot bound and free excitons through LO and acoustic phonon emission.⁸⁸

PLE can also be useful in determining the energy levels in multilayer structures involving alloys. Absorption experiments, which are described in the next section, are helpful in determining the bandgap energies of the constituent epilayers in multilayer structures, such as the SCH described above. However, absorption is useless for wide bandgap samples on SiC, since its bandgap energy is less than that of the epilayers. PLE provides an alternative. By setting the PLE detection position at the lowest bandgap-related PL peak (usually the one due to the well or active region) and scanning the excitation source to higher energies, we can usually see changes in the PL intensity due to the absorption of the other layers with higher bandgap energies. The energy positions of these intensity changes in the PLE spectra relate directly to the bandgap energies of these layers. An example of this technique is shown in the bottom graph on Figure 51, for an AlGaIn/GaN SCH sample. The PLE spectrum reveals two changes in intensity, at approximately 320 and 345 nm, which correspond to the bandgaps of the AlGaIn waveguide and cladding layers, respectively. The carriers created in the two AlGaIn

layers by the excitation light drift and diffuse into the lower energy active region, where they recombine and emit the observed PL signal. The PL intensity of the active region is observed to increase at each of these steps due to the increased absorption cross-section.

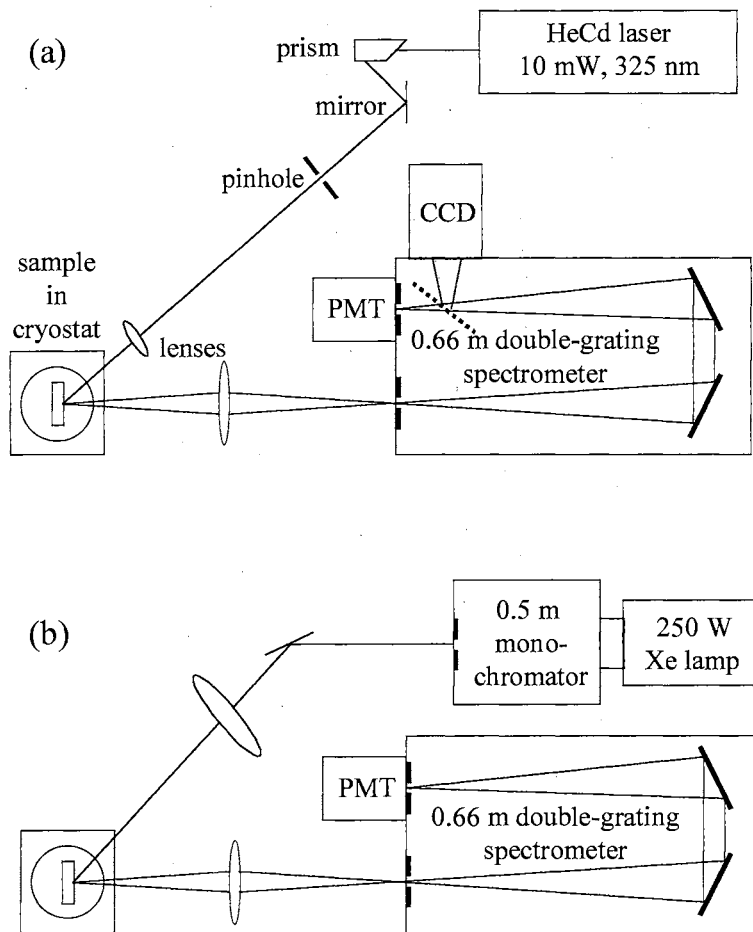


Figure 11. Typical experimental setups for (a) PL and (b) PLE measurements.

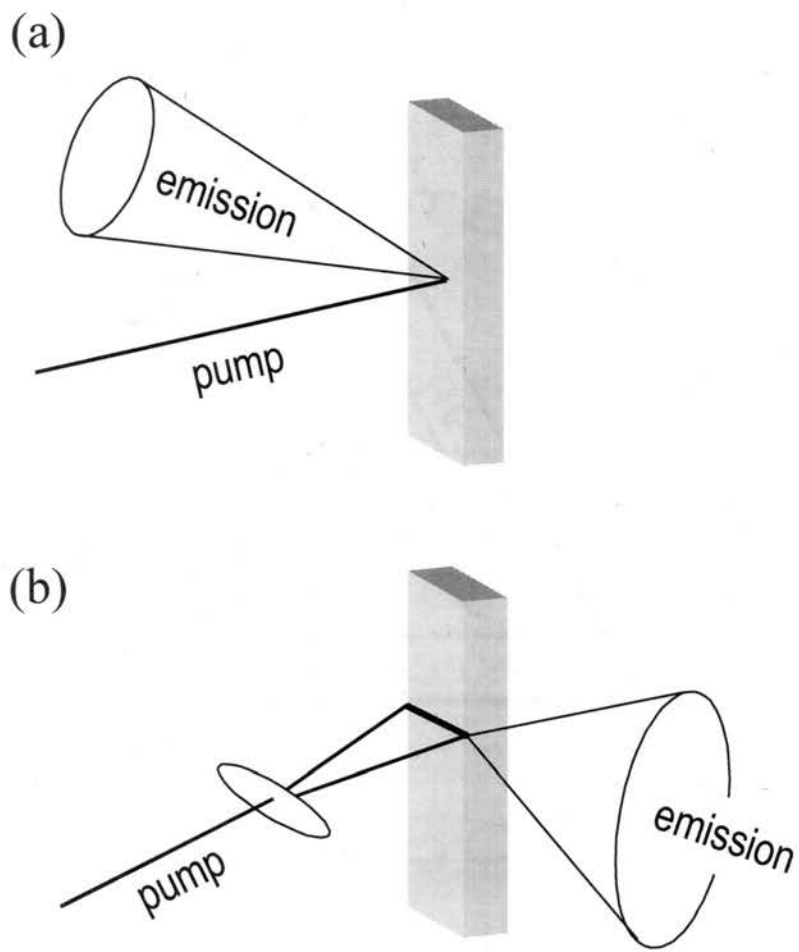


Figure 12. Schematic of (a) surface and (b) edge emission geometries.

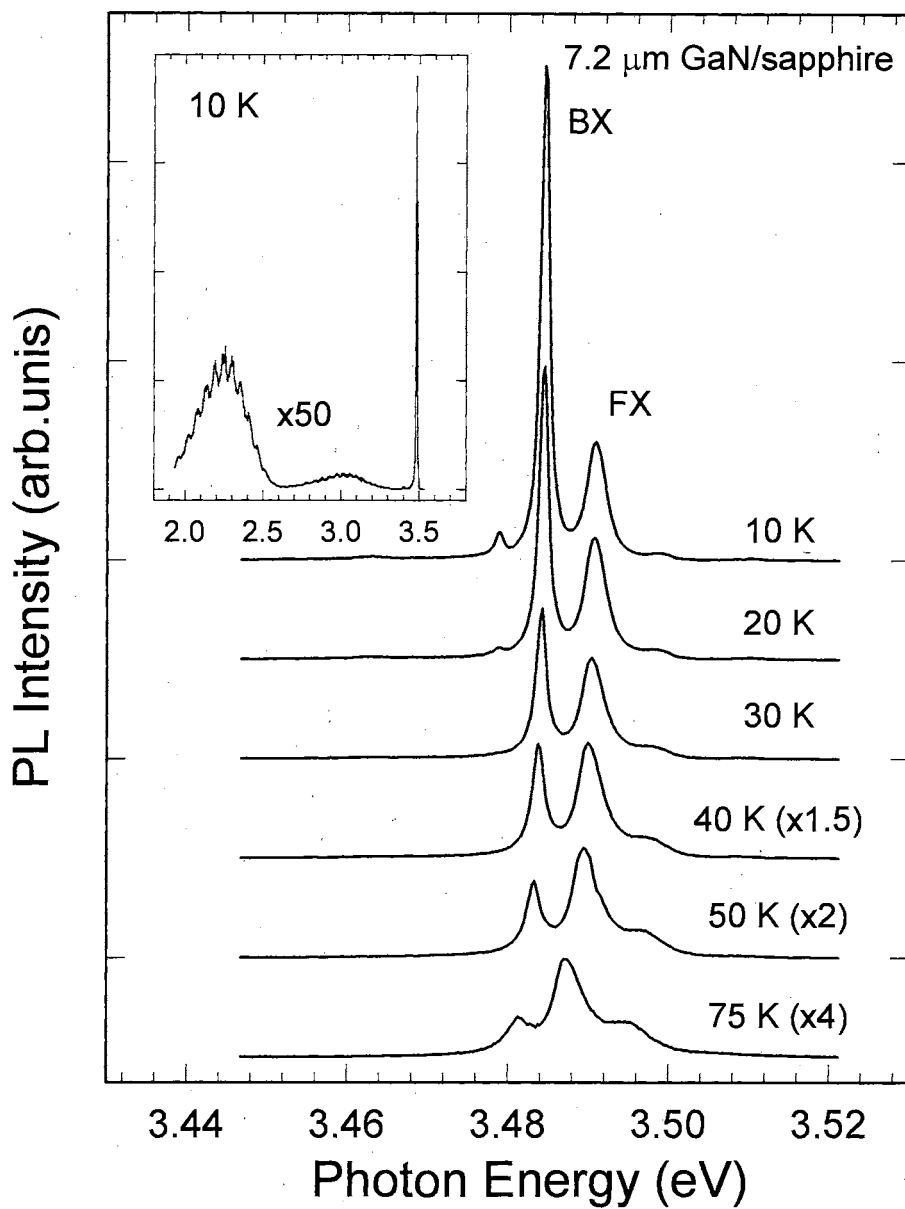


Figure 13. Temperature dependence of the excitonic PL emission from a 7.2 μm GaN epilayer grown on sapphire by MOCVD. As the temperature increases, the higher energy peak (labeled FX) becomes dominant, indicating it is due to free exciton transitions. The low energy peak (labeled BX) is seen to rapidly quench with increasing temperature, indicating it is due to bound exciton transitions.

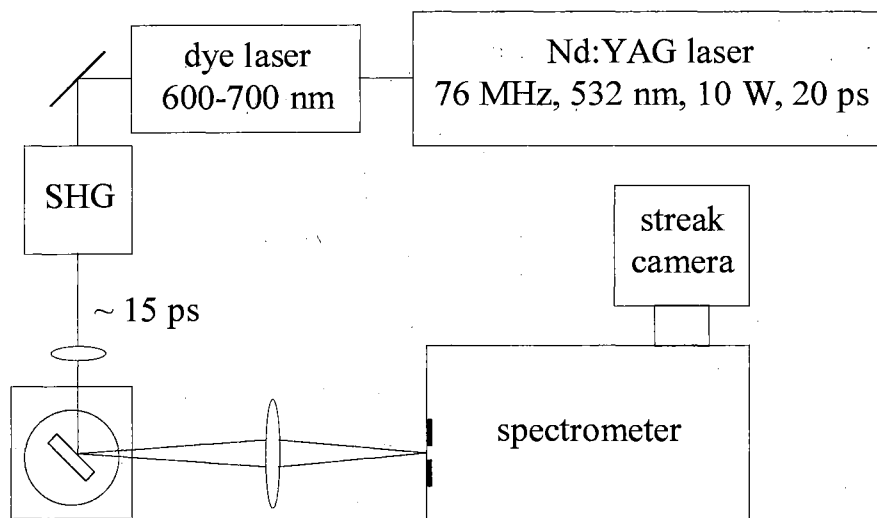


Figure 14. Typical time-resolved PL experimental setup.

Absorption

Absorption is a straightforward technique that measures the wavelength-dependence of the absorption coefficient of semiconductors. The typical absorption experimental setup is shown in Figure 15 (a). The broadband light from a Xe lamp is sent through a monochromator and scanned across the wavelength range of interest. The resultant monochromatic light is focused onto a spot on the sample, and the light passing through the sample is collected and focused into a PMT connected to a lock-in amplification system. Lock-in is attained by optically chopping the excitation light when it exits the monochromator. The amplifier looks for a signal from the PMT with the same frequency and phase as the chopped beam. This technique greatly reduces the noise signal from stray light entering the PMT. By scanning the excitation light across the bandgap region of the sample, we obtain an absorption spectrum. Absorption of light in a semiconductor is governed by Beer's Law:

$$I = I_o e^{-\alpha d}, \quad (3-4)$$

where I is the output intensity (the scan we just obtained), I_o is the incident intensity (obtained by scanning the lamp with no sample present), α is the absorption coefficient, and d is the sample thickness. When calculating absolute absorption values, the reflection of the incident light from the sample surface must be taken into account. A unitless parameter called the optical density (OD) is often used when the thickness of the sample is unknown. OD is given by:

$$\text{OD} = \alpha d = -\ln\left(\frac{I}{I_o}\right) \quad (3-5)$$

which is just the absorption coefficient times the thickness.

The thickness of the sample is very important in absorption measurements, not only because it is necessary for the correct calculation of α , but also because it can determine whether or not any photons can be observed. If the sample is too thick, so many of the incident photons above the bandgap of the semiconductor are absorbed that the instruments cannot measure the small number that do make it through. For the setup shown in Figure 15, this typically happens for a value of OD = 6. Using an excitonic absorption coefficient of $\alpha = 1.5 \times 10^6 \text{ cm}^{-1}$ for GaN, the thickest sample that can be measured is $d = 0.4 \text{ }\mu\text{m}$.

Absorption is an extremely powerful method of studying excitons in semiconductor materials. The inset of Figure 16 shows the 10 K absorption spectrum of a 0.38 μm -thick GaN epilayer, with strong excitonic transitions evident. This data can be fit to find precise values of the excitonic and band-to-band transition energies for the A, B, and C bands. The excitonic (α_{exc}) and band-to-band (α_{bb}) contributions to absorption, respectively, are given by:

$$\alpha_{\text{exc}}(h\nu) = \sum_{n=1}^m \left[\frac{A_x}{n^3} \delta \left(h\nu - E_g + \frac{R_x}{n^2} \right) \right], \quad (3-6)$$

and

$$\alpha_{\text{bb}}(h\nu) = \frac{\gamma_x \alpha_o(h\nu)}{1 - \exp(-2\pi\gamma_x)}, \quad (3-7)$$

where α_o is described by:

$$\alpha_o = \frac{A_b E_g \sqrt{h\nu - E_g}}{h\nu \sqrt{R_x}}, \quad (3-8)$$

and γ_x is given by:

$$\gamma_x = \sqrt{\frac{R_x}{h\nu - E_g}}. \quad (3-9)$$

In the above equations, E_g is the bandgap energy, A_b is the absorption intensity just above E_g , R_x is the exciton binding energy, $h\nu$ is the incident photon energy, n is the order of the excited excitonic level, and A_x is the intensity of the $n = 1$ excitonic transition. The results of a fit to the 10 K absorption data of the 0.38 μm sample is shown in Figure 17. The data obtained from this fit are consistent with what is expected for the A , B , and C exciton and band-to-band transition energies.

Using this technique to obtain excitonic and band-to-band transition energies by studying α as a function of temperature can yield extremely accurate values of the Varshni coefficients; much more reliable than using PL results as described above. Furthermore, we can fit the temperature dependence of the width of the excitonic absorption lines to the following equation:

$$\Gamma = \Gamma_0 + \gamma_{ph}T + \frac{\Gamma_{LO}}{\exp(E_{LO}/k_B T) - 1}, \quad (3-10)$$

where Γ_0 represents contributions to the broadening from temperature independent mechanisms, γ_{ph} represents exciton-acoustic phonon interaction, and Γ_{LO} represents exciton-LO phonon broadening. Using an LO phonon energy (E_{LO}) of 91.7 meV, Fischer *et al* fit their data to this equation to yield $\Gamma_0 = 10$ meV, $\gamma_{ph} = 15$ $\mu\text{eV/K}$, and $\Gamma_{LO} = 375$ meV.⁸⁹ They also observed excitonic resonances significantly above RT, as shown in Figure 16, illustrating the applicability of the III-Nitrides for high temperature electronics.

Absorption measurements can also be used to gauge the degree of the band tail in a semiconductor alloy. The sharper the transition, the faster the rise in the absorption curve. Absorption measurements performed on InGaN alloy epilayers, seen in Figure 18, show a significant band tail as evidenced by a slow rise in the InGaN-related absorption, signifying the presence of alloy content fluctuations. The fringes seen on the solid curves are due to Fabry-Perot interference effects, discussed in detail in the next section.

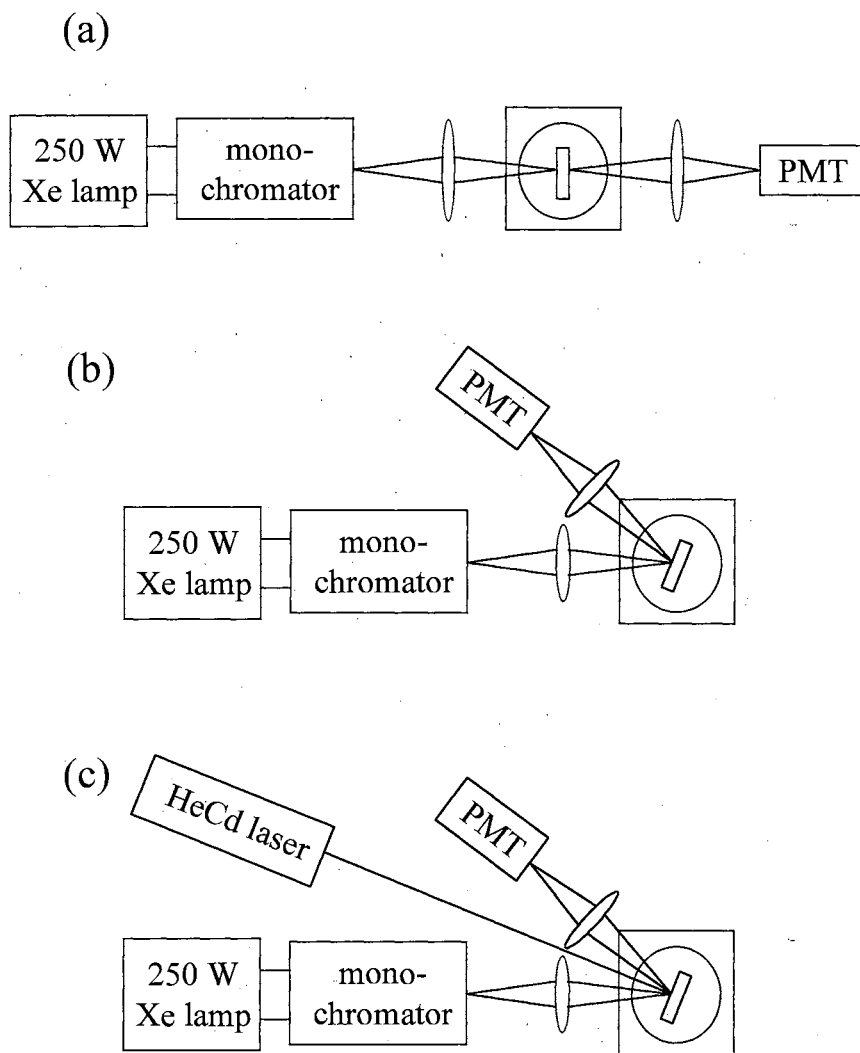


Figure 15. Experimental setups for the measurement of (a) absorption, (b) reflectance, and (c) photorefectance.

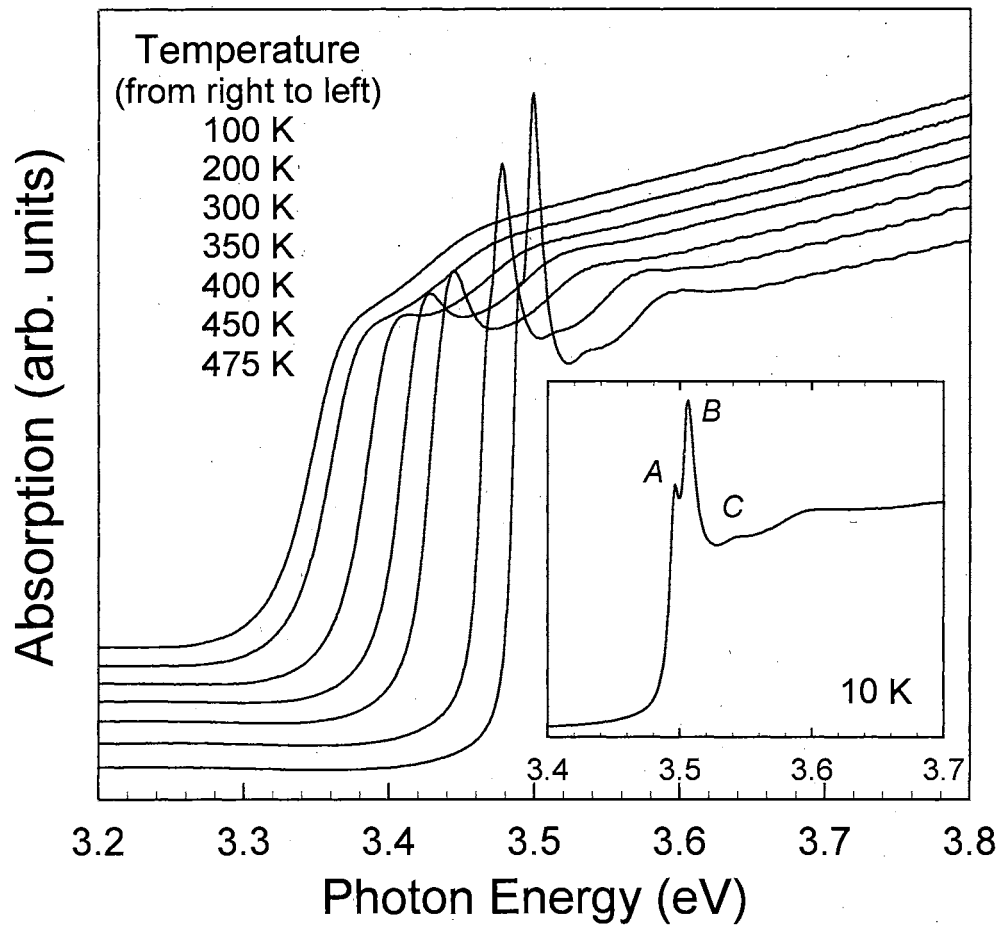


Figure 16. Absorption spectra of a 0.38 μm-thick GaN sample at selected temperatures from 100 K to 475 K. The inset shows the absorption spectrum at 10 K with the excitonic peaks labeled.

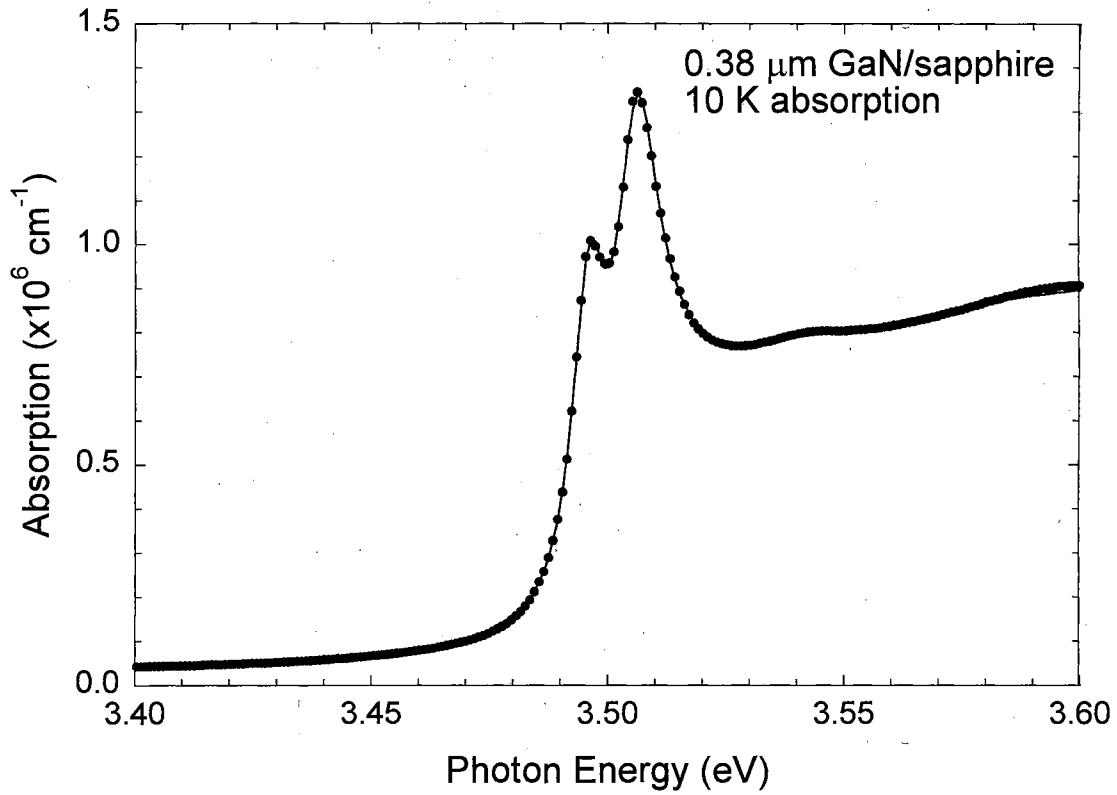


Figure 17. Results of the best least-squares fit of Equations 3-6 through 3-9 (solid line) to the experimental 10 K absorption spectrum (solid circles) of the 0.38 μm GaN epilayer shown in the inset of Figure 16.

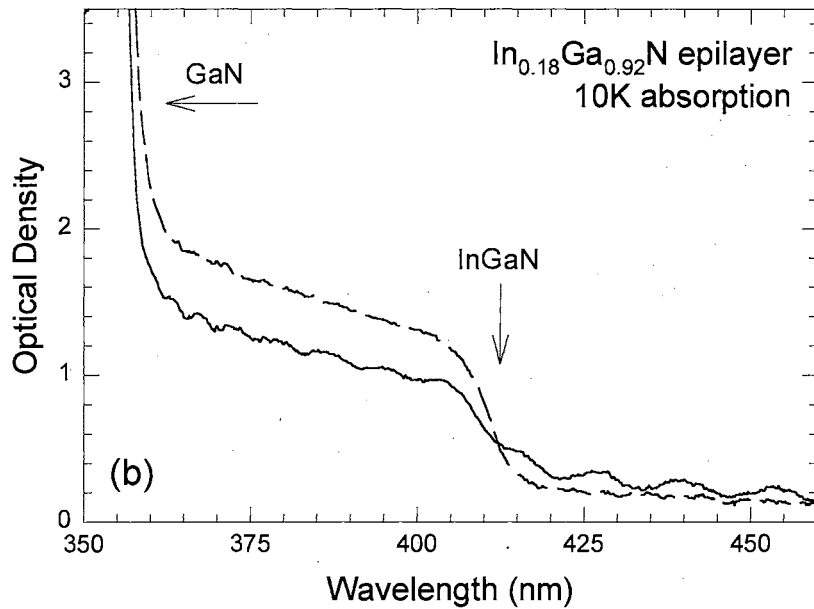
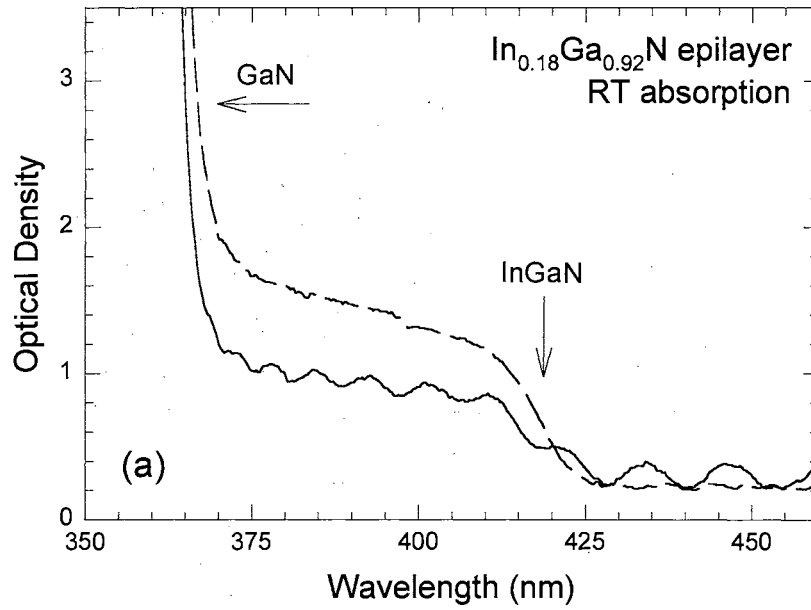


Figure 18. Absorption spectra for 50 nm (solid) and 100 nm (dashed) InGaN epilayers at (a) RT and (b) 10 K. A large degree of band tailing can be seen from the slow rise of the absorption spectra due to the alloy layers compared to GaN. The fringes seen in the solid curves are due to Fabry-Perot interference (see the Section on *Reflectance*).

Reflectance

Reflectance measurements are performed using a setup nearly identical to the one shown above for absorption. The only difference lies in the position of the sample and the detector, as can be seen in Figure 15 (b). For reflectance, the sample is tilted slightly in the plane of the optical table and the detector is rotated $\sim 180^\circ$ to measure the signal reflected from the sample surface. Scanning the incident light across the bandgap of the sample to get the reflectance spectrum yields information about the bandgaps in semiconductors. A typical 10 K reflectance spectrum is shown in Figure 19 (a) for a 3 μm thick GaN epilayer grown on an a -plane sapphire substrate by MOCVD. Resonances in the spectra indicate the energy positions of excitonic transitions. These transition energies can be precisely determined by fitting the data to the equation:

$$R(\nu) = R_0 + R_x \operatorname{Re} \left(\frac{h\nu_x - h\nu + i\Gamma_x}{\Gamma_x^2 + (h\nu - h\nu_x)^2} e^{i\Theta} \right), \quad (3-11)$$

where R_0 is the background, Θ is the phase, and R_x , $h\nu_x$, and Γ_x are the amplitude, transition energy, and broadening parameter, respectively, for the x exciton. Korona *et al* used this approach to find the A , B , and C exciton energies in homoepitaxial GaN epilayers.⁹⁰ However, as the temperature of the sample is increased, these resonances eventually broaden and become indistinguishable from one another. This is shown in Figure 19 (b) for a 1.9 μm thick GaN epilayer grown on a -plane sapphire.

Figure 19 also shows wavelength dependent interference fringes, which arise from the Fabry-Perot cavity created by the sapphire-GaN and GaN-air interfaces. The position of these fringes, marked by arrows, is linked to both the thickness of the Fabry-Perot cavity (*i.e.* the epilayer thickness), and the refractive index of the material. For a

single wavelength of light, assuming normal incidence, a valley in the reflectance is seen due to destructive interference whenever the following simple relation is satisfied:

$$2nd = m\lambda, \quad (3-12)$$

where n is the refractive index of the semiconductor, d is the thickness of the cavity, m is the interference order, and λ is the wavelength of the light. For a fixed thickness, if the wavelength is scanned we will see alternating peaks and valleys in the reflectance curve whenever the changing path length of the incident light causes constructive and destructive interference, respectively. If we knew the actual order of the fringes observed in reflectance measurements (the first one we observe is not necessarily $m = 1$), we could calculate the index of refraction by assuming a sample thickness, or better yet, measuring the thickness using SEM. Luckily, there is a method we can use to determine the fringe order. If we assume the refractive index is independent of wavelength far away from the bandedge, then a plot of m (with the first observed valley being $m = 1$) vs. $1/\lambda$ should yield a straight line in this region, with the y -intersection giving the correct $m = 0$ value. After shifting the preliminary values of m to match this, we can use Equation 3-12 to calculate n . The results of this technique are shown in Figure 20 for three GaN samples of different thickness on sapphire. What is observed is that close to the bandedge, the index of refraction shows a drastic increase. This so-called dispersion of the refractive index is extremely important when dealing with wavelengths of light close to the bandgap of a semiconductor, such as in LDs. It is a necessity in the engineering of DHs and SCHs, where the difference in refractive indices of the waveguide and cladding regions at the emission wavelength must be known.

Photoreflectance

A typical photoreflectance (PR) setup is pictured in Figure 15 (c). The only change from reflectance is the addition of a weak modulating laser beam. The difference between conventional reflectance and PR is that the latter is a differential method utilizing a modulation of the built-in electric field through photoinjected carriers by a

periodically modulated light beam, such as a chopped HeCd laser beam. The change in reflectivity, $\Delta R/R$, due to the modulation may be expressed as:

$$\frac{\Delta R}{R} = a\Delta\varepsilon_1 + b\Delta\varepsilon_2, \quad (3-13)$$

where a and b are referred to as Seraphin coefficients and are related to the unperturbed dielectric function $\varepsilon = \varepsilon_1 + \varepsilon_2$, while $\Delta\varepsilon_1$ and $\Delta\varepsilon_2$ are the changes in the real and the imaginary parts of the modulated dielectric function, respectively.⁹¹ The differential changes in the reflectivity appear as sharp derivativelike lineshapes in the modulated reflectance spectrum, corresponding to specific transitions in the Brillouin zone. Typical PR spectra are shown in Figure 21, as a function of temperature, for an $\text{In}_{0.13}\text{Ga}_{0.87}\text{N}$ epilayer grown on sapphire by MOCVD with a GaN buffer layer. The transition at lower energy is due to band-to-band transitions in the alloy layer, and is significantly broadened due to fluctuations in the alloy content. This sample also exhibits a group of transitions at higher energy which are much narrower than the lower energy peak, and are due to the various excitonic transitions in the underlying GaN buffer layer.

Several additional experimental steps must be taken for PR measurements. First, the chopper is moved from the lamp light to the laser light. The lock-in amplifier automatically measures the difference in the reflectance with and without modulation, simplifying the measurement (we don't have to take a reflectance scan with the laser, take a reflectance scan without the laser, then take the difference). Secondly, the laser power must be made low so as not to excite too much PL from the sample. There is no spectrometer between the sample and the PMT, so the entire spectrum of the PL signal contributes to a background level for PR. A balance between this PL background and the modulation field strength must be found. Thirdly, a bandpass filter must be used to block the scattered laser light, which would saturate the PMT, but must still allow significant transmittance in the bandgap region. Lastly, care must be taken to overlap the lamp and laser spots on the sample surface.

In order to determine the energy positions associated with the various observed optical transitions and identify those unknown spectral features, the PR spectral features are fitted to the functional form:^{92,93,94}

$$\frac{\Delta R}{R} = \text{Re} \left[\sum_j C_j e^{i\theta_j} (E - E_j + i\Gamma_j)^{-m} \right], \quad (3-14)$$

where C_j and θ_j are the amplitude and phase of the lineshape, and E_j and Γ_j are the energy and the empirical broadening parameter of the j th transition, respectively. The exponent m is a characteristic parameter that depends on the type of critical point and the order of the derivative. The values of $m = 5/2$ and 2 , which correspond to three-dimensional interband and excitonic transitions, respectively, are generally used to fit the derivativelike spectral structures.^{92,95}

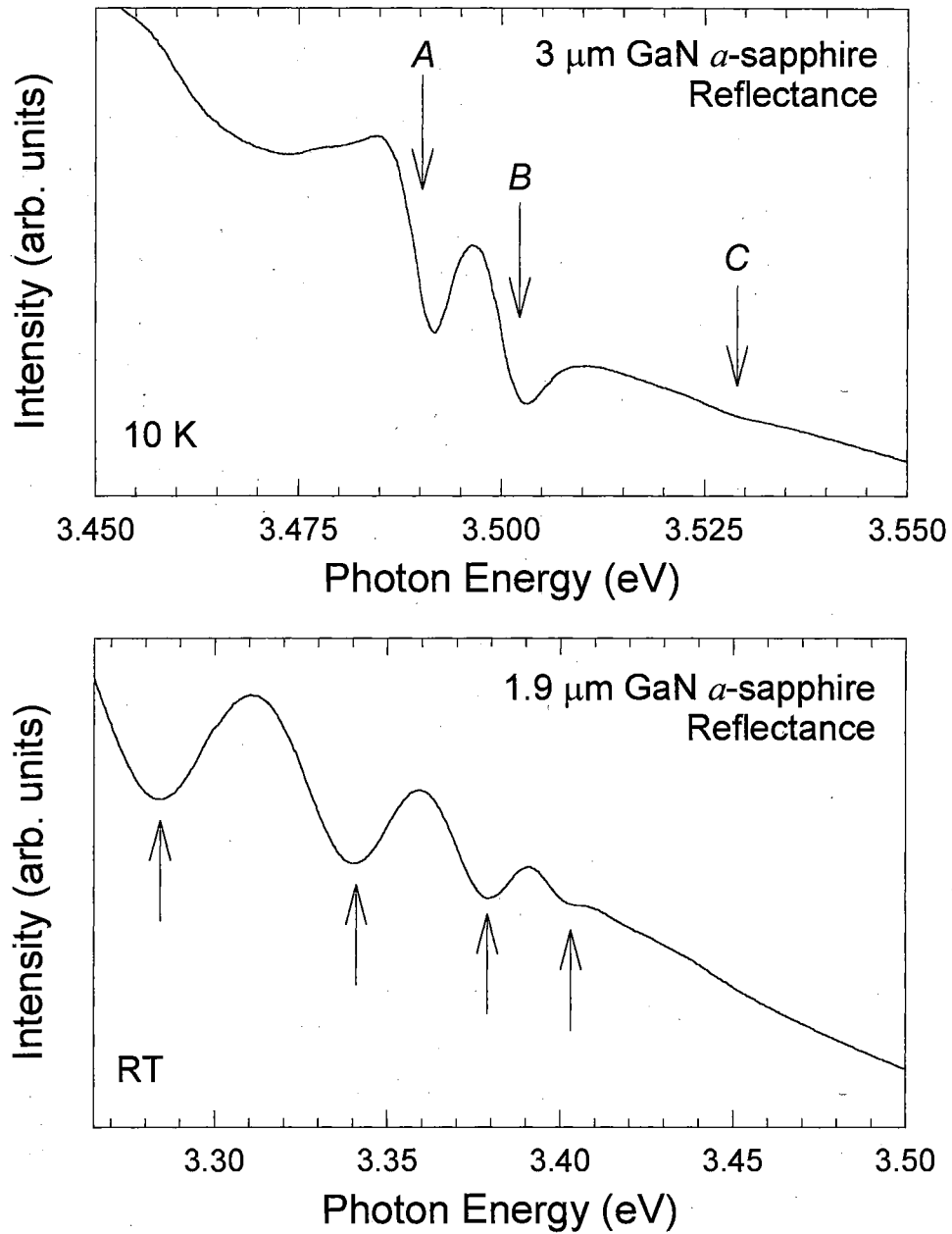


Figure 19. Typical reflectance data. The top curve shows 10 K reflectance data from a 3 μm GaN epilayer with *A*, *B*, and *C* excitons marked with arrows. The bottom curve shows RT reflectance taken from a 1.9 μm GaN epilayer, with valleys due to Fabry-Perot interference marked with arrows. Both samples were grown on *a*-plane sapphire by MOCVD.

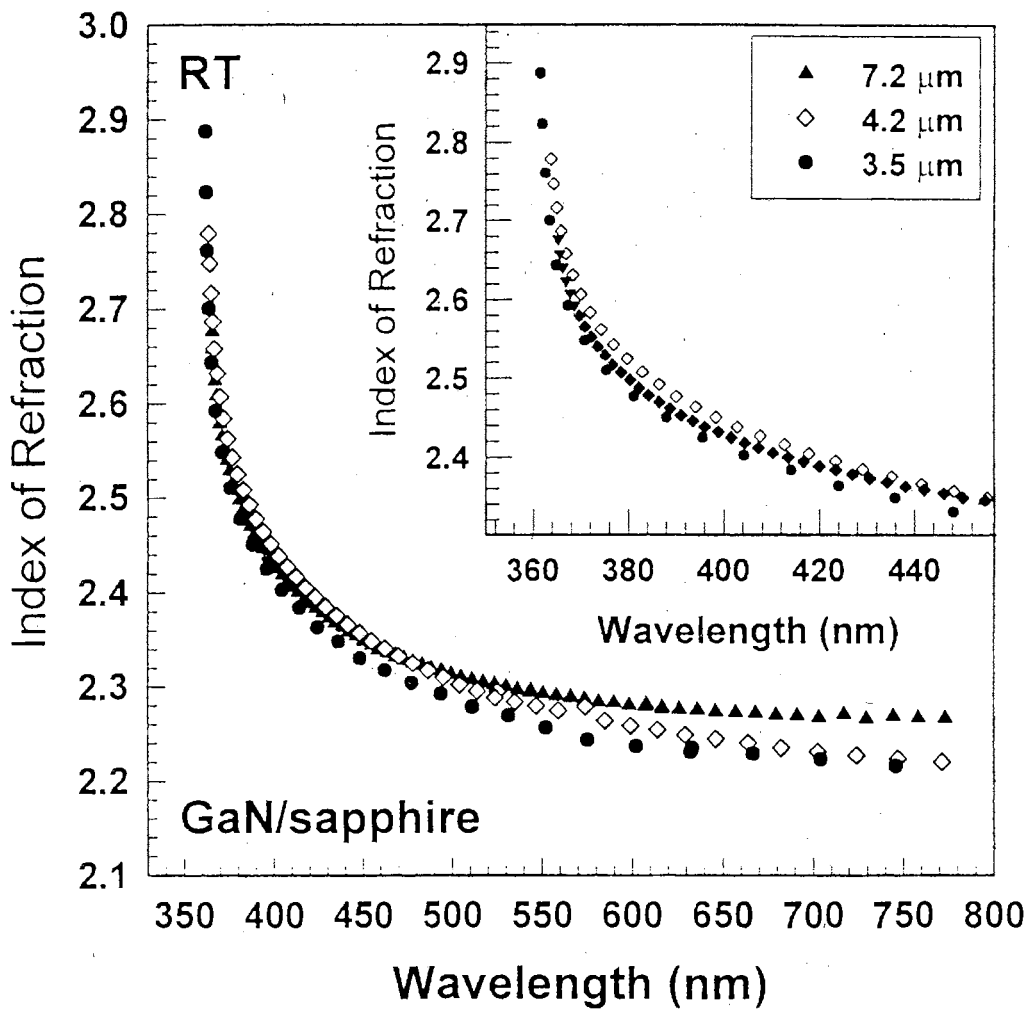


Figure 20. Refractive index at RT for several GaN films of different thickness grown on sapphire by MOCVD. The inset shows a narrower region near the bandgap of GaN.

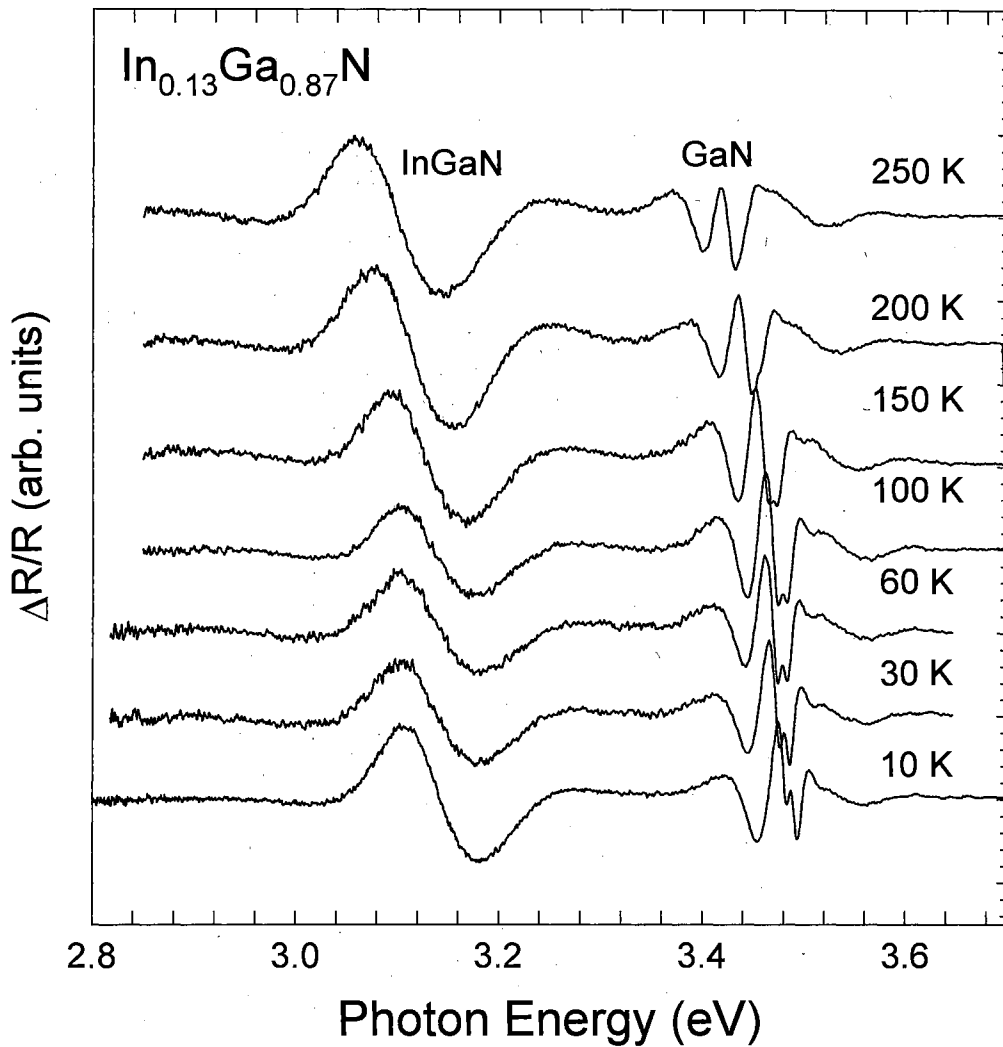


Figure 21. PR spectra of an $\text{In}_{0.13}\text{Ga}_{0.87}\text{N}$ epilayer as a function of temperature. The signal labeled GaN is from an underlying buffer layer.

Photoconductivity

Photoconductivity (PC) measurements might be best described as absorption measurements where we use the sample under investigation as the detector instead of a PMT. If the incident light is above the bandgap of the sample, absorption of a photon creates an electron and a hole. These photoexcited carriers cause a change in the conductivity of the sample, which is measured by monitoring the voltage drop across a resistor in series with the sample and a battery. An amplifier locked-in to the excitation lamp via a chopper is used to increase the signal to noise ratio and to avoid measuring current originating from other sources, such as stray light and thermal carrier generation. A typical PC experimental system is shown in Figure 22 (a). The sample is connected to the external circuit via metallic contacts deposited on the surface of the sample. Figure 22 (b) shows one of the most common contact schemes – metal-semiconductor-metal (MSM) fingers. To maximize the signal measured by the digital multimeter (DMM), the sample is excited within the dotted circle on the figure. By scanning the wavelength of the exciting light, we can study the spectral response of the sample.

A typical result of this procedure is shown in Figure 23, at a temperature of 10 K for a 0.4 μm GaN epilayer grown on sapphire by MOCVD. As seen in the figure, there is no PC signal when the excitation wavelength is below the bandgap energy of GaN. As the wavelength approaches the bandgap, the PC signal starts to increase due to the creation of electron-hole pairs. The peaks in the spectra are related to excitonic transitions in GaN, and will be discussed in more detail in the next chapter.

We can fit the wavelength dependent photocurrent spectra with the following equation,⁹⁶ originally proposed by DeVore:⁹⁷

$$I_{\text{PC}} = \frac{I \tau}{1 - (\alpha L)^2} \left(1 - e^{-\alpha d} + \frac{\alpha L (\alpha L e^{-\alpha d} - \alpha L - a e^{-\alpha d} - a)}{1 + a \coth(d/2L)} \right), \quad (3-15)$$

where I is the wavelength dependent light intensity, τ is the carrier lifetime, α is the wavelength dependent absorption coefficient, L is the diffusion length, and the parameter $a = s\tau/L$, where s is the surface recombination velocity. This spectrum is strongly dependent on the shape of the absorption coefficient. Accordingly, we describe the absorption of the sample using Equations 3-6 through 3-9. Alternatively, to reduce the number of coefficients in the fitting process, we can plug the experimental absorption curve into Equation 3-15. The fitting of PC data is presented in more detail in the next chapter.

PC measurements are the standard method of characterizing photodetectors. Valuable information such as the peak detection wavelength, cutoff wavelength (especially important for solar-blind PDs), and quantum efficiency can be obtained through the analysis of PC results. As shown in Chapter IV, PC can also serve as a powerful spectroscopic tool. Several interesting effects have been observed through PC spectroscopy. For instance, the excitonic resonance in GaAs epitaxial layers at 10 K was observed to switch from a peak to a dip in the PC spectrum as the thickness of the epilayer was increased.⁹⁸ The calculated results for this phenomenon are shown in Figure 24. This effect occurs because as the absorption increases (for a thick sample), the carriers are created closer to the surface, leading to a faster recombination lifetime. For a thin sample, the carriers are always created near the surface.

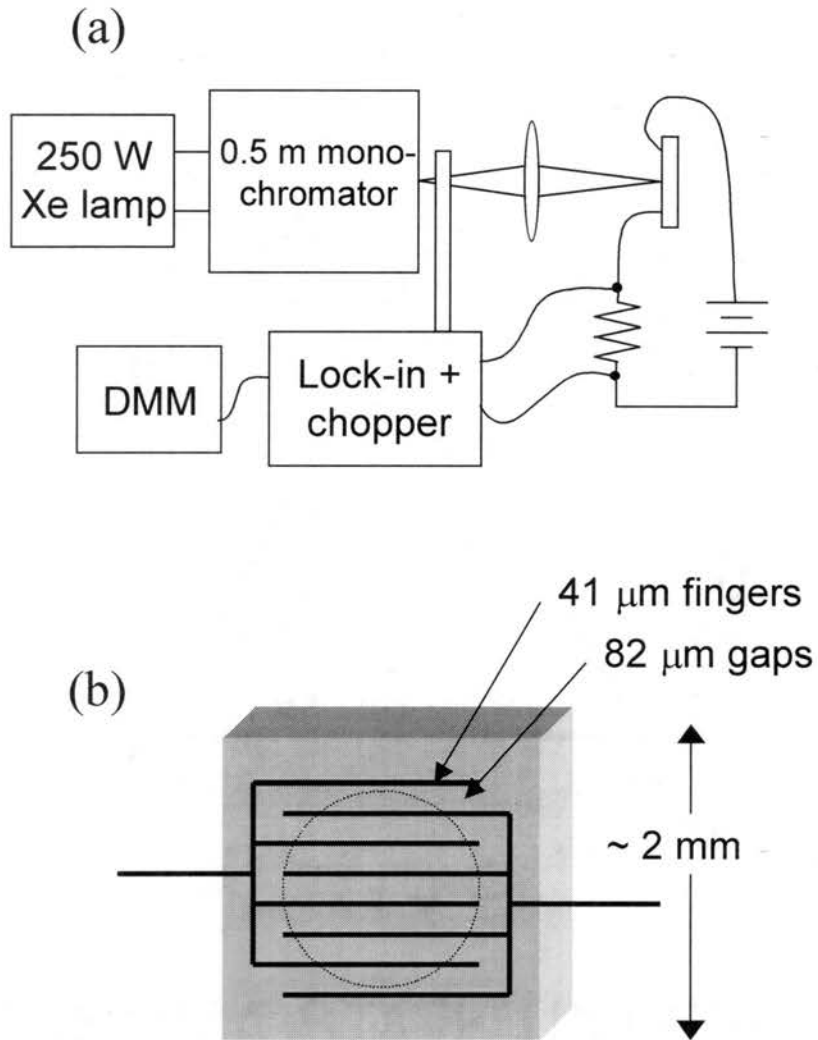


Figure 22. (a) Typical experimental setup for the measurement of photoconductivity. (b) Metal-semiconductor-metal (MSM) contact scheme. The dotted line indicates the excited region.

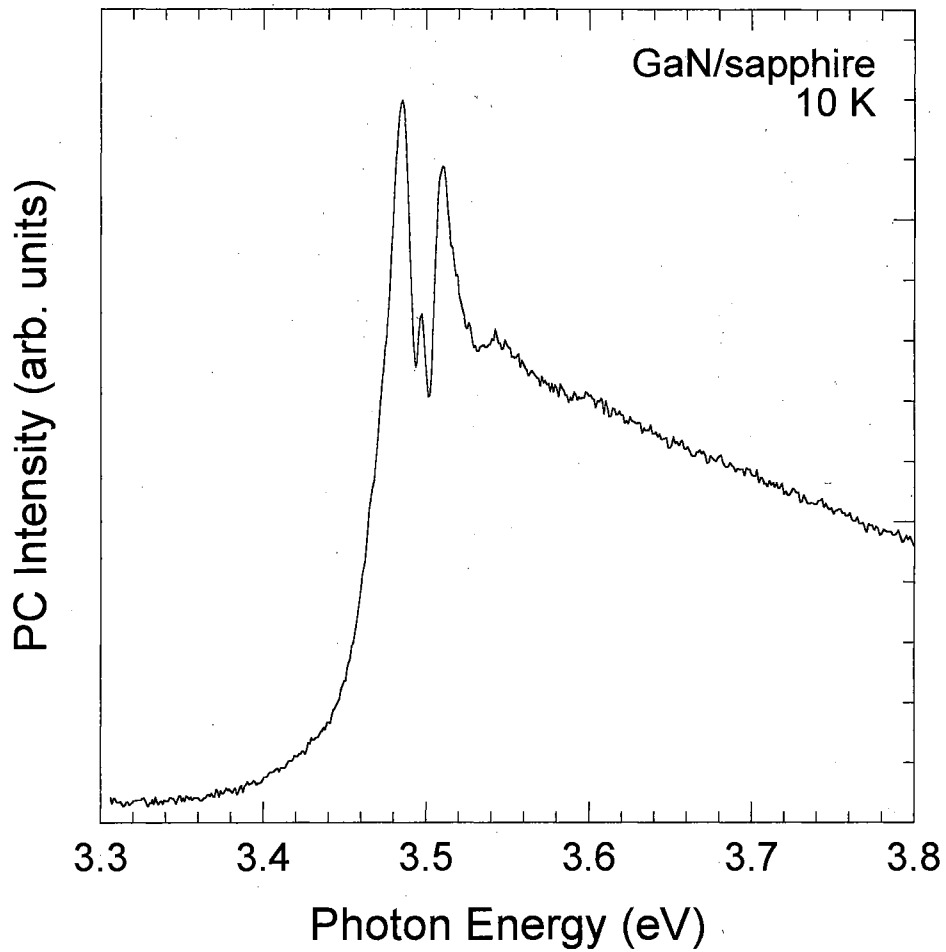


Figure 23. Typical data from photoconductivity experiments. The result presented was taken at 10 K from a 0.4 μm GaN epilayer grown by MOCVD on sapphire, with an MSM contact scheme. A voltage of 40 V was applied to the sample, and the photocurrent was measured across a 2 M Ω resistor.

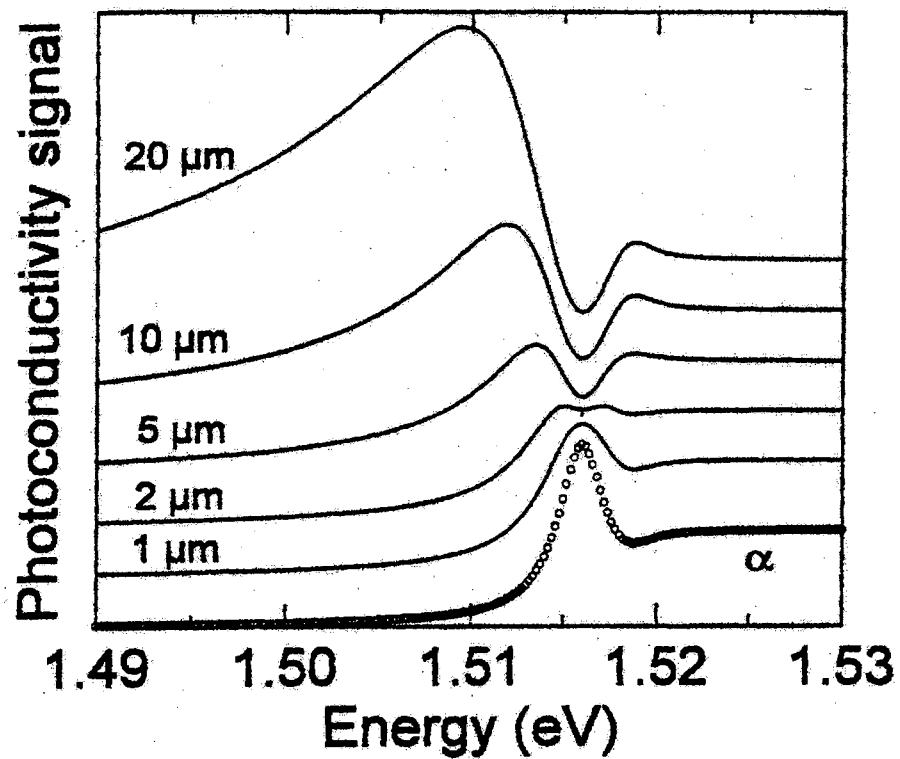


Figure 24. PC spectra of GaAs epitaxial layers of varying thickness. As the thickness increases, the excitonic resonance changes from a peak in the spectrum to a dip. The bottom curve (open circles) is the calculated 10 K absorption spectrum for the samples.

Stimulated Emission and Lasing

First, let's discuss the difference between stimulated emission (SE) and lasing. Both of these terms fall under the category of optical pumping experiments. The terms SE and lasing are often interchanged, and there is really no clear-cut distinction between the two. SE is the physical process of light emission, whereas lasing (light amplification by the stimulated emission of radiation) takes advantage of the SE process to build up the light output. The term lasing is used whenever optical feedback is present. This is often identified by the observation of modes in the output spectra, which result from an optical cavity. The mode spacing $\Delta\lambda$ is related to the cavity length L through the following equation:^{99,100}

$$\Delta\lambda = \frac{\lambda_o^2}{2L(n - \lambda_o dn/d\lambda)}, \quad (3-16)$$

where λ_o is the wavelength of a mode, n is the refractive index at λ_o , and $dn/d\lambda$ is the dispersion of the refractive index as described above. This cavity can be intentional, such as mirror-coated facets or cleaved laser bars, or it can be "accidental," as in the case of cracks in the epilayer or the surfaces of microstructures such as self-formed pyramids.

The experimental setup for the study of SE and lasing is similar to that of PL, since we are looking at the light emitted from a sample that is being excited by a laser. A typical experimental setup is shown in Figure 25 for four possible pumping configurations. The laser used in optical pumping, however, must be pulsed rather than cw. The reason for this is that to observe SE, we need to create a population inversion in the sample, *i.e.* there must be more free carriers in the conduction band than in the valence band. Because photoexcited carriers relax back down to the valence band via radiative or nonradiative recombination over a time scale that is typically in the ns or ps

range, we must use a pulsed laser to create a population inversion before the carriers have a chance to decay. Additionally, the peak intensity of this laser pulse must be large enough to excite a sufficient number of carriers into the conduction band. Thus, chopping a cw laser beam or using an ultrafast shutter to obtain pulses is not an option. The excitation density of the pump pulse is typically measured in kW/cm². For comparison, a pulsed laser focused to a 1 mm² spot with an average power of 5 mW, a pulse duration of 10 ns, and a repetition rate of 10 Hz has a peak intensity of 5000 kW/cm². Over this same time scale, a cw laser running at 5 mW would only give us 5×10^{-9} W/cm².

Four laser excitation sources have been used in the research presented in this thesis. The first consists of a XeCl excimer laser (~ 10 ns pulsewidth and 10 Hz repetition rate at 308 nm). The second is a tunable dye laser pumped by the above-mentioned excimer laser. The excimer-pumped dye laser emitted directly in the UV with a pulse duration of ~ 8 ns. The third source was an injection-seeded Nd:YAG laser ($\lambda = 1.064 \mu\text{m}$, 6 ns, 30 Hz), which could be tripled to 355 nm or quadrupled to 266 nm using a nonlinear crystal. Finally, the 532 nm second-harmonic of this Nd:YAG laser could be used to pump a tunable dye laser, whose 600-700 nm output was subsequently doubled into the UV using another nonlinear crystal. SE experiments are performed in the edge-emission geometry, pictured in Figure 12 (b). The UV laser excitation source is focused to a line on the sample surface using a cylindrical lens. This forms a gain region that amplifies the SE signal before it is emitted through the edge of the sample. A continuously variable ND filter is used to attenuate the laser power. The resultant emission is collected from the edge of the sample and focused onto the slits of a 1 meter spectrometer and detected by either a UV-enhanced CCD or an optical multichannel analyzer (OMA), which is a linear diode array, *i.e.* a one-dimensional CCD.

SE in semiconductors is characterized by a threshold, which occurs at the point that the gain in the cavity equals the losses. Below this threshold, we only observe spontaneous emission. Above this threshold, a new peak (or peaks) appears at the maximum of the gain curve. This new peak increases superlinearly in intensity and narrows with increasing excitation intensity. Figure 26 illustrates the nature of SE in GaN epilayers. A strongly superlinear increase can be seen in the integrated emission

intensity with increasing excitation power. SE in an InGaN MQW is shown in Figure 27. This sample illustrates the striking difference between stimulated and spontaneous emission spectra.

SE experiments are indispensable for research on potential new lasing materials, as well as for the characterization of LDs. Rather than go through the extremely expensive and time-consuming process of fabricating an LD just to test if it works or not (in the research and development stage, this can be a colossal undertaking), we can utilize optical pumping experiments. If the LD structure exhibits optically pumped SE/lasing with a reasonable threshold value, creating a successful device lies only in the matter of fabrication (etching, photolithography, contacts, *etc.*). We have cleared the device structure and material quality of any culpability if the LD fails to work properly.

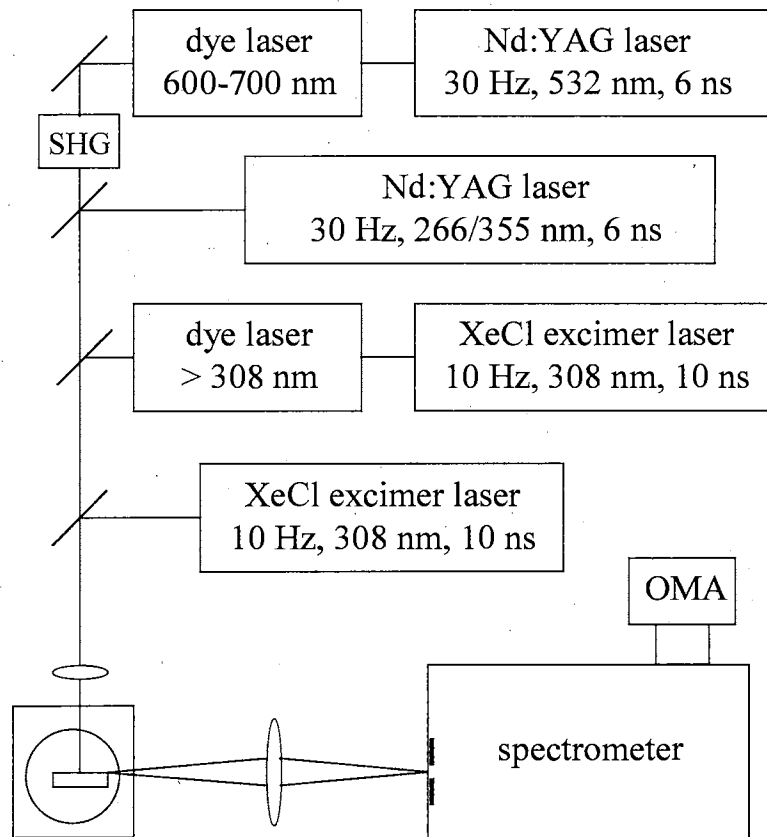


Figure 25. Typical stimulated emission/lasing experimental setup shown for four different pump laser configurations.

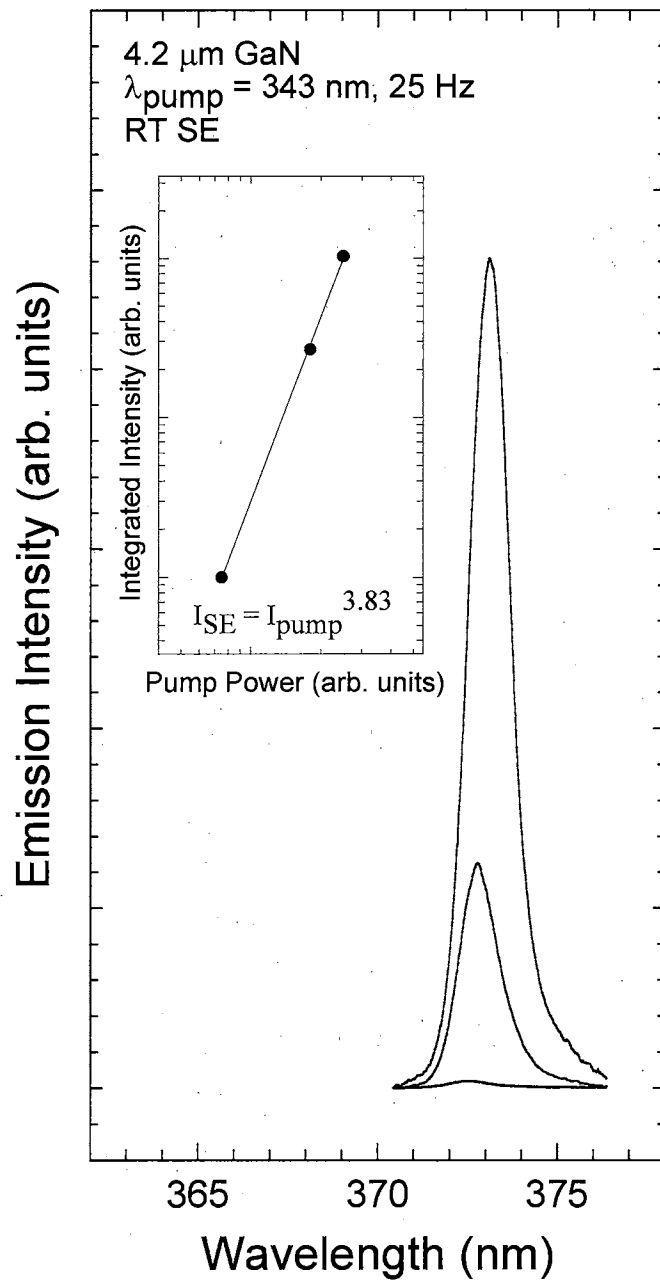


Figure 26. SE spectrum of a 4.2 μm GaN sample at various excitation intensities above the SE threshold. The inset shows the integrated intensity of the emission versus the pump power, illustrating the superlinear increase of the SE signal.

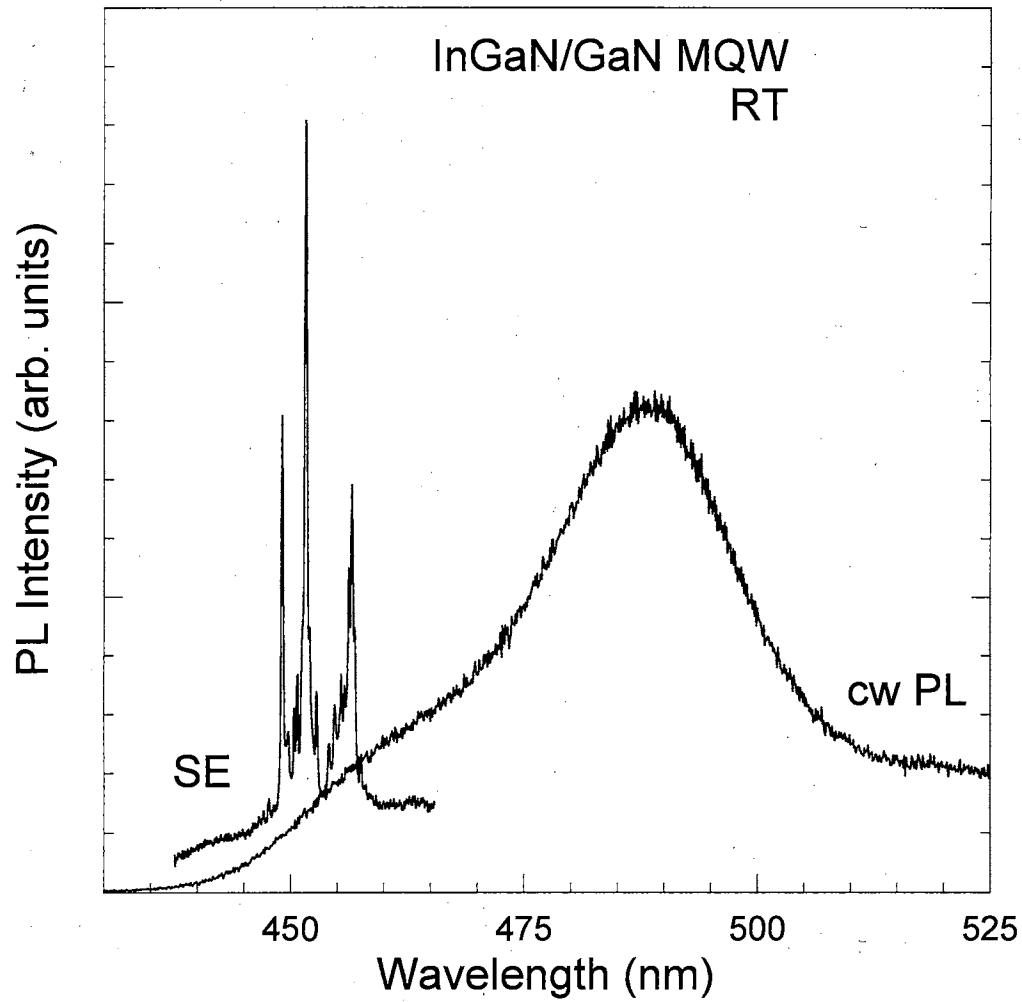


Figure 27. RT stimulated and spontaneous emission spectra from an InGaN/GaN MQW sample. The 308 nm emission from a XeCl excimer laser was used as the pump source. Note the narrowness of the SE peaks.

CHAPTER IV

EXCITONS IN GaN

Besides being physically interesting entities in their own right, excitons play an extremely significant role in the performance of semiconductor devices. It is important to study the properties of excitons to be able to design and grow optoelectronic devices that efficiently utilize them. This chapter presents the results of several experimental studies of excitonic transitions in GaN epilayers performed through a variety of spectroscopic techniques.

Binding Energy for the Intrinsic Excitons in Wurtzite GaN

In this section we present the results of an experimental study of the optical transitions associated with the ground and excited states of excitons in GaN epilayers using reflectance and photoreflectance measurements at low temperatures. We precisely determined the energy positions for the $1s$ and $2s$ states of the A , B , and C exciton transitions, as well as the fundamental band-to-band ($\Gamma_9^V - \Gamma_7^C$) transition. This was accomplished through the fitting of sharp derivativelike PR spectral features related to these transitions. Using this technique, it was possible to directly estimate the binding energy of the excitons using the hydrogenic model.

The GaN samples used in this work consisted of nominally undoped single-crystal wurtzite heteroepitaxial films grown by MOCVD on both (0001) sapphire and SiC

substrates. AlN buffer layers were deposited on the substrates at a temperature of 775 °C before the growth of the GaN epilayers. The GaN epilayers were deposited at 1040 °C on top of the buffer layers. The PL and PR experimental setups used in this study were identical to those pictured in Chapter III.

Figure 28 shows the results of conventional reflectance measurements taken at 10 K from two GaN epilayers grown on sapphire with thicknesses of 7.2 and 4.2 μm , as well as from a GaN epilayer grown on SiC with a thickness of 3.7 μm . The reflection spectra exhibit three dominant resonances, which are labeled *A*, *B*, and *C* on the top curve, and correspond to intrinsic free-exciton transitions. The *A*, *B*, and *C* excitons are related to the $\Gamma_9^V - \Gamma_7^C$, Γ_7^V (upper band) $- \Gamma_7^C$, and Γ_7^V (lower band) $- \Gamma_7^C$ interband transitions in GaN, as pictured in Figure 6. The *C* exciton signatures appear very weak in the spectra because the transition is theoretically forbidden for incident light with a wave vector along the *c* axis ($\mathbf{k}\parallel c$) and a polarization perpendicular to the axis ($\mathbf{E}\perp c$).^{101,102} Most interestingly, there is a set of weak but resolvable spectral features marked by *a* and *b* in the spectral region on the high-energy side of the main *A* and *B* transitions in the reflection spectra, especially in the 7.2 μm sample. While the *A*, *B*, and *C* spectral features can be unmistakably identified with the intrinsic free exciton transitions,¹⁰³ the nature of the *a* and *b* features in Figure 28 is not immediately clear. We found that the energy separation between the *a* and *b* features is very close to the separation of the *A* and *B* exciton transitions. The individual distance between the *A* exciton and the *a* feature as well as the *B* exciton and the *b* feature was also found to be about the same. Similar properties were observed in the exciton spectrum of CdS by Thomas and Hopfield, which led to the determination of the binding energy for *A* and *B* excitons in the material by attributing the corresponding spectral features to $n = 2$ excited states of the exciton based on their polarization properties.¹⁰² However, it is very difficult to use a polarization dependent approach in this work because of the very limited thickness of the samples used and the poor signal-to-noise ratio of the *a* and *b* features in the reflection spectra. Fortunately, photomodulation spectroscopy provides us with an alternative approach capable of detecting weak signals so as to accurately determine their transition energies and make a positive identification of the nature of the transitions. Figure 29 shows PR spectra taken from samples of GaN on sapphire and SiC. The PR spectra consist of a

series of sharp structures corresponding to most of the observed spectral features in the reflectance spectra, and also exhibit a pronounced enhancement of the weak *a* and *b* spectral structures seen on the reflectance curves in Figure 28. The solid lines in Figure 29 are the best least-squares fits to the experimental data using Equation 3-14. We found that the energy positions and widths of the PR spectral features could only be fit using $m = 2$ due to their excitonic nature.

The energy positions for the *A*, *B*, and *C* exciton transitions in the GaN/sapphire sample shown in Figure 29 (a) are 3.491, 3.499, and 3.528 eV, respectively. These values are higher than those obtained from virtually strain-free bulk GaN reported in Refs. [104], [105], and [106] due to the effects of residual strain caused by the mismatch of lattice parameters and thermal expansion coefficients between the GaN epilayer and the substrate.^{107,108,109} The best fits to our data result in an energy separation of 0.008 eV between the *a* and *b* features, which is almost identical to the *A-B* separation, and a 0.016 eV difference for both *A-a* and *B-b* separations with an experimental error of 0.001 eV. Similar properties were also observed in the other GaN samples: while the absolute energy position for the main *A* and *B* exciton transitions varies from sample to sample slightly due to the influence of residual strain, the energy differences between the *A-a* and *B-b* features were found to be ~ 0.016 eV for all the samples, and the energy separation between the *a* and *b* features was found to closely follow the separation between the main *A* and *B* exciton features at lower energies for each individual sample. These observations indicate that the *a* and *b* features are indeed associated with the *A* and *B* exciton transitions. Therefore, we attribute the *a* and *b* spectral features to the $n = 2$ excited states ($2s$) of the excitons. Such identifications permit a direct estimate of the binding energy for *A* and *B* excitons from the separation between the $n = 1$ and $n = 2$ states for excitons, assuming the hydrogenic model based on the effective mass approximation is applicable. According to Elliott's theory, exciton energy levels are given as:¹¹⁰

$$E_n = -\frac{E_b}{n^2}, \quad (4-1)$$

where n is an integer denoting the order of the excited state and E_b is the exciton binding energy. From the results presented above, we obtain a binding energy of $E_b \approx 0.021 \pm 0.001$ eV for both A and B excitons. This can be further manifested by the result of a theoretical fitting of the extra spectral structure in the portion of the PR spectrum between the a and b features. We found that it is necessary to introduce one more oscillator with a third-derivative lineshape to improve the fit to the experimental data. The good agreement between the theoretical fit and the observed spectrum indicates a spectral feature corresponding to a band-to-band transition at 3.512 eV. The approximate 0.021 eV energy separation between this band-to-band signature and the transition energy of the $n = 1$ state of the A exciton is consistent with the estimated binding energy. Therefore, this extra structure must originate from the $\Gamma_9^V - \Gamma_7^C$ transition, as denoted in Figure 29 (a), which corresponds to the $n = \infty$ state for the excitonic transition.

The binding energy for the C exciton can be derived from the theoretical fit to the PR spectrum taken from the 3.7 μm GaN sample grown on SiC as shown in Figure 29 (b) using the approach described above. This sample exhibits a much stronger C exciton transition signal in the reflection spectrum, as shown in the inset of the figure, compared to the samples of GaN on sapphire. The energy positions for the A , B , and C exciton transitions in this sample are 3.470, 3.474, and 3.491 eV, respectively. In addition to the derivativelike spectral features arising from the transitions associated with the $n = 1$ exciton states of the A , B , and C excitons, the spectral features related to the transitions involving the $n = 2$ excited states of the A and C excitons could be clearly observed in the PR spectrum. The best fit yields a 0.0172 eV energy separation between the $1s$ and $2s$ states of the C exciton, which corresponds to a binding energy of ~ 0.023 eV, and retains an energy difference of ~ 0.016 eV between the A exciton ($n = 1$) and a feature as indicated in the figure.

It should be pointed out that the exciton binding energies given above are estimated under the assumption of an isotropic reduced spherical mass for the excitons in GaN. In reality, wurtzite GaN is a hexagonal crystal with axial symmetry. The effective-mass equation for hydrogenic states should, in principle, be modified because the reduced effective mass as well as the dielectric constant is actually anisotropic. Nevertheless, the results presented here are in good agreement with the theoretical values obtained by

variational calculations (20.3 meV)¹¹¹ and perturbation theory (19.8 meV)¹¹² based on the hydrogenic model. In addition, a reduced effective exciton mass μ can be derived from our results with the relation:

$$E_b = \frac{e^4 \mu}{2(4\pi\hbar\varepsilon)^2} = 13.60 \mu / \varepsilon^2 \text{ eV}, \quad (4-2)$$

using a low frequency dielectric constant of $\varepsilon = 9.5$, to be $\mu \approx 0.15 m_0$. The obtained value is consistent with the value of $\sim 0.16 m_0$ estimated using an effective mass of $0.2 m_0$ for the electrons and $0.8 m_0$ for the holes in wurtzite GaN. Therefore, the simple hydrogenic series of Equation 4-1 is still a valid approach for the determination of the binding energy of excitons in GaN.

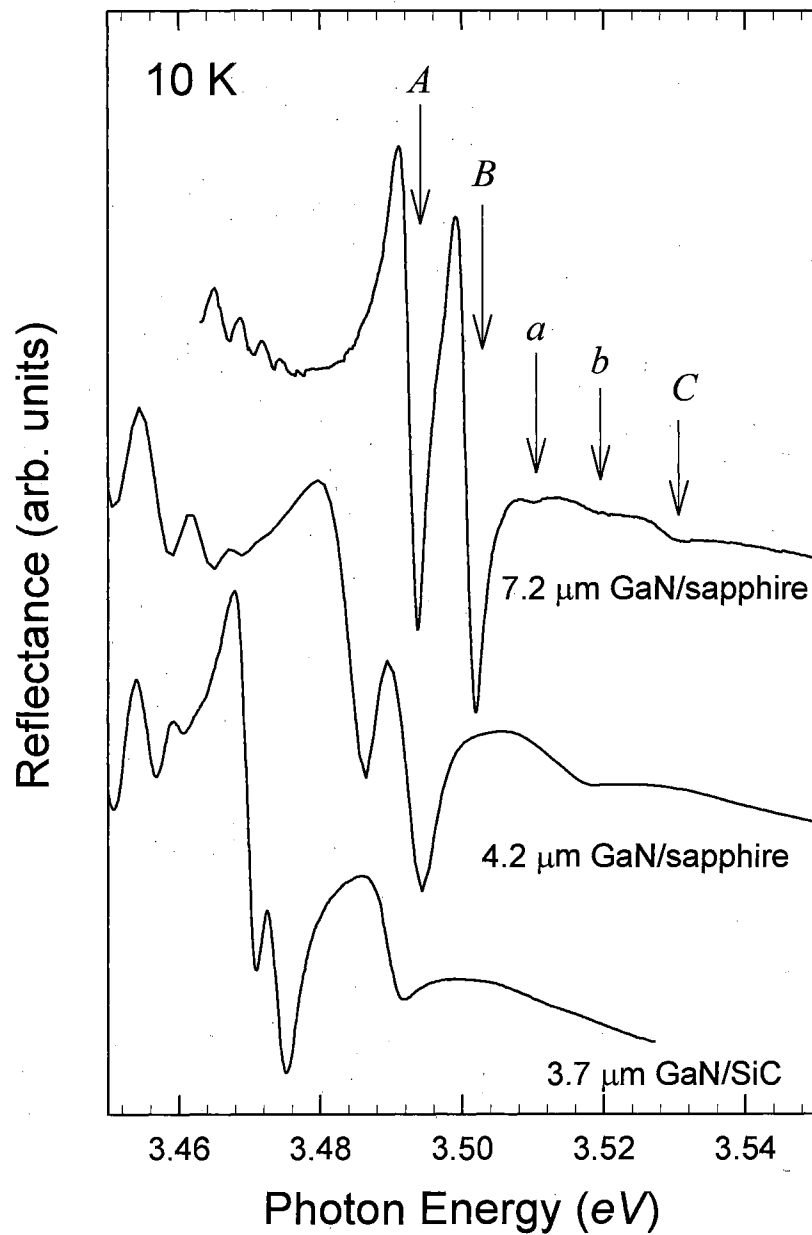


Figure 28. 10 K reflection spectra taken near the bandedge of a 7.2 μm GaN/sapphire sample (top curve), a 4.2 μm GaN/sapphire sample (middle curve), and a 3.7 μm GaN/SiC sample (bottom curve). Various excitonic transitions are labeled for the 7.2 μm epilayer. The curves are displaced vertically for clarity.

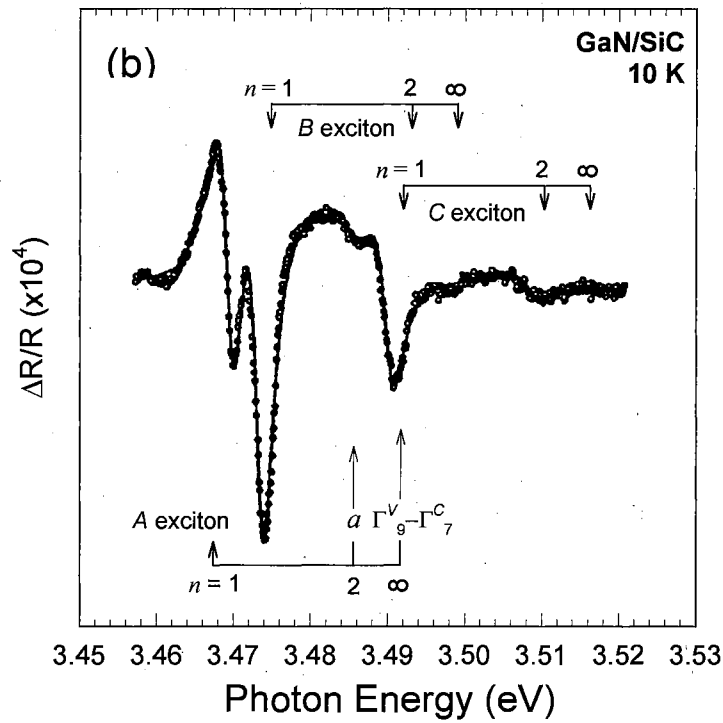
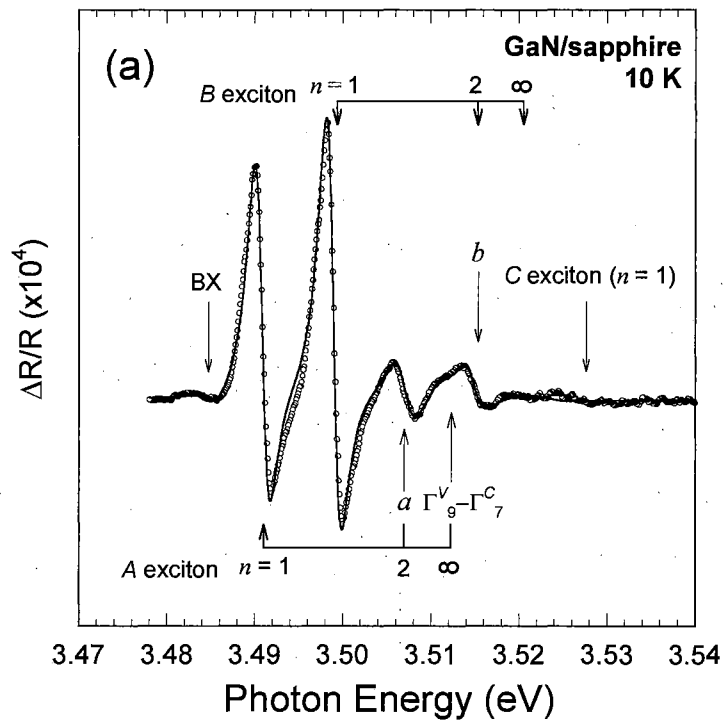


Figure 29. 10 K PR spectra taken from the (a) 7.2 μm GaN/sapphire sample and (b) 3.7 μm GaN/SiC sample. The open circles indicate experimental data, while the solid lines are the best results of the least-square fits to the data.

Excitons and Strain in GaN Epilayers

The residual strain built into GaN epitaxial films has been found to play an important role in determining the energies of excitonic transitions. The effects of residual strain induced by the mismatch of lattice constants and thermal expansion between epilayer and substrate on the intrinsic free exciton transitions in GaN samples were examined by optical measurements in conjunction with high precision XRD measurements. Poisson's ratio, which describes the relationship between strain in the a plane and along the c plane, as well as the uniaxial and hydrostatic deformation potentials were derived from the experimental results. To determine the lattice parameters of the GaN epitaxial films, four-crystal X-ray rocking curves were measured.

As can be seen in Figure 28, the energy positions of the A , B , and C exciton transitions are sample dependent. A number of different transition energies have been reported in the literature. The difference in the reported exciton transition energies can be attributed to the effects of residual strain in the epilayers due to the mismatch of lattice parameters and coefficients of thermal expansion between GaN and the substrate material used. The effects of strain are clearly seen when comparing variations in the lattice parameters of epitaxial films to virtually strain-free bulk GaN, as in Figure 30, where the a lattice constants are plotted versus the c lattice constants of several GaN epilayers grown on SiC and sapphire. As can be seen in the figure, GaN epilayers grown on sapphire substrates are under biaxial compression, whereas those grown on SiC exhibit basal tensile strain. Poisson's ratio, which describes the relationship between the strain in the a plane (ϵ_{\parallel}) and along the c plane (ϵ_{\perp}) induced by the variation of lattice constants in wurtzite semiconductors, can be estimated using the expression:¹¹³

$$\frac{\epsilon_{\perp}}{\epsilon_{\parallel}} = \frac{-2u}{(1-u)}, \quad (4-3)$$

Where $\varepsilon_{\perp} = (c_s - c_o)/c_o$, $\varepsilon_{\parallel} = (a_s - a_o)/a_o$, a_o and c_o are the lattice parameters for bulk strain-free GaN, a_s and c_s are those for the strained GaN epilayer, and ν is Poisson's ratio. The best fits to the experimental data result in a slope of -0.689 for the ratio $\varepsilon_{\perp}/\varepsilon_{\parallel}$, corresponding to a Poisson's ratio of $\nu = 0.256$. Since the strain components ε_{\perp} and ε_{\parallel} are related through the elastic stiffness coefficients for GaN as $\varepsilon_{\perp} = -2C_{13}/C_{33}\varepsilon_{\parallel}$ under biaxial stress conditions, it is interesting to compare the XRD measurement results with the numerical values of C_{13} and C_{33} published in the literature.¹¹⁴ We found that within experimental uncertainty, our results are consistent with the values $C_{13} = 114$ and $C_{33} = 381$ GPa given by Ref. [108] and $C_{13} = 106$ and $C_{33} = 398$ GPa from Ref. [104].

Figure 31 presents the measured free exciton transition energies from the GaN samples used in this work as a function of relative in-plane (biaxial) strain. The excitonic transition energies of strain-free GaN reported in the literature are included in the figure for reference. It is clearly shown in the figure that not only the absolute energy positions for the free excitons shift up or down relative to those of strain-free GaN depending on the substrate, but their separations also change under the influence of strain. This anisotropic effect of strain on the excitonic transition energies allows us to make a direct estimate of the deformation potentials, including both hydrostatic and uniaxial components, for wurtzite GaN. By fitting the experimental data, we find the relationship between the combined hydrostatic deformation potentials D_1 and D_2 , as well as the uniaxial deformation potentials D_3 and D_4 :

$$D_1 - C_{33}/C_{13}D_2 = 37.9 \text{ eV} \quad (4-4)$$

$$D_3 - C_{33}/C_{13}D_4 = -15.2 \text{ eV}, \quad (4-5)$$

where D_1 and D_2 are combined hydrostatic deformation potentials for transitions between the conduction and the valence bands, and D_3 and D_4 are uniaxial deformation potentials characterizing the further splitting of the three topmost valence band edges for tension or compression along and perpendicular to (0001), respectively, and the C_{ij} are the elastic stiffness constants. Based on the facts that the strain-induced total energy shift relative to the excitonic transition energy is very small and the elastic properties of GaN are of a quasicubic nature ($C_{11} \approx C_{33}$), we found that it is appropriate to estimate the numerical

values for the uniaxial and hydrostatic deformation potentials within the range of linear dependence on strain using a quasicubic approximation:¹¹⁵

$$D_3 \approx -2D_4 \text{ and } D_1 - D_2 \approx 2D_4. \quad (4-6)$$

The numerical values for these four principal deformation potentials obtained in this work are $D_1 = -6.5$ eV, $D_2 = -11.8$ eV, $D_3 = -5.3$ eV, and $D_4 = 2.7$ eV. The uncertainty of the above estimates is $\sim 15\%$, originating primarily from experimental error in the precise determination of lattice parameters. A number of investigations using elasticity theory to derive numerical values of the uniaxial and hydrostatic deformation potentials of wurtzite GaN have recently been reported. The results obtained by this work using strain tensor components determined by X-ray measurements are consistent with those derived using this theory.

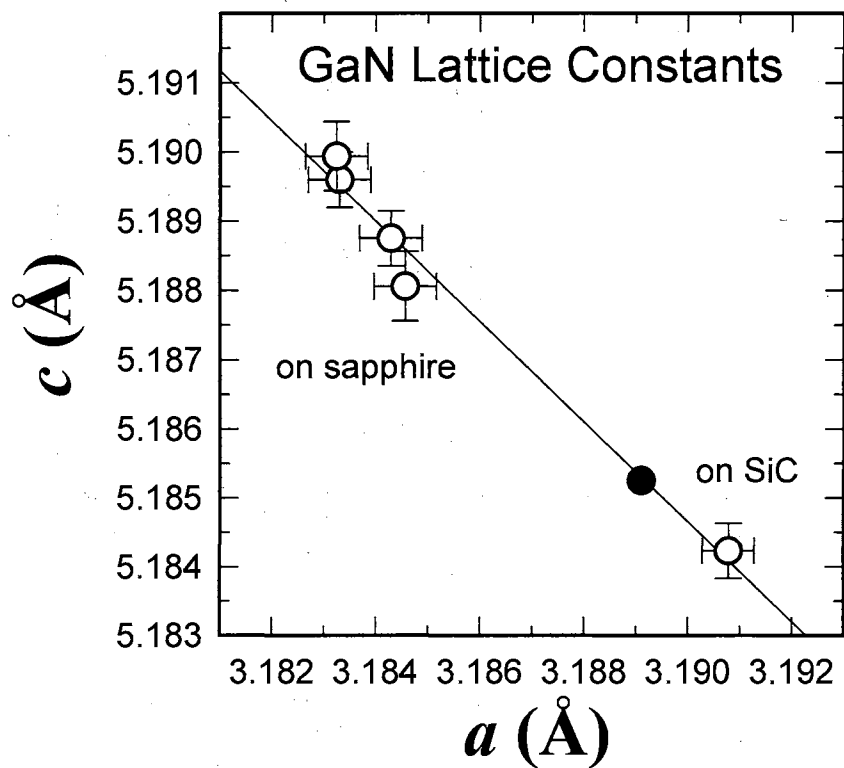


Figure 30. The measured in-plane GaN lattice constant (a) versus the lattice constants in the growth direction (c). The solid circle represents the lattice constants of strain-free GaN. The solid line is the best fit to the data.

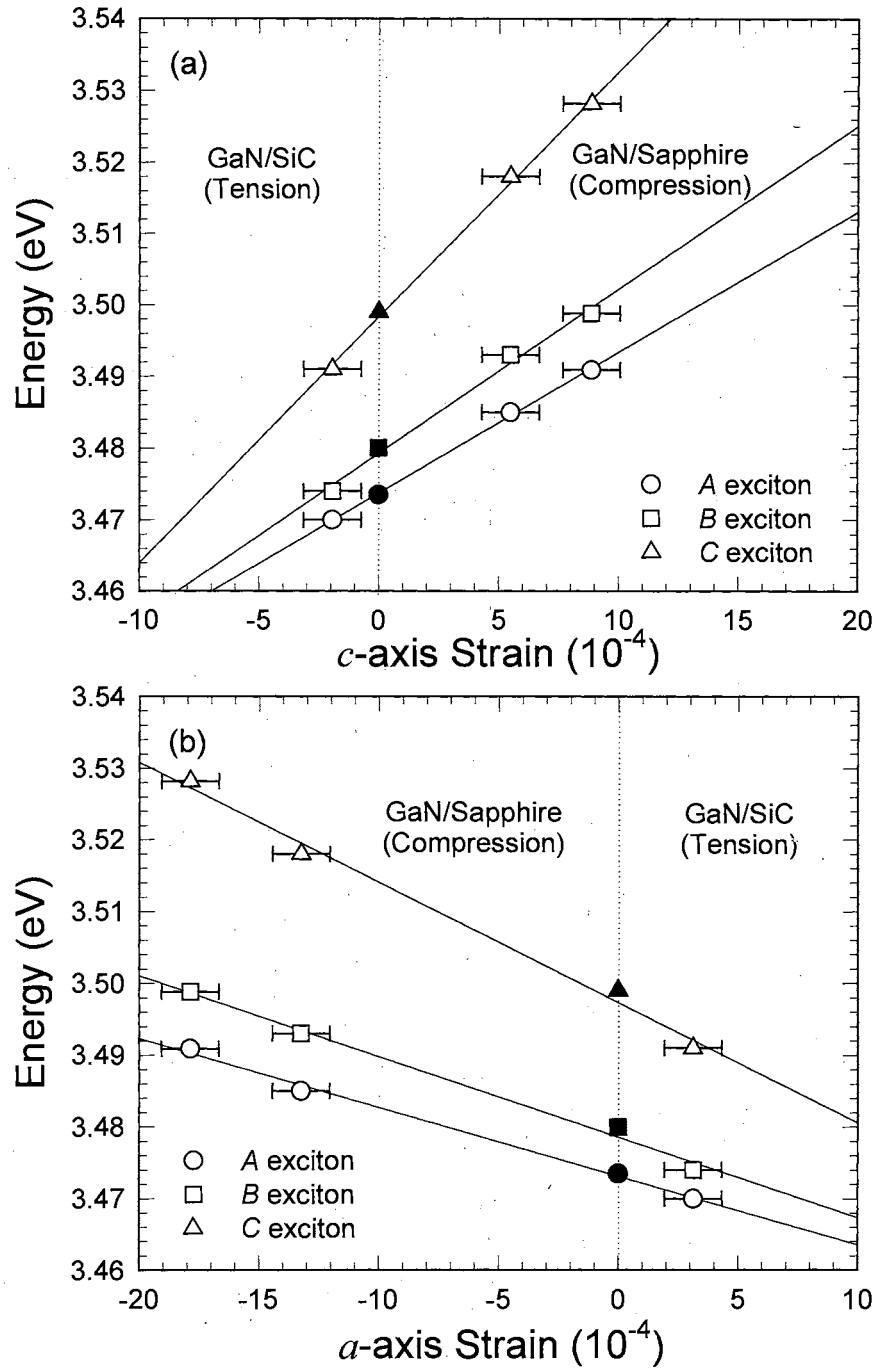


Figure 31. The measured free-exciton transition energies from the GaN samples used in this work as a function of (a) strain in the growth direction and (b) relative in-plane (biaxial) strain. The excitonic transition energies of strain-free GaN are included in the figure for reference. The solid lines are the best linear fits to the experimental data.

Excitonic Photoconductivity in GaN epilayers

PC experiments were performed on 0.4 μm -thick GaN epilayers grown by MOCVD on sapphire substrates. Electrical contact to the sample was achieved by evaporating gold onto the surface of the samples in the MSM finger configuration, as shown in Figure 22 (b). The individual fingers were 41 μm wide, and they were spaced 82 μm apart. The experimental setup used was identical to the one shown in Figure 22 (a). A variety of bias voltages and load resistors were used for the PC experiments. The results presented in this thesis were all taken with $R = 2 \text{ M}\Omega$ and $V = 120 \text{ V}$.

The PC spectrum obtained by scanning the excitation source is shown in Figure 23 for a sample temperature of 10 K. The measured spectrum directly follows the bandedge behavior of the GaN epilayer and is reminiscent of absorption spectra: no signal is seen for lower excitation photon energies, but as we approach the GaN bandgap energy we see a sharp increase in the PC signal due to the creation of electron-hole pairs by the exciting photons. Three sharp peaks are observed in the region of the spectrum near 3.5 eV.

To study the origin of these three peaks, temperature dependent PC was performed. The peaks persisted from 10 K until around 180 K, where they broadened and merged into a single weak feature on a large background. The energy position of these peaks versus temperature did not follow the Varshni equation as expected. To further investigate the origin of the three peaks observed near 3.5 eV, the PC spectrum was compared to PL and reflectance spectra taken from the same sample. This comparison is shown in Figure 32. As depicted in the figure, the peaks did not line up to the *A*, *B*, and *C* exciton energies, as might have been expected. The abnormal temperature dependence and comparison with results of other experiments both support the hypothesis that the peaks observed in PC are not related to excitonic transitions.

However, the valleys in between the peaks in the PC spectrum seem to line up rather well with the A exciton seen in PL and the A and B excitons seen in reflectance. After further analysis of the temperature dependent data, the energy positions of the valleys were found to closely follow the Varshni equation. A similar situation was found in the GaAs material system by Parenteau et al, who studied the PC spectra of GaAs epilayers as a function of epilayer thickness.⁹⁸ They found that as the thickness increased, the signature of the free exciton changed from a peak to a dip in the PC spectrum. This transition occurred at a thickness of about 2 μm in GaAs, where the free exciton has a photon energy of 1.516 eV. Furthermore, they fit the data using Equation 3-15 and obtained excellent agreement between experiment and theory. Additionally, excitonic resonances consisting of both peaks and dips were observed by Gross *et al* in CdS crystals at $T = 77.3$ K.¹¹⁶ They attributed the observation of the peaks and dips in different samples to the presence of two different types of crystals. It is likely that they were seeing different results for different thicknesses of crystal, as explained previously and pictured in Figure 24.

By fitting our observed PC spectra using this method, which is described in Chapter III, we obtained the transition energies for the A and B free excitons in GaN (3.496 and 3.506 eV, respectively). The best least-squares fit to our data is pictured in Figure 33. It would be interesting to do a study of the thickness dependence of the PC spectra for GaN. According to the model used to explain the results presented here, as the thickness of the epilayers is decreased, we would expect to see the excitonic dips in the PC spectra transform into peaks.

This study shows that photoconductivity experiments are a valuable technique in determining the energy positions of excitonic levels in GaN samples. It is especially useful for samples too thick for absorption experiments, or samples in which the top photoconductor layer does not have the lowest bandgap energy, such as for AlGaN epilayers on sapphire with a GaN buffer layer or for III-Nitride samples grown on SiC substrates.

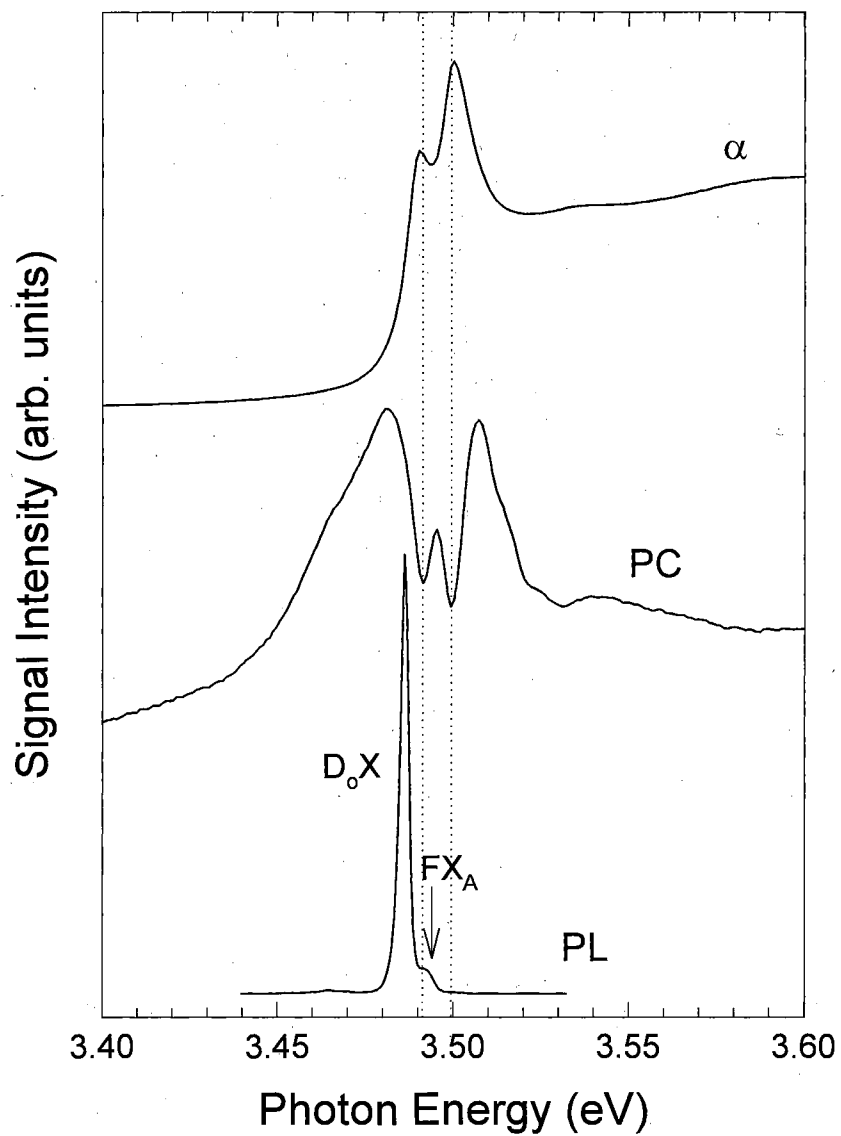


Figure 32. Comparison of 10 K PL and PC data from a 0.4 μm GaN epilayer and 10 K absorption from a 0.38 μm GaN epilayer, both samples grown on sapphire by MOCVD. The three peaks near 3.50 eV in the PC spectra do not match up with any of the observed exciton energies as measured by PL or absorption. The dotted lines show the expected energy positions of the *A* and *B* excitons.

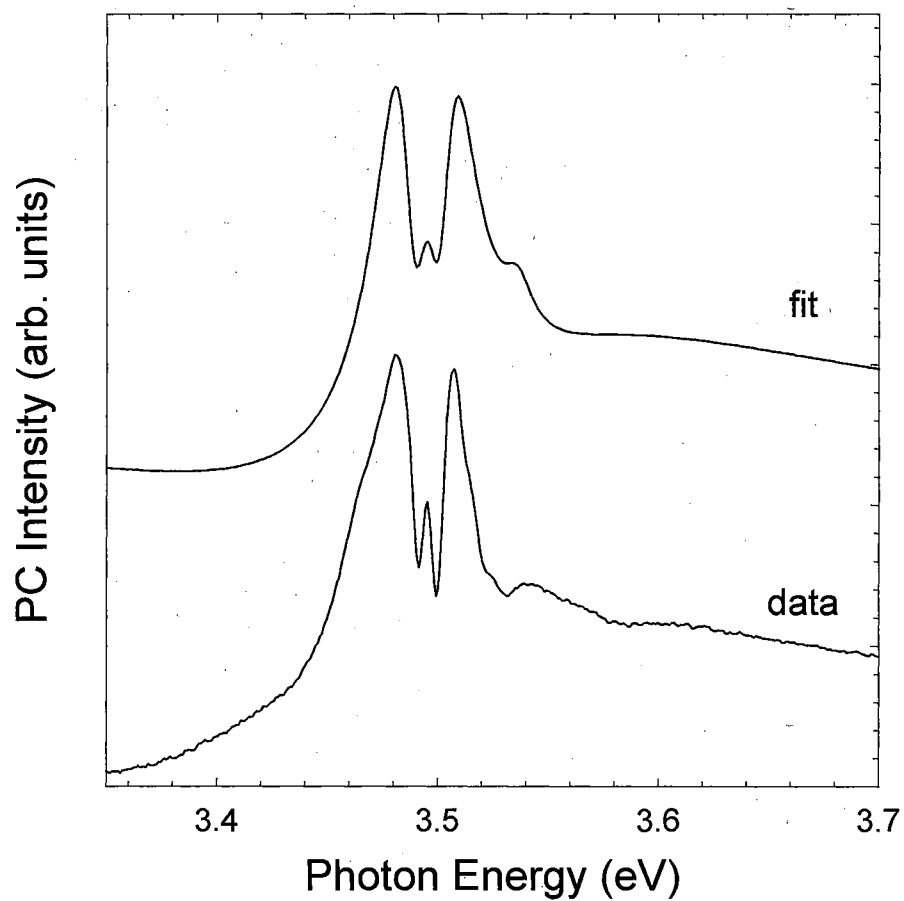


Figure 33. Photoconductivity spectrum of a 0.4 μm GaN epilayer (bottom) and a fit to this data using Equation 3-15 (bottom). The fit yielded *A* and *B* free exciton energies of 3.496 and 3.506 eV, respectively.

CHAPTER V

EXPERIMENTAL INVESTIGATIONS OF III-NITRIDE ALLOYS AND HETEROSTRUCTURES

As discussed in Chapter II, some of the most important optoelectronic devices are grown taking advantage of III-Nitride alloys (such as InGaN and AlGaN) and heterostructures (such as DHs and SCHs). This chapter will describe some of the contributions of the author to the field of experimental research in these areas.

Optical Properties of $\text{In}_x\text{Ga}_{1-x}\text{N}$ Alloys

As discussed in previous chapters, the quest for light emitting devices operating in the blue and UV spectral regions has led to extensive studies in recent years on the properties of wide bandgap semiconductor materials. The III-Nitrides have attracted much attention as the most promising material for such device applications.^{117,118,119} Within this family of semiconducting materials, the InGaN alloy system is particularly important because its direct band gap covers a wide spectral range from UV (~ 365 nm for GaN) to red (~ 650 nm for InN). The recently commercialized superbright high efficiency blue, green, and white LEDs and current injection violet LDs are all based on InGaN/GaN heterostructures using InGaN layers as the active light emitting medium.^{16,120} In this section, we present the results of a study of the optical properties of InGaN alloys ($0 < x < 0.2$) grown on top of thick GaN epilayers by MOCVD. PL measurements were performed to assess the optical properties of samples with different

alloy compositions. Photomodulation spectroscopy was used to determine the energy gap of the samples and to examine the effect of temperature on the bandgap. Transient luminescence measurements were carried out to study the PL decay processes in these alloy samples.

The InGaN alloy samples used in this study were nominally undoped single crystal epilayers grown by MOCVD. Before the deposition of the InGaN epilayers, thick GaN layers were grown on sapphire substrates at a temperature of 1050 °C with 20 nm GaN buffer layers. The alloy layers were deposited at a temperature around 800 °C. The thickness of the InGaN epitaxial layers was typically around a few thousand ångstroms. Optical measurements were carried out on the InGaN samples over a wide temperature range from 10 K to RT. The samples were mounted onto the cold finger of a closed cycle helium refrigerator and cooled to the desired temperature. PL spectra were measured using the setup shown in Figure 11 (a) with a photon counting PMT system for detection. PR spectra were measured using the setup shown in Figure 15 (c). Transient luminescence measurements were performed using the experimental setup shown in Figure 14. The streak camera was in synchroscan mode and had a temporal resolution of ~ 2 ps. The overall time resolution of the system was less than 15 ps.

10 K PL and PR spectra of an $\text{In}_{0.14}\text{Ga}_{0.86}\text{N}$ sample are shown in Figure 34. The PL spectrum (lower curve) exhibits two dominant spectral features: a sharp, strong emission line at higher energy arising from the near-bandedge excitonic transitions in GaN, and a strong, relatively broad luminescence structure at ~ 3.08 eV related to the InGaN alloy. The weak structures observed between these two features are mainly luminescence signatures involving DAP transitions in the GaN layer. On the lower energy side of the PR spectrum (upper curve), the spectral feature with the derivativelike lineshape corresponds to the optical transition associated with the alloy band gap, and the differential spectral structures at high energy are free exciton transitions from the edges of different valence bands to the conduction band of GaN. PR is a spectroscopic method utilizing a modulation of the built-in electric field already present in the samples. We found that using a third derivative Gaussian lineshape functional form, which is appropriate for describing band-to-band transitions,^{93,121} results in a much better fit to the positions and widths of the PR spectra than using a Lorentzian functional form,^{122,123}

which is used to describe excitonic transitions. This suggests that the optical transitions observed at even the lowest temperature are of a band-to-band nature rather than excitonic, presumably because of the strong inhomogeneous broadening due to alloying effects. The best fits to the 10 K PR spectral features using Equation 3-14 yield an energy of 3.143 eV for the transition in $\text{In}_{0.14}\text{Ga}_{0.86}\text{N}$, indicating a large Stokes shift (~ 60 meV) between the PL peak position and the actual band-to-band transition energy.

With increasing temperature, the PL signal from the alloy layer quickly decreases in intensity due to enhanced nonradiative recombination processes and thermal broadening of the emission structures, whereas the PR spectral structures associated with the InGaN bandedge could be well resolved up to room temperature for all alloy samples used. Figure 35 shows the shift of optical transition energy as a function of temperature for the $\text{In}_{0.14}\text{Ga}_{0.86}\text{N}$ sample. The solid line in the figure represents the best fit to the Varshni empirical equation. The parameters obtained from the best fit for the sample are given in the figure. The superior spectral resolution of PR spectroscopy compared to PL measurements enables us to determine the actual energy gaps for the InGaN alloy samples used in this work. In Figure 36 we plot the measured energy gaps of various samples at 10 K and RT against their alloy compositions, with 10 K PL results plotted for comparison. Within the alloy composition range studied in this work, the PR results are in reasonably good agreement with the following theoretical prediction for the dependence of the InGaN band gap on In concentration including the bowing effect:¹²⁴

$$E(x) = 3.5 - 2.63x + 1.02x^2 \text{ eV.} \quad (5-1)$$

The scattered PL data, as seen in the figure, are not a reliable way to map the energy gap evolution for the alloy system because the PL signals are most likely associated with impurities and suffer from the effects of alloy disorder broadening. On the other hand, our values measured using PR spectroscopy agree within $\sim 1\%$ with a previous determination of the alloy concentrations by X-ray measurements (not shown).

We have also performed TRPL measurements to study carrier recombination dynamics in the InGaN samples. Figure 37 shows the temporal evolution of spectrally integrated luminescence associated with an $\text{In}_{0.08}\text{Ga}_{0.92}\text{N}$ sample at selected temperatures. The time evolution of the luminescence is dominated by an exponential decay with a

measured effective lifetime around 340 ps at 10 K. As the sample temperature is increased, the temporal profile of the luminescence gradually evolves into an increasingly nonexponential decay concurrent with a drastic decrease of the effective lifetime for the main decay process. At temperatures around 150 K, the deduced lifetime for the PL decay is already below the limit of our instrumental resolution. Similar results were obtained for all the samples used in this work: the measured decay times for near-bandedge PL emissions were generally around a few hundred picoseconds at 10 K, and decreased rapidly as the sample temperatures increased. The measured decay time was examined as a function of energy position for the 10 K PL peak from an $\text{In}_{0.08}\text{Ga}_{0.92}\text{N}$ shown in the inset of Figure 37. This allows us to verify whether the PL structure results from the recombination of localized excitons or whether it directly involves impurity states and alloy potential fluctuations.^{125,126} If the PL emission originates from localized excitons in the InGaN alloys, the lifetime is predicted to obey the following power-law dependence:¹²⁷ $\tau \propto E_{BX}^{3/2}$, where E_{BX} is the exciton localization energy. This means that the measured lifetime should increase with increasing exciton localization energy, corresponding to a decrease in electron-hole wave function overlap. Our experimental results did not exhibit such a dependence of measured effective lifetime upon the energy position, suggesting that impurity states and alloy potential fluctuations are most likely responsible for the observed PL signals.

Although the radiative recombination processes involved in the PL emission of the InGaN samples are not of an excitonic nature, as mentioned previously, it is still worthy to make a comparison of the results obtained in this work with the excitonic emission decay processes observed in pure GaN.¹²⁸ While the measured effective lifetime for PL decay in InGaN samples was found to be an order of magnitude longer than that in GaN, the dependence of the PL decay process on the temperature in InGaN alloys is much stronger than that in GaN.¹²⁹ Such a strong influence of temperature suggests that although recombination from carriers bound to extrinsic states such as defects or impurities can be very efficient at low temperatures, the measured decay time is still determined by the detailed decay kinetics in the alloy samples. The observed decrease of the PL decay time along with the increasingly nonexponential transient characteristics with temperature indicates that incrementally stronger nonradiative

relaxations occur as the temperature increases, resulting in the continued faster decay of the photogenerated carrier population. The decrease of PL in both intensity and observed effective lifetime with temperature suggests that nonradiative processes including trapping and recombination at energy levels associated with impurities and defect centers at or near the midgap (Shockley-Read-Hall recombination), surface recombination, and Auger recombination prevail in the InGaN alloys at relatively high temperatures. It is well known that the lifetime of photogenerated carriers in semiconductor alloy systems is strongly dependent on the sample quality.¹²⁶ The observations reported here indicate that the impurities and defects incorporated during InGaN epitaxial growth generate PL quenching centers in the layers which adversely affect the radiative recombination of carriers.

In conclusion, we have studied optical transition processes in InGaN alloys using several different experimental approaches including conventional and time-resolved PL measurements and PR spectroscopy. PR allowed us to unambiguously determine the bandgap energy for the alloy samples within the alloy composition range studied ($0 < x < 0.2$). We found that the low temperature PL emission from the alloy layers is primarily due to recombination directly involving impurity states and alloy potential fluctuations. The strong dependence of the PL decay time on temperature observed in the alloy samples indicates that the trapping and recombination of photogenerated carriers at impurities and defect centers are dominant channels in determining the carrier population decay process.

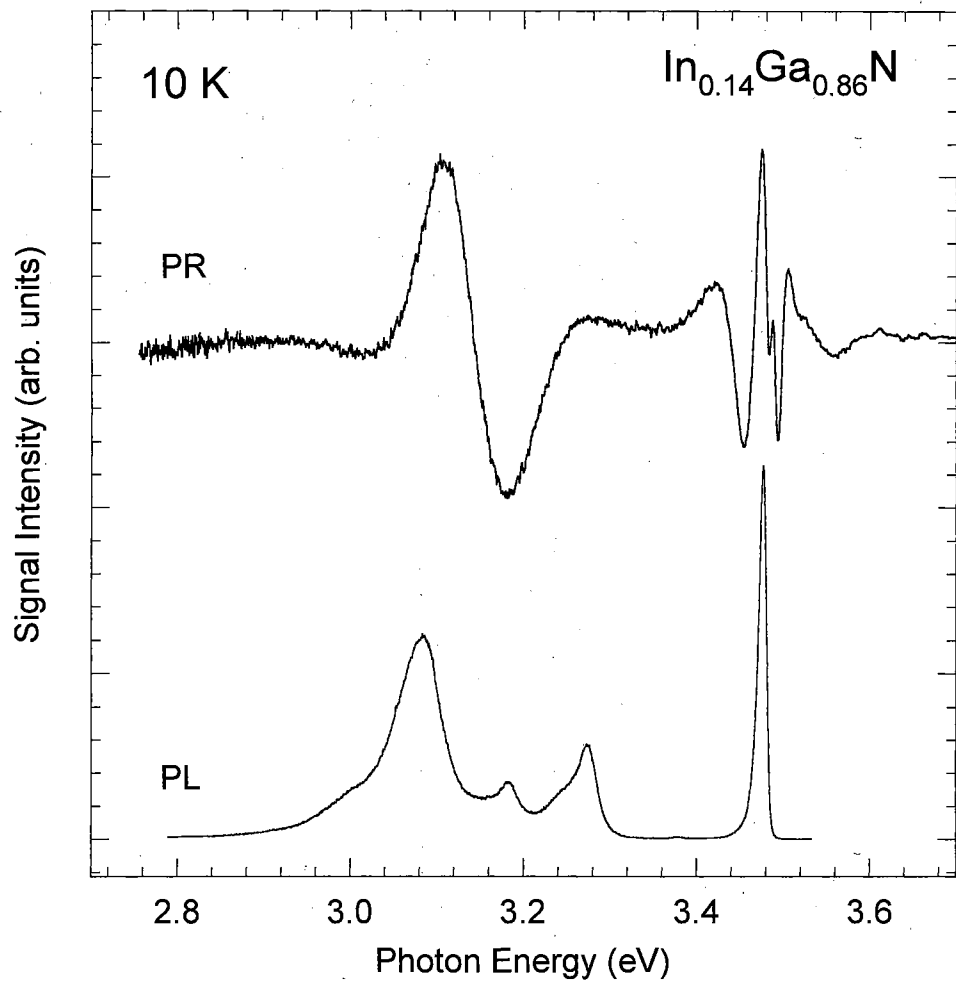


Figure 34. PR (upper curve) and PL (lower curve) spectra of an $\text{In}_{0.14}\text{Ga}_{0.86}\text{N}$ sample at 10 K.

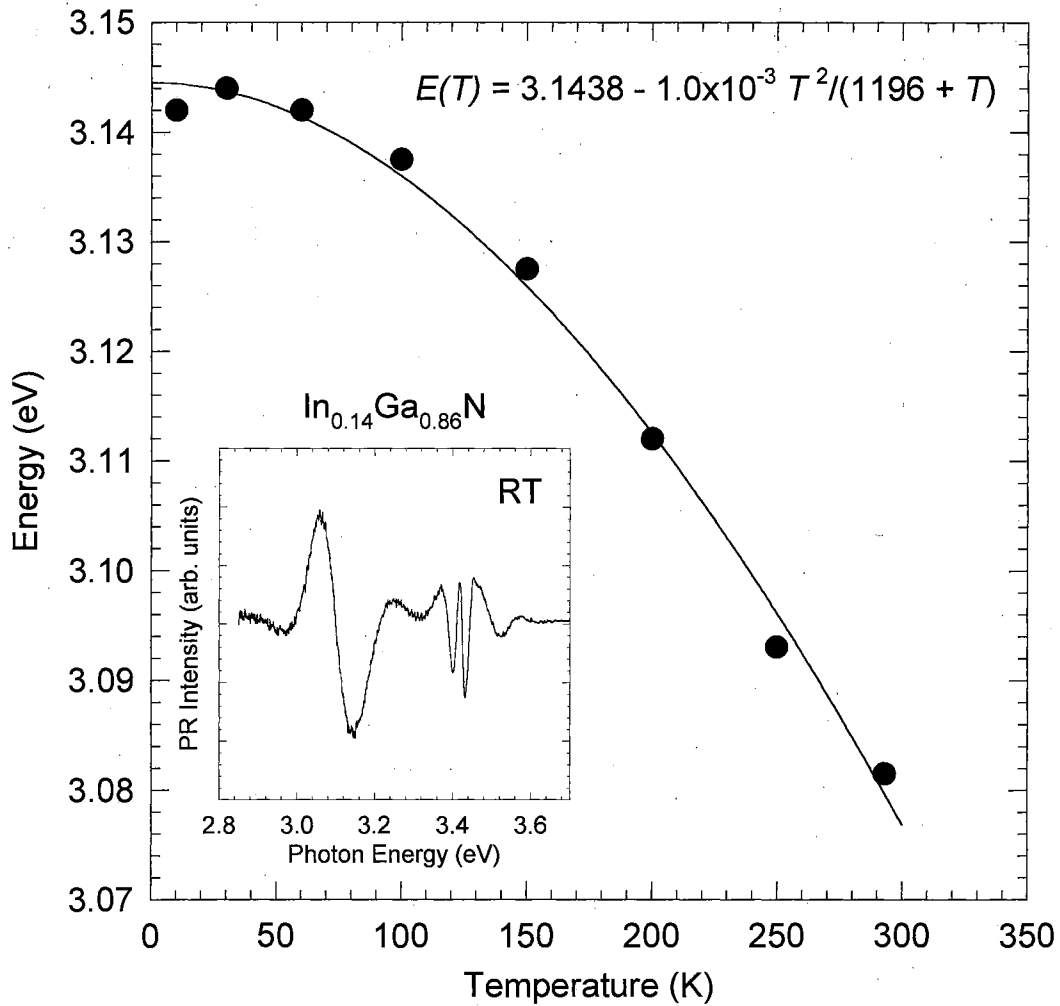


Figure 35. Temperature dependence of the interband transition energy of the $\text{In}_{0.14}\text{Ga}_{0.86}\text{N}$ sample. The solid curve represents the best least-squares fit to the experimental data using the Varshni empirical equation. The inset shows a PR curve of the sample at RT.

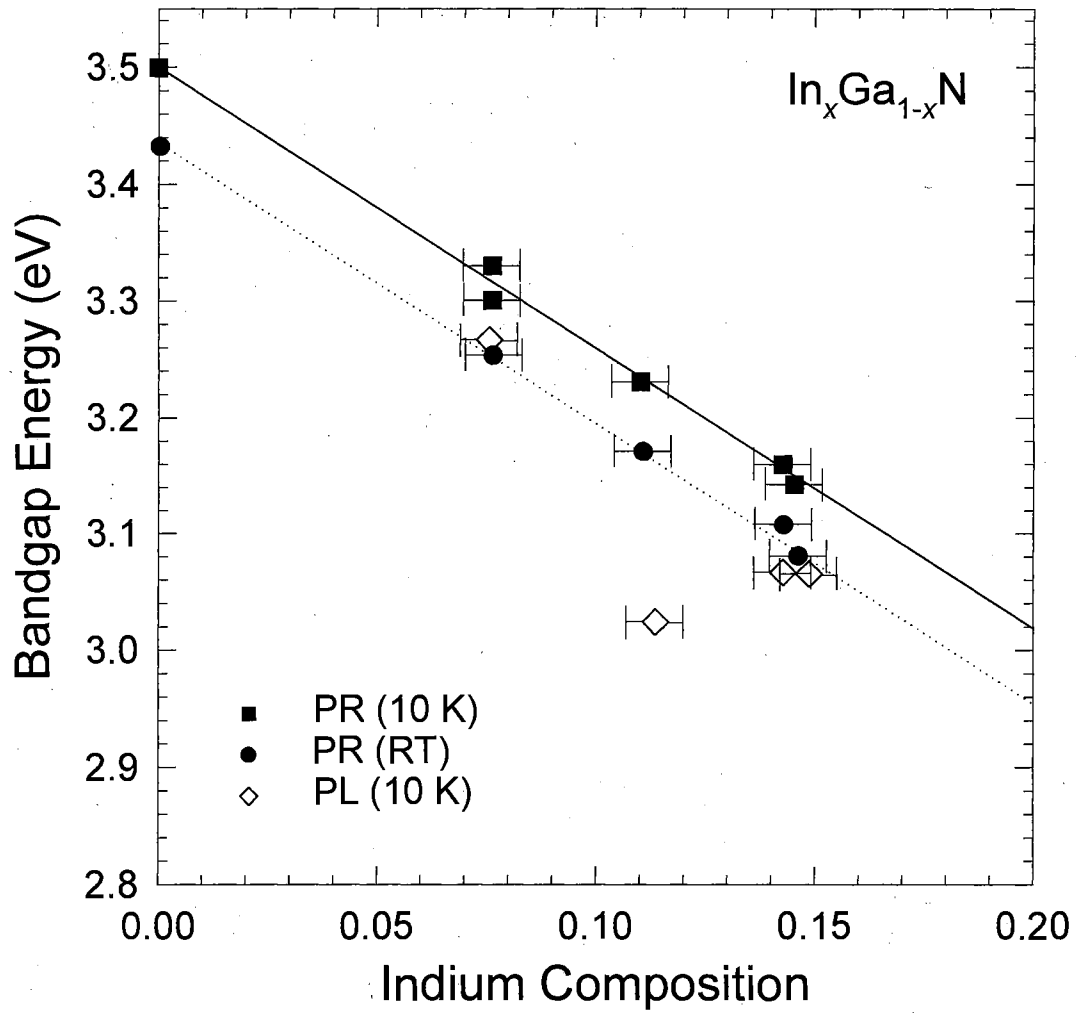


Figure 36. Bandgaps of various samples measured by PR at 10 K and RT vs. their alloy concentrations. 10 K PL results are shown for comparison. The solid and dotted line are the theoretically predicted dependence of the $\text{In}_x\text{Ga}_{1-x}\text{N}$ bandgap on In concentration at 10 K and RT, respectively.

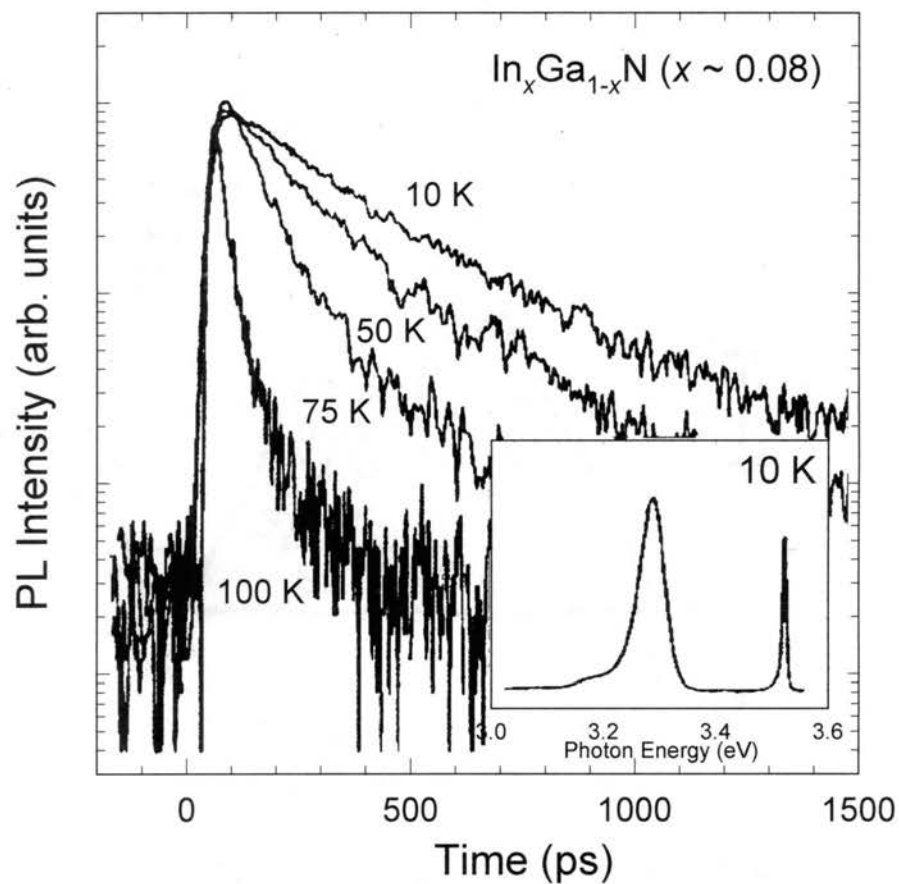


Figure 37. Temporal variation of the alloy PL peak for an $\text{In}_{0.08}\text{Ga}_{0.92}\text{N}$ sample at selected temperatures. The inset shows the 10 K PL spectrum over a broad spectral range.

High Pressure Studies of the III-Nitrides

Experimental investigations of the pressure dependence of bandedge-related optical transitions in AlGaN and InGaN alloys, which can provide important insight into the nature of the radiative decay processes of photoexcited carriers in these alloy systems, have not been thoroughly explored. Since AlGaN and InGaN alloys with small Al and In concentrations are commonly used in InGaN/GaN/AlGaN LEDs and LDs and also in GaN/AlGaN HFETs, all of which are strained systems, it becomes extremely useful to have a working knowledge of the pressure dependence of the bandgaps of AlGaN and InGaN layers. This knowledge can be used to calculate the band alignment, a necessary step in the engineering of devices with different Al and In mole fractions. In this report, we present the results of pressure dependent PL studies on AlGaN and InGaN epilayers using the diamond anvil cell (DAC) technique (introduced in Chapter III). The PL spectra of the AlGaN and InGaN samples used in this work were dominated by strong near-bandedge emission structures. Under applied pressure, these emission structures were found to linearly shift to higher energies. From the magnitude of the energy shifts, we were able to determine the pressure coefficients for the samples. Our results provide a direct measure of the pressure dependence of the direct bandgap at the Γ point of the samples. We also found that the pressure coefficients for AlGaN and InGaN alloys are slightly dependent on alloy composition.

The AlGaN and InGaN samples used in this work were nominally undoped single-crystal heteroepitaxial films grown by MOCVD on (0001) plane sapphire substrates. The AlN mole fractions for the AlGaN alloys were $5 \pm 1\%$ and $35 \pm 2\%$, respectively, estimated by XRD and optical transmission measurements. The InGaN samples were grown at a temperature of $800\text{ }^\circ\text{C}$ on top of $2\text{ }\mu\text{m}$ -thick GaN layers. Two InGaN alloy samples were measured, which had InN mole fractions of 8% and 14%. PL

measurements were performed using the experimental setup shown in Figure 11 (a). A frequency-doubled Ar⁺ laser (244 nm) was used as the excitation source for the AlGa_N samples. A photon-counting PMT system was used for detection. Pressure dependent PL measurements were carried out with gasketed DACs using the technique described in Chapter III.

Figure 38 shows the PL spectrum taken at 10 K from the Al_{0.35}Ga_{0.65}N layer at atmospheric pressure. The spectrum consists of a strong and sharp luminescence emission at 4.327 eV and a broad emission band centered around 2.39 eV. The emission line at higher energy is near-bandedge luminescence caused primarily by the radiative decay of photoexcited carriers localized in the band tail states induced by local alloy concentration fluctuations.^{130,131} The relatively large FWHM value of 65 meV for this emission line reflects the effect of the fluctuations induced by alloy disorder. The weak and broad emission band observed at ~ 2.39 eV is reminiscent of the yellow emission band commonly observed in GaN at ~ 2.2 eV, but is shifted towards the green spectral region in Al_{0.35}Ga_{0.65}N.

Under applied pressure, the near-bandedge emission line shifts towards higher energy, indicating an increase of the direct band gap of the alloy. The effect of applied pressure on the Al_{0.35}Ga_{0.65}N sample can be seen in Figure 39, where the near-bandedge luminescence feature measured from the sample at selected pressures is displayed. The inset of Figure 39 shows the energy positions of the emission peak as a function of applied pressure. The solid line is the best least-squares fit to the linear pressure dependent function given in Equation 3-2, and yields a pressure coefficient of $\alpha = 3.6 \times 10^{-3}$ eV/kbar. Similar results were obtained from the Al_{0.05}Ga_{0.95}N sample, and are plotted in Figure 40. The inset shows the RT PL spectrum of the emission related to the bandedge of the alloy taken at atmospheric pressure. A pressure coefficient of $\alpha = 4.0 \times 10^{-3}$ eV/kbar was determined for the Al_{0.05}Ga_{0.95}N sample. These values are comparable to the pressure coefficients observed for excitonic transitions associated with the fundamental bandgap of GaN^{132,133,134} and the near-bandedge luminescence in InGa_N alloys.¹³⁵ The shift of the near-bandedge luminescence peak positions with pressure in the AlGa_N epilayers is a signature of the direct dependence of bandgap on applied pressure. This is true because the conduction band minimum and the valence band

maximum of the alloys vary with the local value of x and act as a potential energy for the envelope function of the carriers in the effective mass approximation. The electronic states involved in the recombination processes responsible for the near-bandedge PL emissions can, therefore, be described within the framework of the effective mass approximation. Therefore, the shift of the emission structures associated with the radiative decay of carriers under hydrostatic pressure follows the direct bandgap of the AlGaN epilayers.

So far, no experimental results have been reported regarding the pressure coefficient of pure AlN, which would allow a prediction of the dependence of the direct bandgap energy on pressure as a function of alloy composition for the AlGaN alloy system. A theoretical calculation by Christensen and Gorczyca arrived at a pressure coefficient of 4.0×10^{-3} eV/kbar for the band gap of AlN,¹³⁶ suggesting that there is no significant difference between the values of pressure coefficient for the bandgaps of AlN and GaN (where $\alpha = 3.9 \times 10^{-3}$ eV/kbar) despite the large difference (~ 2.7 eV) in bandgap energies for these materials.

The energy shift of the broad emission band in the green spectral region (not shown) was found to be much smaller than that of the near-bandedge emission line from the AlGaN alloy. Recent theoretical calculations and experimental observations suggest that a defect-related donor state is involved in the recombination process that gives rise to the yellow emission band in GaN.^{137,138,139,140} This defect-related donor is predicted to introduce a resonance approximately 0.4-0.8 eV above the bottom of the conduction band of GaN, and is expected to become a donor-like deep center once it is pushed sufficiently deep into the forbidden gap by the external application of pressure. Perlin *et al* have succeeded in demonstrating such a resonant-to-deep transition by monitoring the energy shift of the yellow emission band as a function of the applied pressure in GaN samples.^{139,140} Their results showed that the yellow emission band followed the GaN bandgap up to 180 kbar, then lost its linear pressure dependence and became insensitive to applied pressure. Alloying AlN with GaN has an effect analogous to the application of hydrostatic pressure. It shifts the resonant electronic level into the forbidden gap as the bandgap increases. After the alloying-induced resonant-to-deep transition, which is expected to occur in the range of 20-25% AlN alloy fraction, the energy position of the

donor state becomes insensitive to a further change of the bandgap. The peak position of the broad emission band no longer shifts at a rate similar to the bandgap change with the alloy composition. It would be very interesting to study the effect of pressure on the broad emission band in AlGaN samples with relatively high Al concentrations. Unfortunately, the pressure dependence of the broad emission band in the $\text{Al}_{0.35}\text{Ga}_{0.65}\text{N}$ sample could not be reliably derived due to the overlap of the emission band with the strong fluorescence of the diamonds in the DAC under excitation of the 244 nm Ar^+ laser line.

For the InGaN case, Figure 41 presents the 10 K PL spectra of the $\text{In}_{0.08}\text{Ga}_{0.92}\text{N}$ and $\text{In}_{0.14}\text{Ga}_{0.86}\text{N}$ alloy samples at atmospheric pressure. The same experimental technique and fitting procedure used on the AlGaN samples above were applied to the study of the InGaN layers. Both PL spectra exhibit two dominant spectral features: a sharp emission line at higher energy arising from near-bandedge excitonic transitions in the GaN layers underneath the InGaN, and a strong, relatively broad luminescence peak associated with the alloys. The excitonic transitions in GaN originate from the radiative recombination of bound excitons. The emission structures observed from the alloy layers are due to the radiative decay of photoexcited charge carriers localized in the band tail states created by alloy potential fluctuations, similar to what is observed in the AlGaN case. The weaker spectral features observed between the two main emission lines, as well as the features on the low energy side of the alloy emission peak, are related to DAP transitions and their phonon replicas in the GaN layers.

Figure 42 shows the effect of applied pressure on the transitions in the InGaN alloys at 10 K. In the figure, the peak emission energy is plotted as a function of pressure for the two samples studied as well as for the underlying GaN layers. The solid lines represent the best least-squares fits of the data to the standard linear pressure dependence, which yield values of $\alpha = 3.9 \times 10^{-3}$ eV/kbar for $\text{In}_{0.08}\text{Ga}_{0.92}\text{N}$, $\alpha = 3.5 \times 10^{-3}$ eV/kbar for $\text{In}_{0.14}\text{Ga}_{0.86}\text{N}$, and $\alpha = 3.9 \times 10^{-3}$ for GaN. The small difference in pressure coefficients observed here is a real effect, and is likely direct evidence of a composition dependence of the pressure coefficients for InGaN alloys. A theoretical calculation by Christensen and Gorczyca predicted a pressure coefficient of 3.3×10^{-3} eV/kbar for the bandgap of InN.¹³⁶ This result agrees with the small decrease in the pressure coefficient with

increasing In concentration observed here.

In summary, we have studied the effects of hydrostatic pressure on the PL in AlGaN and InGaN alloys using the DAC technique. The PL spectra of the AlGaN and InGaN samples used in this work exhibit strong near-bandedge emission structures, which allows the direct determination of the pressure coefficients for AlGaN and InGaN alloy samples. For the AlGaN alloys, we obtain values of $\alpha = 4.0 \times 10^{-3}$ eV/kbar for $\text{Al}_{0.05}\text{Ga}_{0.95}\text{N}$ and $\alpha = 3.6 \times 10^{-3}$ eV/kbar for $\text{Al}_{0.35}\text{Ga}_{0.65}\text{N}$. For the InGaN alloys, we obtain values of $\alpha = 3.9 \times 10^{-3}$ eV/kbar for $\text{In}_{0.08}\text{Ga}_{0.92}\text{N}$ and $\alpha = 3.5 \times 10^{-3}$ eV/kbar for $\text{In}_{0.14}\text{Ga}_{0.86}\text{N}$. Our results suggest that the near-bandedge emission observed in all of the alloy samples studied originates from the radiative decay of carriers localized in the band tail states of alloy potential fluctuations within the framework of the effective mass approximation. Therefore, the pressure coefficients obtained for the near-bandedge emissions provide a direct measure of the pressure dependence of the direct band gap at the Γ point for $\text{Al}_{0.05}\text{Ga}_{0.95}\text{N}$ and $\text{Al}_{0.35}\text{Ga}_{0.65}\text{N}$ as well as $\text{In}_{0.08}\text{Ga}_{0.92}\text{N}$ and $\text{In}_{0.14}\text{Ga}_{0.86}\text{N}$.

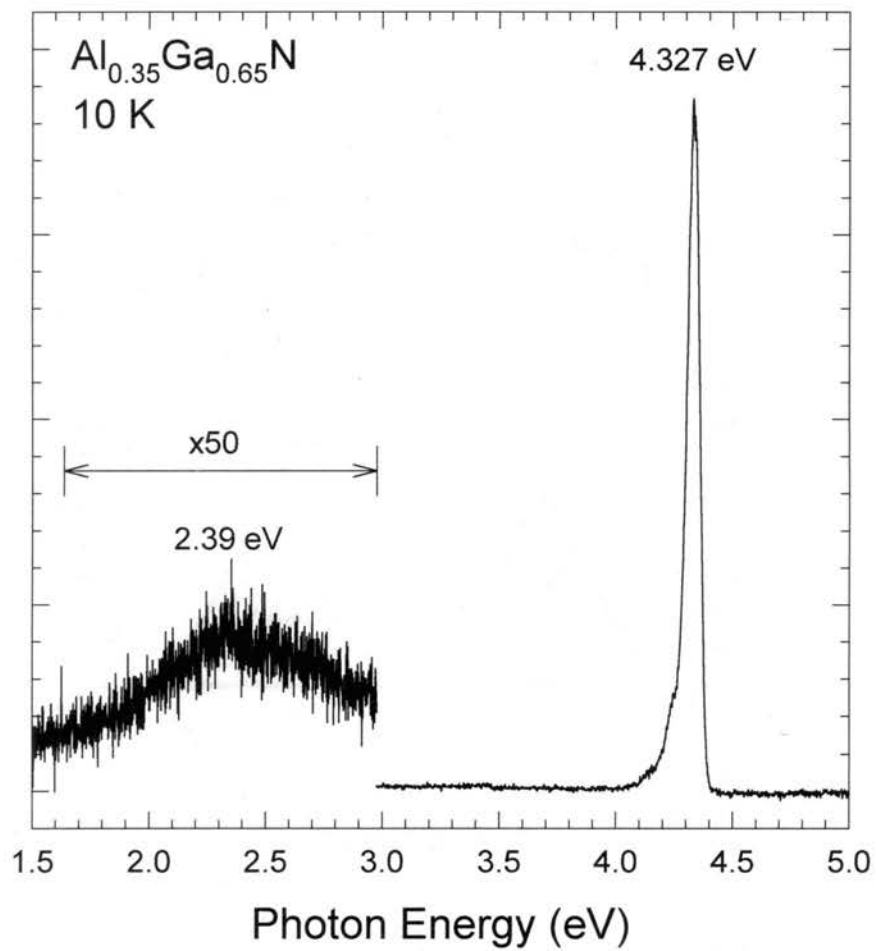


Figure 38. 10 K PL spectrum taken from an $\text{Al}_{0.35}\text{Ga}_{0.65}\text{N}$ epitaxial layer at atmospheric pressure.

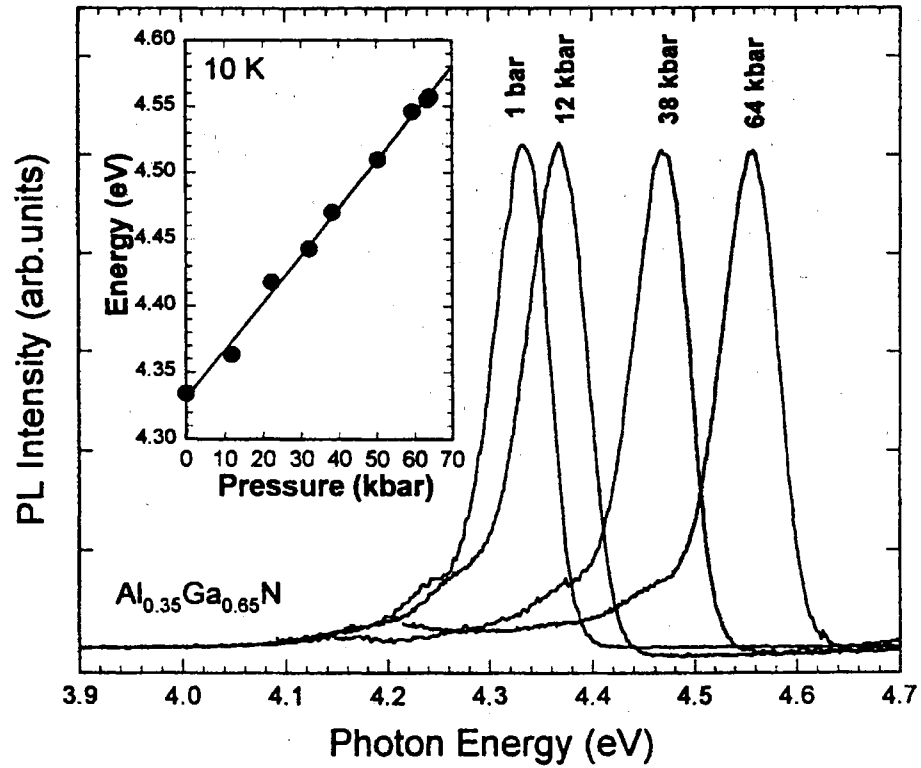


Figure 39. Near-bandedge luminescence of the $\text{Al}_{0.35}\text{Ga}_{0.65}\text{N}$ sample at selected pressures. The inset shows the energy position of the emission peak versus applied pressures. The solid line in the inset is the best fit to the experimental data.

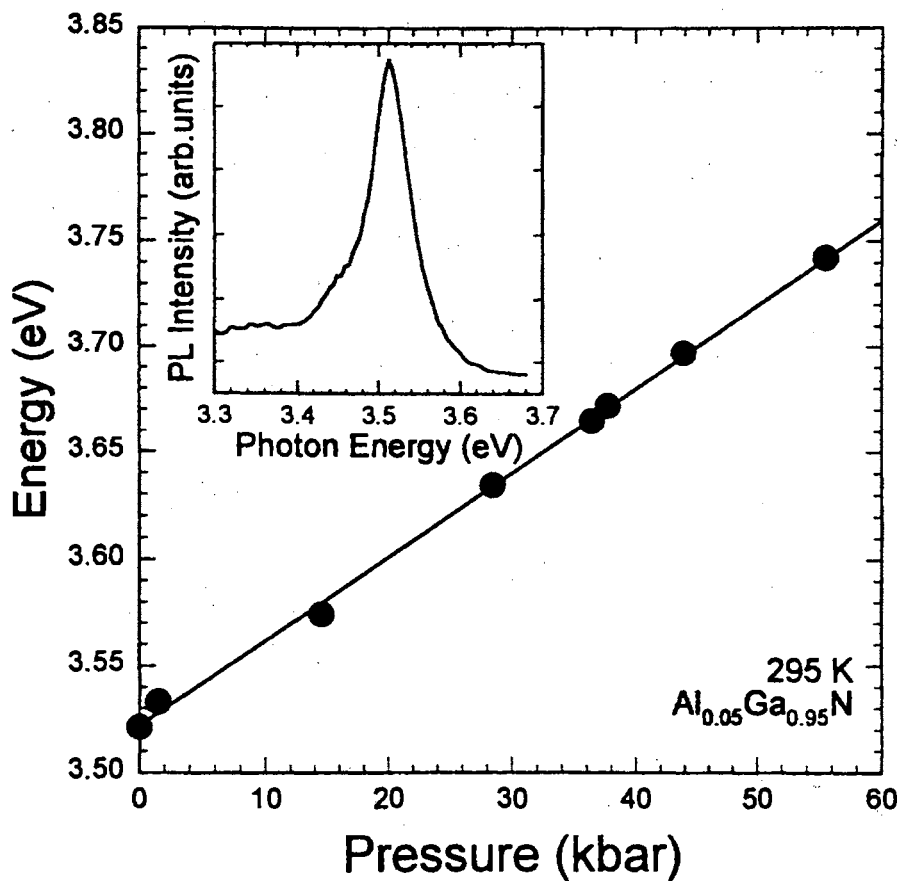


Figure 40. Peak position of the PL emission from an $\text{Al}_{0.05}\text{Ga}_{0.95}\text{N}$ sample as a function of applied pressure at RT. The inset shows the RT PL spectrum of the sample at atmospheric pressure.

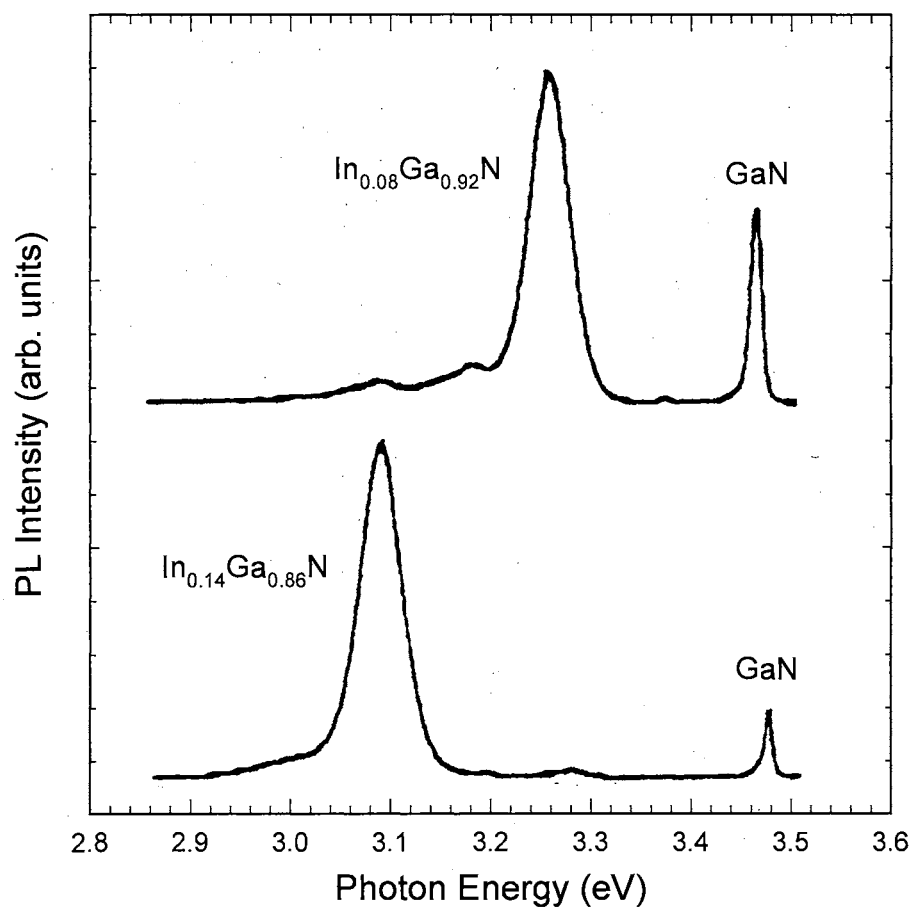


Figure 41. 10 K PL spectra of the InGaN alloy samples at atmospheric pressure.

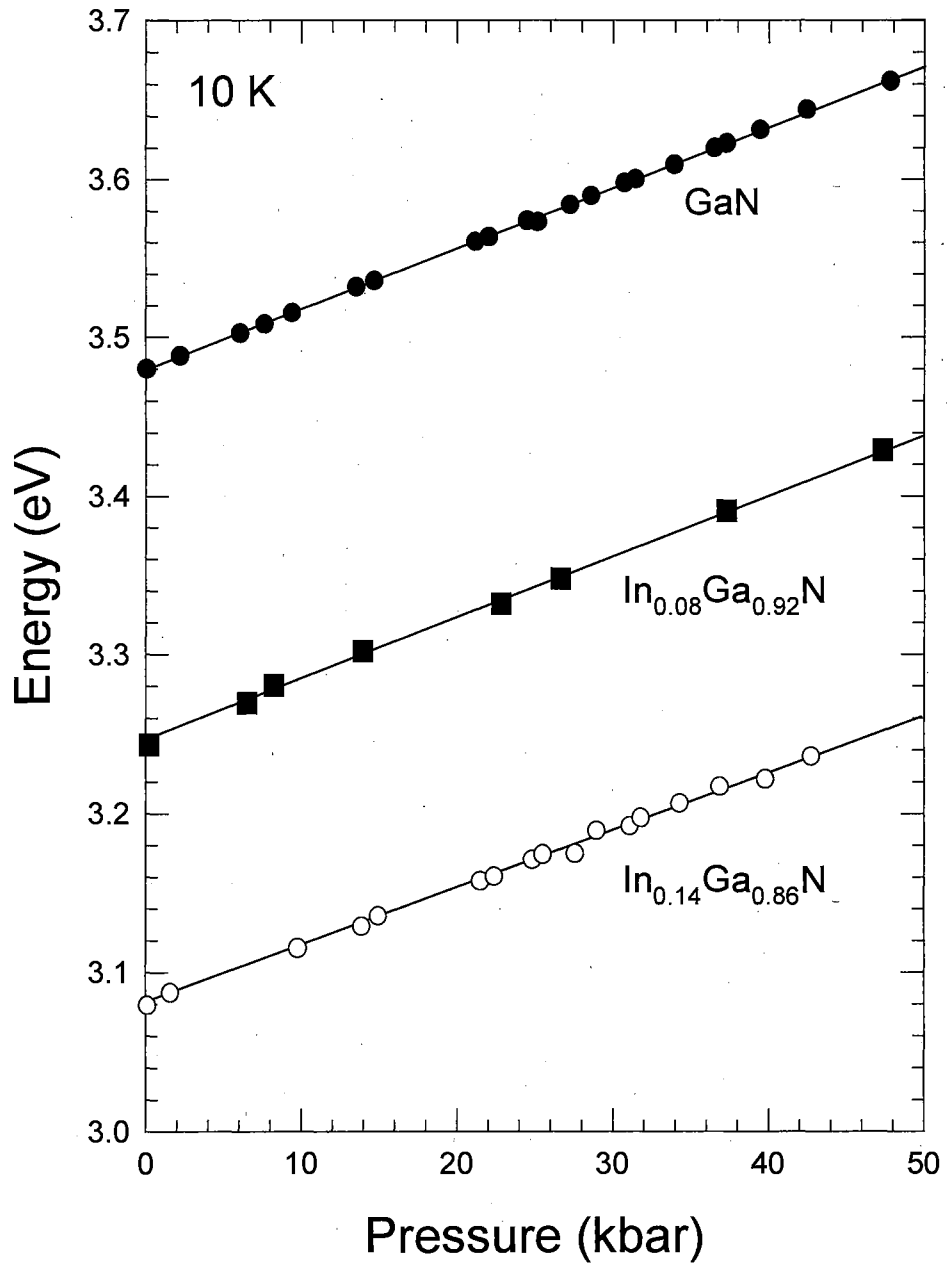


Figure 42. Pressure dependence of the near-bandedge PL transition energy at 10 K for the InGaN alloys and GaN.

Dynamics of Photoexcited Carriers in AlGaN/GaN Double Heterostructures

In this section, we present the results of a time-resolved luminescence study of the spontaneous lifetime of photoexcited carriers in AlGaN/GaN DHs. An emphasis is put on the determination of an effective carrier capture time that describes the process of carriers being photogenerated in the AlGaN cladding layer of the DHs, and subsequently drifting and diffusing into the GaN active region before recombining through various channels. Using the observed lifetimes, we calculate the minority carrier diffusion constant and average drift velocity for the DH samples.

The AlGaN/GaN DHs used in this work were deposited on nominally undoped thick single-crystal GaN epilayers grown on either SiC or sapphire substrates by MOCVD, with both substrates oriented in the (0001) direction. AlN nucleation layers were deposited on the substrates before the growth of GaN. The thicknesses of the GaN epilayers were around 3 μm , and they were deposited at 1050 $^{\circ}\text{C}$ directly on the AlN layers. PL measurements were taken using the system pictured in Figure 11 (a) with a photon-counting PMT system for detection. TRPL measurements were performed using the setup shown in Figure 14. The time evolution of the signal was investigated using a streak camera in synchroscan mode with a temporal resolution of 2 ps, and the overall resolution of the TRPL system was less than 15 ps. The excitation power density was kept below 5 mW/cm^2 with a beam spot of ~ 500 μm focused on the samples.

Figure 43 shows the PL spectra of two DH samples at 10 K. The spectra are offset vertically for clarity. The upper curve corresponds to an $\text{Al}_{0.03}\text{Ga}_{0.97}\text{N}/\text{GaN}$ DH grown on sapphire consisting of a 2000 \AA GaN active layer symmetrically surrounded by 4000 \AA $\text{Al}_{0.03}\text{Ga}_{0.97}\text{N}$ cladding layers. The sample corresponding to the lower curve is an $\text{Al}_{0.1}\text{Ga}_{0.9}\text{N}/\text{GaN}$ DH grown on SiC with a structure similar to the first sample, except the thickness of the GaN active layer is 600 \AA and the top alloy cladding layer is 2300 \AA

thick. The peaks around 3.47-3.48 eV in the figure are associated with near-band-edge emissions from the GaN layers and are dominated by bound exciton luminescence peaks. The difference in the positions of these GaN peaks between the two samples is due to the effects of residual strain, as discussed in the previous chapter. The strong and relatively broad emission structures at higher energy are related to the radiative recombination of photoexcited carriers in the AlGa_{0.9}N cladding layers of the samples, as labeled in the figure. A detailed analysis of these lineshapes has been published elsewhere.¹⁰⁸ The inset of Figure 43 shows the 10 K reflectance spectra for the Al_{0.1}Ga_{0.9}N/GaN DH grown on SiC, with the positions of the GaN-related *A*, *B*, and *C* free exciton transitions marked by arrows. The observation of these excitonic signatures, which originate from the active region of the sample, indicates that the sample is of very high quality. Figure 44 shows the PL spectra of the Al_{0.03}Ga_{0.97}N/GaN DH sample at selected temperatures using a pulsed laser with an excitation wavelength of 290 nm. Due to the shorter wavelength (and hence, smaller penetration depth) of this excitation source compared to that in the main graph of Figure 43, the incident photons should be completely absorbed by the 4000 Å Al_{0.03}Ga_{0.97}N top cladding layer without creating a significant amount of carriers in the GaN active region. The observation of a GaN-related peak under these excitation conditions is due to carrier diffusion. The fast quenching of the PL intensity of the GaN active layer with increasing temperature compared to that of the alloy layer confirms that the luminescence signal arises from the radiative recombination of carriers that were generated in the alloy cladding layer and then reached the active region by diffusion due to a carrier concentration gradient. As the temperature of the sample increases, the probability of a photoexcited carrier reaching the active region decreases due to thermally enhanced nonradiative recombination and various scattering processes.

Figure 45 shows the time evolution of the spectrally integrated PL signal measured simultaneously from the AlGa_{0.9}N alloy cladding layer (triangles) and the GaN active region (circles) of the Al_{0.1}Ga_{0.9}N/GaN DH sample. A delay in the initial increase of the GaN luminescence signal compared to that of AlGa_{0.9}N is clearly observed. This temporal behavior can be attributed to the effect of an accumulation of photoexcited carriers within the GaN active region by a carrier capture process that involves the diffusion of photoexcited carriers from the Al_{0.1}Ga_{0.9}N cladding layer into the GaN active

region and inelastic scatterings within the GaN layer mainly by LO phonon emissions.^{141,142,143} The dynamics of the photoexcited carriers (including generation, diffusion, spontaneous recombination, and nonradiative relaxation) can be described, for a low generation rate, by the following rate equations:

$$dn_{\text{AlGaN}}/dt = G(t) - n_{\text{AlGaN}}/\tau_D - n_{\text{AlGaN}}/\tau_{\text{AlGaN}}, \quad (5-2)$$

$$dn_{\text{GaN}}/dt = n_{\text{AlGaN}}/\tau_D - n_{\text{GaN}}/\tau_{\text{GaN}}, \quad (5-3)$$

where n_{AlGaN} and n_{GaN} are the carrier concentrations in the AlGaN cladding and the GaN active layers, respectively, $G(t)$ is the generation rate (dependent on the actual excitation laser pulse), τ_D is the effective carrier capture lifetime, and τ_{AlGaN} and τ_{GaN} are the effective lifetimes (τ_{eff}) of spontaneous recombination for carriers in the AlGaN and GaN layers, respectively.

The solid lines in Figure 45 are the best fits to the experimental data using Equations 5-2 and 5-3. The fitting results yield a capture time of $\tau_D \sim 350$ ps and effective lifetimes of $\tau_{\text{AlGaN}} \sim 150$ ps and $\tau_{\text{GaN}} \sim 280$ ps for spontaneous recombination in the top alloy cladding layer and the GaN active region of the $\text{Al}_{0.1}\text{Ga}_{0.9}\text{N}/\text{GaN}$ sample, respectively. As mentioned above, the effective carrier capture time τ_D consists of two contributions. The first arises from the drift and diffusion of the photoexcited carriers from the top AlGaN cladding layer into the GaN active region, and is driven by the variation of carrier concentration at different positions in the sample. The second arises from the inelastic scattering of carriers reaching the active region, which allows them to dissipate their excess energy, primarily via LO phonon emission. However, the macroscopic transport properties of the carriers in the AlGaN cladding layers should be dominant in determining the capture time discussed here because of the very short time scale of inelastic scattering processes such as LO phonon emission.^{144,145} The value of $\tau_{\text{GaN}} \sim 280$ ps is significantly longer than the reported values of 50-75 ps for high quality GaN epilayers measured using the same experimental system.^{128,146} This indicates that the dynamics of the carriers in the GaN active region is governed by the carrier diffusion dominated capture process: while the population of carriers already accumulated in the GaN active layer decreases by spontaneous recombination and relaxation, there are also a

number of carriers drifting into the region due to diffusion from the cladding layer over a period of time characterized by τ_D after the photogeneration laser pulse. Consequently, the temporal profile of the luminescence from the GaN layer exhibits a slow rising and a longer decay time.

Figure 46 presents the results of TRPL experiments on the $\text{Al}_{0.03}\text{Ga}_{0.97}\text{N}/\text{GaN}$ DH sample. Using the approach described above, a capture time of $\tau_D \sim 600$ ps and effective lifetimes of $\tau_{\text{AlGaN}} \sim 70$ ps and $\tau_{\text{GaN}} \sim 180$ ps were obtained for this sample. The difference in the deduced spontaneous lifetimes for the $\text{Al}_x\text{Ga}_{1-x}\text{N}$ layers with different x values used in this work is related to the different quality and compositions of the alloys, since the spontaneous recombination of photoexcited carriers involves both radiative and nonradiative processes as described by Equation 3-3. The material quality of the samples also affects the value of τ_{GaN} . However, the difference in the GaN layer thicknesses of the samples studied is not likely to have significant influence on τ_{GaN} since the GaN region can be treated as a three-dimensional electronic system, primarily due to the fact that the layer thickness is much larger than the size of the overlap of the electron and hole wave functions (*i.e.* the exciton radius). The observed differences in the value of τ_D results from the different thicknesses of the AlGaN cladding layers as well as the different initial excess energies of the photoexcited carriers (due to the different alloy concentrations of the cladding layers). The values of τ_D measured here should be considered to be the effective capture time for the holes because of the background n -type doping ($N_D - N_A$ is on the order of 10^{16} - 10^{17} cm^{-3}) in the MOCVD-grown GaN active layer and AlGaN alloys.

There is some additional information we can get from these results if we consider the nature of the generation/diffusion/recombination process. After being photogenerated near the surface of the sample by the absorbed laser light, minority carriers diffuse into the sample and recombine with majority carriers within a depth determined by the diffusion properties of the sample.^{147,148} Thus, the capture time τ_D can be used to make an estimate of the diffusion constant for minority carriers in the AlGaN alloy regions of these samples using the following equation:

$$\tau_D = L^2/D, \quad (5-4)$$

where L is the thickness of the top AlGa_xN cladding layer of the DH samples corresponding to the diffusion length defined by standard diffusion theory^{56,149} and D is the diffusion constant for the carriers. The results yield $D \sim 2.6 \text{ cm}^2/\text{s}$ for Al_{0.03}Ga_{0.97}N and $D \sim 1.5 \text{ cm}^2/\text{s}$ for Al_{0.1}Ga_{0.9}N at 10 K. The difference between these values can be explained by two possible mechanisms: (1) an increased effect of alloy disorder-induced potential fluctuation scattering on the carrier diffusion process, and (2) the increase in carrier effective mass with Al concentration, which results in a reduction of the carrier mobility. The diffusion constants obtained here should be considered an upper limit to the actual values. This is due to the fact that the effective carrier capture time τ_D determined in this work represents a lower limit to the actual value since the influence of nonradiative recombination at the interface region is not included in Equations 5-2 and 5-3.

Using the diffusion lifetimes obtained from TRPL measurements above, we can estimate the average carrier drift velocity by taking into account the distance the carriers must traverse before they reach the GaN active region and recombine. We can estimate the drift velocity using the relation:

$$v_d \sim d/\tau_D, \quad (5-5)$$

where d is the distance the carriers travel before recombining, *i.e.* the top cladding layer thickness. Using the experimentally determined values of $\tau_D = 350 \text{ ps}$ and the thickness $d = 2300 \text{ \AA}$ for the DH on SiC, we get a drift velocity of $v_d = 6.6 \times 10^4 \text{ cm/s}$. Using $\tau_D = 600 \text{ ps}$ and $d = 4000 \text{ \AA}$ for the DH on sapphire gives a value of $v_d = 6.7 \times 10^4 \text{ cm/s}$. The extremely good agreement between the values of v_d for these two samples is partially due to the simplicity of Equation 5-5, but should also provide reassurance that the model used to describe the generation, drift and diffusion, and eventual recombination of carriers in the DH systems studied here is reliable.

In conclusion, we have studied the dynamics of photoexcited carriers in Al_xGa_{1-x}N/GaN heterostructures by performing picosecond time-resolved luminescence spectroscopy measurements. The dynamics of the system, which include the generation, diffusion, spontaneous recombination, and nonradiative relaxation of the photoexcited

carriers in the DH samples, has been studied by examining the time evolution of the luminescence signal associated with the spontaneous recombination of photoexcited carriers in the GaN active region and the AlGaN cladding layers. The effective carrier capture time as well as the effective lifetimes of the spontaneous recombination for carriers in the AlGaN cladding layers and the GaN active regions of the DH samples were determined by numerical fits to the experimental results using a set of dynamic rate equations. Based on these results, we estimated an upper limit for the diffusion constant of minority carriers in the AlGaN layers of the samples and calculated an average carrier drift velocity.

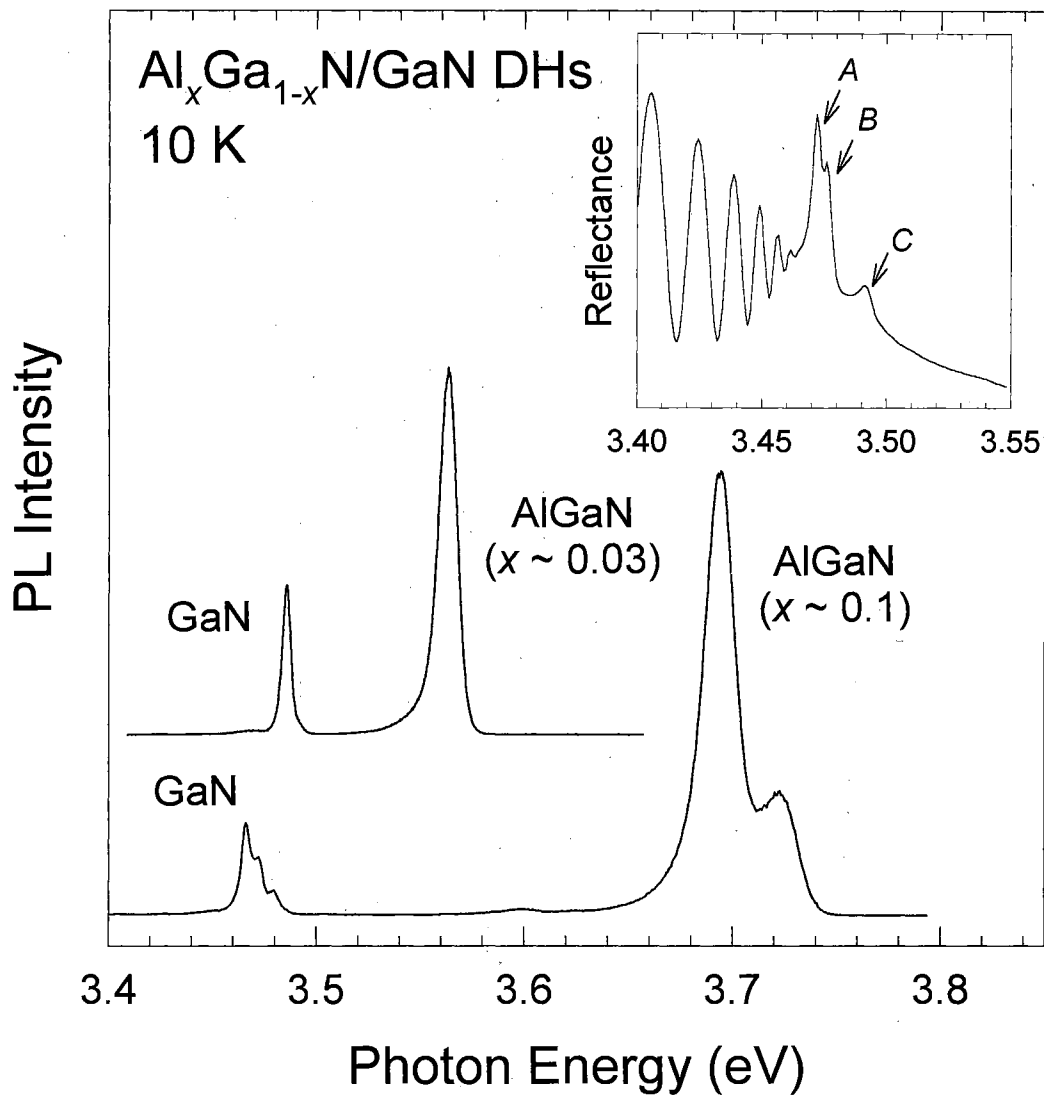


Figure 43. 10 K PL spectra taken from an Al_{0.03}Ga_{0.97}N/GaN DH grown on sapphire (top) and an Al_{0.1}Ga_{0.9}N/GaN DH grown on SiC (bottom). The spectra are offset for clarity. The inset shows the 10 K reflectance spectrum from the Al_{0.1}Ga_{0.9}N/GaN sample, with arrows marking the A, B, and C exciton transition signatures.

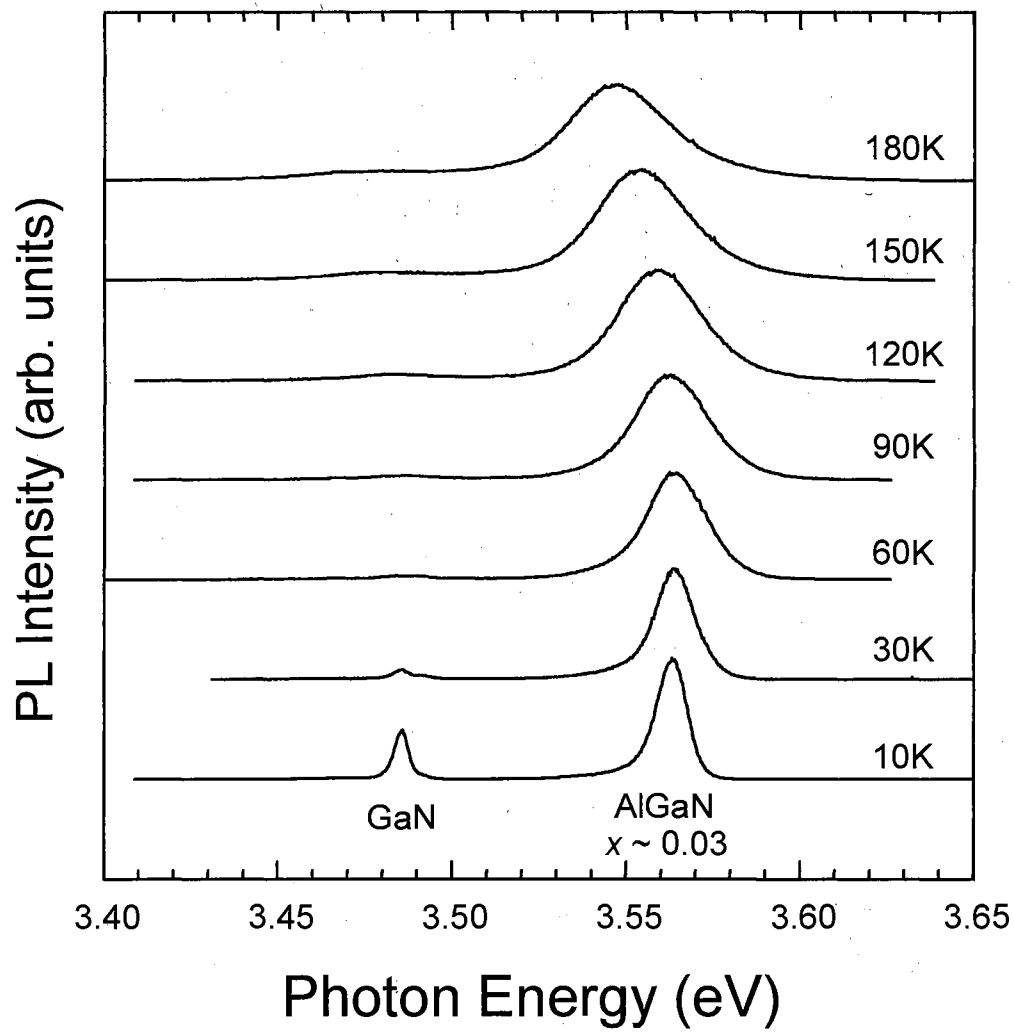


Figure 44. PL of an $\text{Al}_{0.03}\text{Ga}_{0.97}\text{N}/\text{GaN}$ DH grown on sapphire, showing the fast quenching of the GaN-related luminescence signal with increasing temperature. The spectra are offset vertically for clarity.

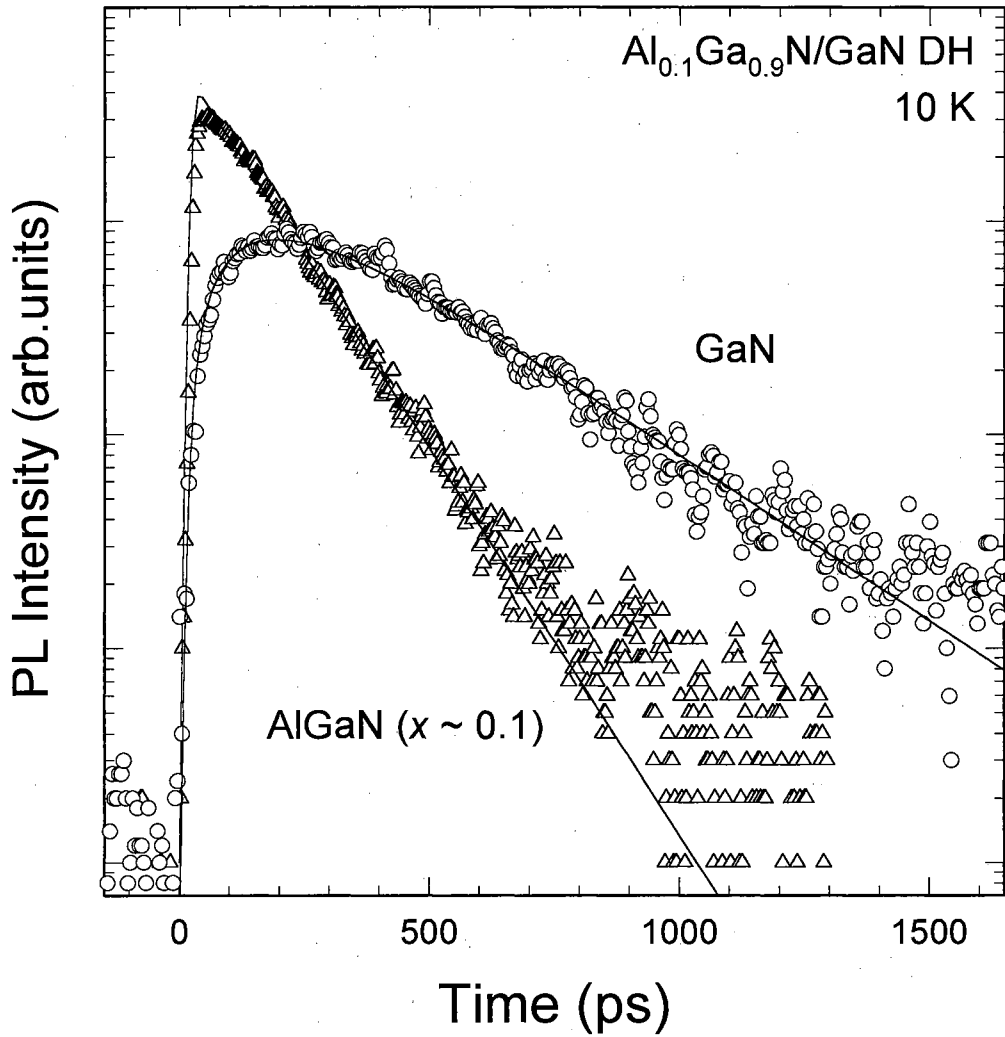


Figure 45. Temporal evolution of the spectrally integrated PL for the AlGaN cladding and GaN active regions of an Al_{0.1}Ga_{0.9}N/GaN DH sample grown on SiC at 10 K. The circles and triangles correspond to the TRPL data for the active region and the cladding, respectively. The solid lines are the best fits to the experimental data.

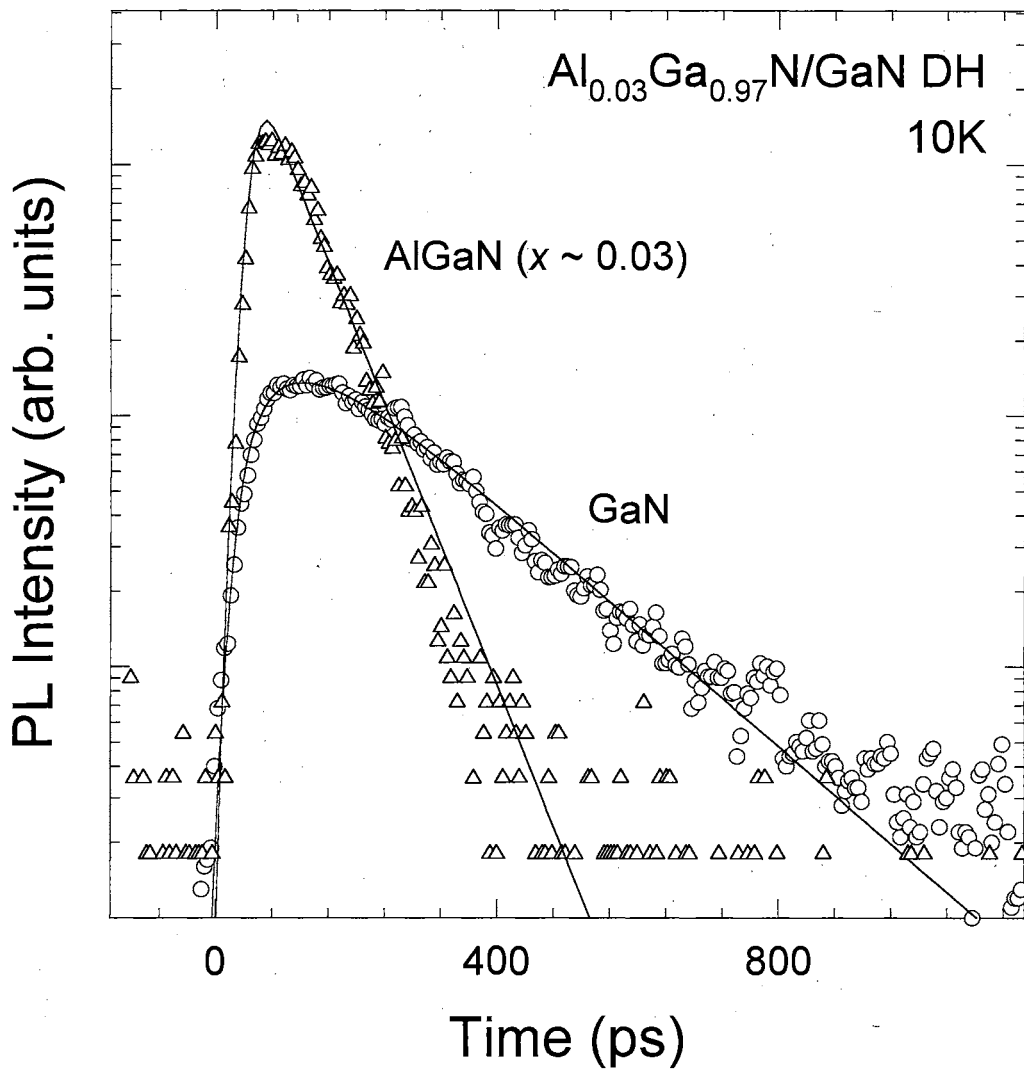


Figure 46. Temporal evolution of the spectrally integrated PL for the AlGaN cladding and GaN active regions of an Al_{0.03}Ga_{0.97}N/GaN DH sample grown on sapphire at 10 K. The circles and triangles correspond to the TRPL data for the active region and the cladding, respectively. The solid lines are the best fits to the experimental data.

Excitation Wavelength Dependence of Stimulated Emission/Lasing from AlGaIn/GaN Separate Confinement Heterostructures

As mentioned in the *Structures* section in Chapter II, optoelectronic devices usually take advantage of the capability of modern epitaxial growth techniques to grow complicated layered thin film structures. Such structures are often necessary to achieve the desired device performance. One structure that is very useful for LDs is the SCH (see Chapter II for a comprehensive description). This structure allows the simultaneous confinement of carriers and output light, improving the efficiency and output characteristics of the device. Here we present the results of a study of the wavelength dependence of SE/lasing from AlGaIn/GaN SCHs. In addition to optical pumping experiments, PL and PLE measurements were performed to gain more information on the emission properties of the SCH sample.

The samples used in this study were grown on (0001) SiC substrates by MOCVD. First, an approximately 3 μm thick GaN layer was deposited. On top of this layer, the following structure was grown: 2300 \AA bottom cladding layer, 800 \AA bottom waveguide layer, 100 \AA GaN active region, 800 \AA top waveguide layer, and finally the top 2300 \AA cladding layer. The structure described here is identical to the one pictured in Figure 9. The samples were mounted to the cold finger of a closed cycle helium refrigerator that allowed continuous temperature tuning from 10 K to 300 K. PL measurements were performed using a setup similar to the one pictured in Figure 11 (a) with a photon counting PMT system for detection, but with the 244 nm line of an intracavity frequency doubled cw Ar⁺ laser for excitation. For PLE spectroscopy, the setup in Figure 11 (b) was employed. SE/lasing was studied with the experimental setup shown in Figure 25 using either the output of a tunable UV dye laser pumped by a XeCl excimer laser or the 308 nm output of the excimer laser itself.

Results of PL experiments on the AlGaIn/GaN SCH at 10 K are shown in Figure 47. The spectrum is characterized by three dominant peaks, which are due to the cladding, waveguide, and active regions of the SCH as indicated in the figure. The smaller feature on the high energy side of the waveguide peak is most likely due to a small ($\sim 1\%$) deviation in Al composition between the two symmetrically located waveguide regions. The optical quality of the sample is quite good, judging from the sharpness of the PL emission lines. Next, optical pumping experiments were performed at RT. The result is shown in Figure 48. Single-mode lasing occurred at a wavelength of 362 nm, with a threshold pumping density of $\sim 125 \text{ kW/cm}^2$. This threshold value is $5\times$ lower than the typical value found for SE in GaN epilayers.¹⁵⁰ In addition, the wavelength position of the lasing peak is blueshifted by 11 nm compared to GaN epilayers. Of particular interest in this figure is the extremely narrow linewidth of the lasing peak ($\sim 3 \text{ \AA}$), indicating the high quality of the active region and the presence of significant optical feedback (due to cracks in samples grown on SiC). 10 K lasing experiments were performed, and the resultant data is presented in Figure 49. The dominant structure on the right side of the spectrum is lasing from the active region of the SCH, whereas the weaker peak on the left is PL originating from the waveguide region. The lasing wavelength has blueshifted 4 nm compared to the RT value. The detailed power dependence of the luminescence from the SCH is shown in Figure 50 at 10 K. The onset of lasing from the active region can be clearly seen by the superlinear increase in integrated emission intensity compared to the slightly sublinear increase in the cladding layer peak.

Valuable information about the lasing properties of the SCH can be achieved by comparing the RT and 10 K lasing data. First of all, the FWHM of the lasing peak does not change over this large temperature range. Secondly, the difference in the position of the lasing wavelengths at RT and 10 K is only 4 nm, which corresponds to 38 meV. This value is extremely small compared to the amount that the bandgap of GaN shifts over the same temperature range ($\sim 140 \text{ meV}$). These two observations are an indication that lasing in the SCH sample is dominated by the exciton-exciton gain mechanism.¹⁵¹

Next, the excitation wavelength dependence of the lasing in the SCH was studied using a tunable UV dye laser pumped by the XeCl excimer. We found a marked increase

in the lasing threshold when the excitation source was tuned to wavelengths above 346 nm, as pictured by the solid dots on the top graph of Figure 51. The dashed line is a guide for the eye. To elucidate the origin of this increase, we compared the wavelength dependent lasing threshold to the PL and PLE spectra from the SCH. As seen by the solid line in the top graph of Figure 51, the wavelength at which the increase in lasing threshold was observed lines up with the PL emission originating from the AlGaIn waveguide layer. In addition, we see a change in the PLE spectrum at this same position, which is shown in the bottom graph in Figure 51. The most likely explanation of these observations deals with the small absorption cross section in the thin active region of the SCH. If the active region is pumped near resonance, there is only a 100 Å layer that can contribute to the absorption of the excitation photons. A quick calculation using Beer's Law (Equation 3-4) tells us that only 63.2% of the pump laser will be absorbed in the active region. The rest passes through the sample until it is absorbed by the GaN buffer layer and is wasted in terms of optical pumping efficiency. When the excitation source is tuned above the bandgap energy of the waveguide region, they will start to absorb the incoming photons. While some of the carriers photoexcited by the pump laser will radiatively combine and give rise to the short wavelength spontaneous emission signal seen in Figures Figure 49 and Figure 50, others should drift and diffuse into the GaN active region, as discussed in the last section. These injected carriers give rise to the lasing peak in the active region. Due to the high quality of the SCH sample studied here, this process is an extremely efficient method of carrier transfer. Thus, the decrease of the lasing threshold seen at 346 nm is due to the increased absorption of the pump beam by the waveguide, followed by the drift and diffusion of the photoexcited carriers from the waveguide to the active region.

To support this theory, we present the spectrum shown in Figure 52, which shows the results of near resonant optical pumping of the SCH at RT. Two peaks are observed, at 362 and 373 nm. The 362 nm peak is the same peak observed for pumping at 308 nm, *i.e.* lasing from the active region of the SCH. The 373 nm peak, however, occurs at the same wavelength as SE from GaN epilayers. As mentioned before, 36.8% of the near resonant pump beam passes through the active region. In this case, the light not absorbed

by the active region passes through to the buffer layer, where it is still strong enough to produce a population inversion and hence SE.

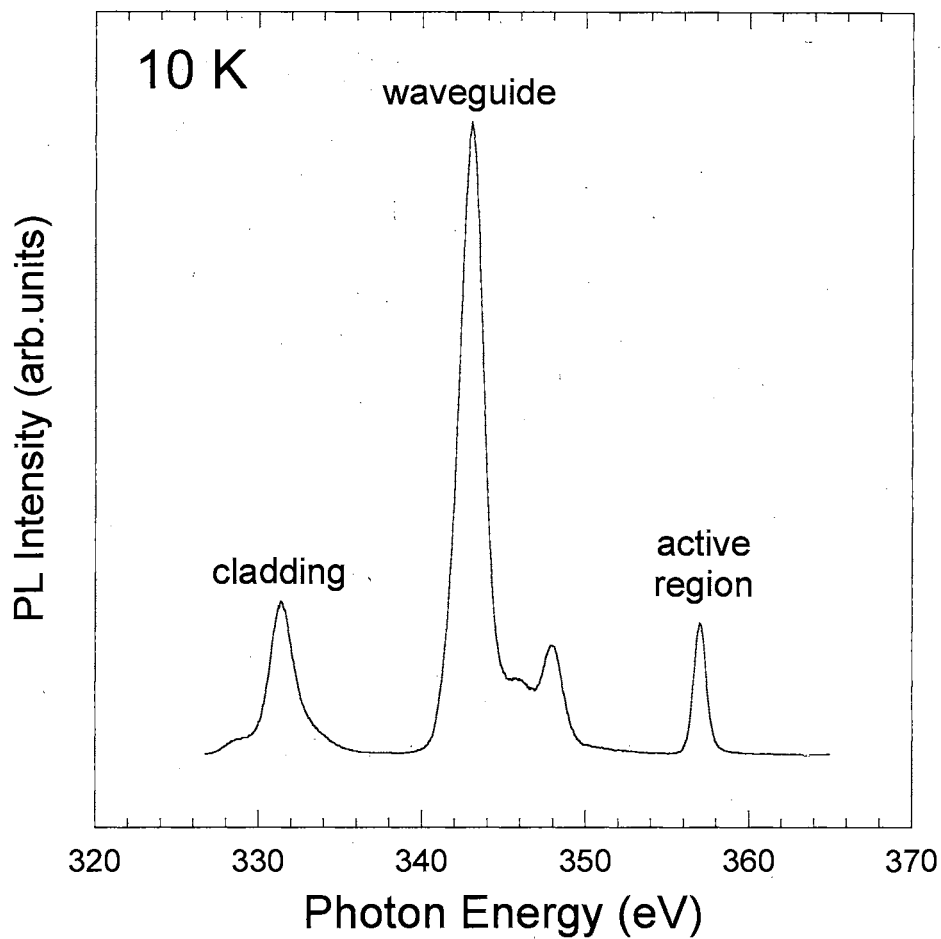


Figure 47. 10 K PL of the AlGa_{0.11}N/GaN SCH. Three distinct peaks from the Al_{0.11}Ga_{0.89}N cladding, Al_{0.06}Ga_{0.94}N waveguide, and GaN active region can be seen. The small spectral feature between the waveguide and active region peaks at ~ 348 nm is most likely due to a small (~ 1%) difference in alloy concentration between the two symmetrically located waveguide layers.

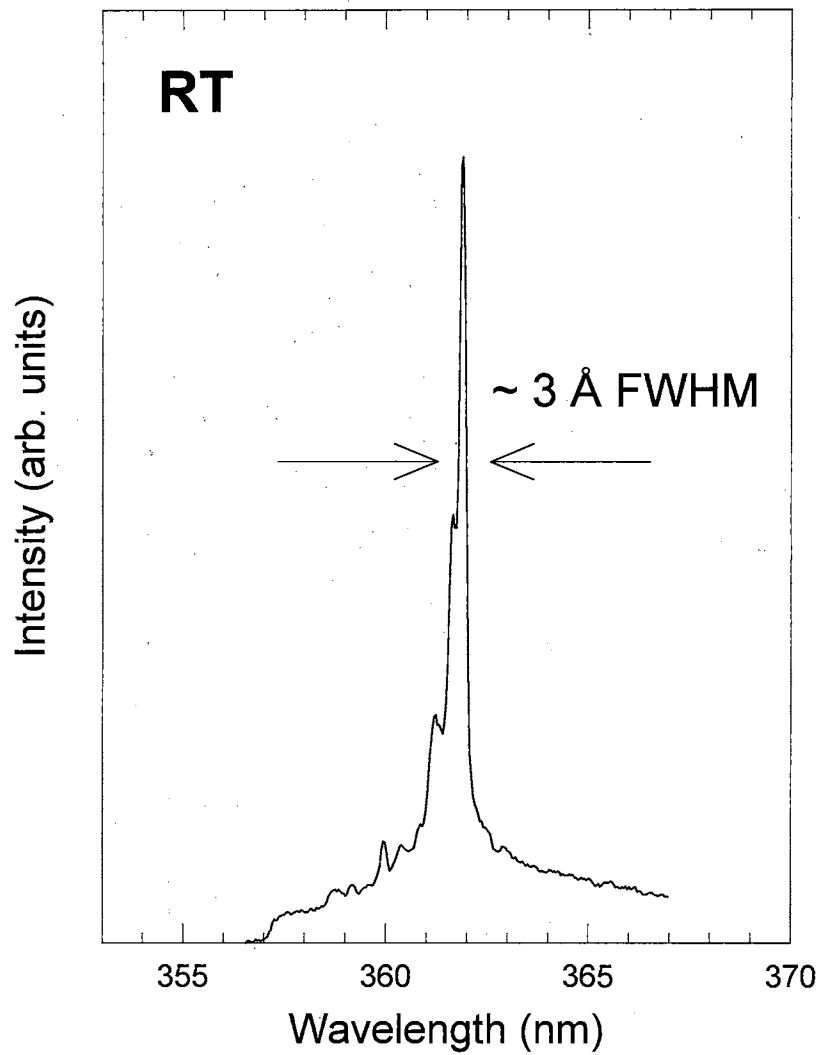


Figure 48. Typical RT lasing spectrum of the AlGaIn/GaN SCH structure. The pump source was a XeCl excimer laser at 308 nm. The lasing is characterized by a low threshold intensity ($\sim 125 \text{ kW/cm}^2$) and a narrow linewidth ($\sim 3 \text{ \AA}$ FWHM). The lasing peak is blueshifted by 11 nm compared to GaN epilayers.

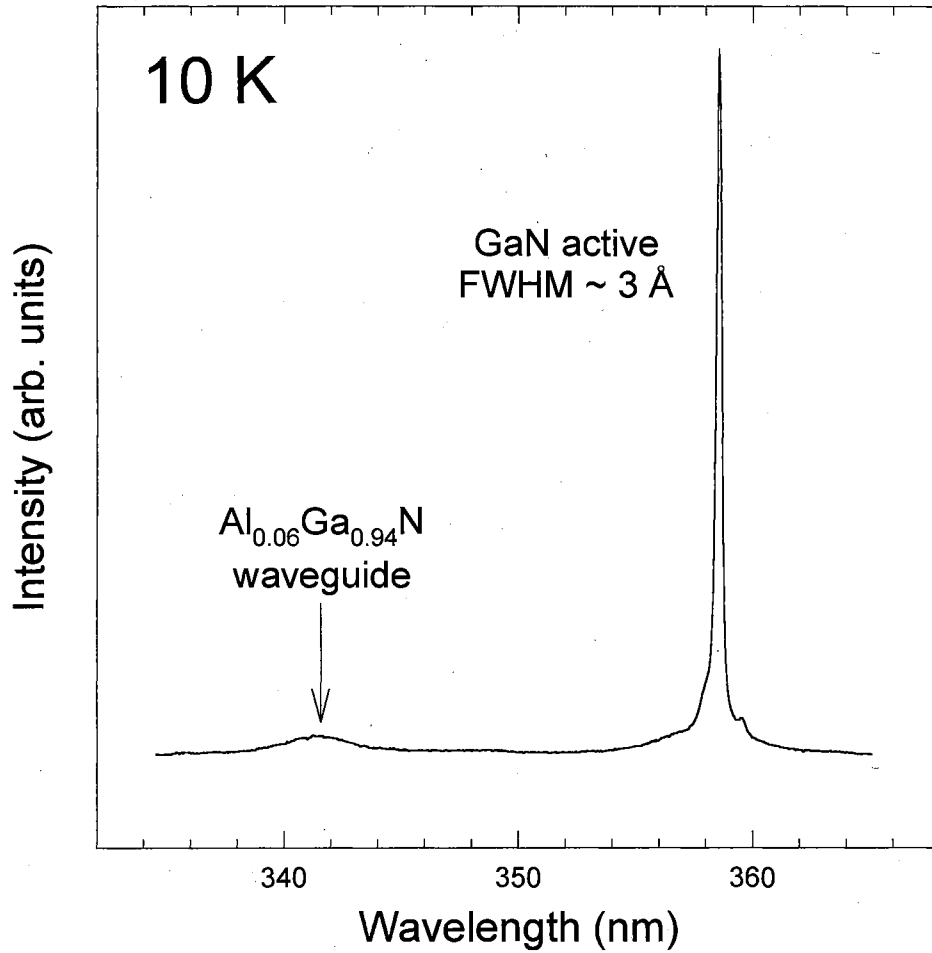


Figure 49. Typical 10 K lasing spectrum of the SCH. An extremely narrow lasing peak is seen at $\sim 358 \text{ nm}$ from the active region of the SCH. The weak structure at shorter wavelength is PL emission from the AlGa N waveguide region.

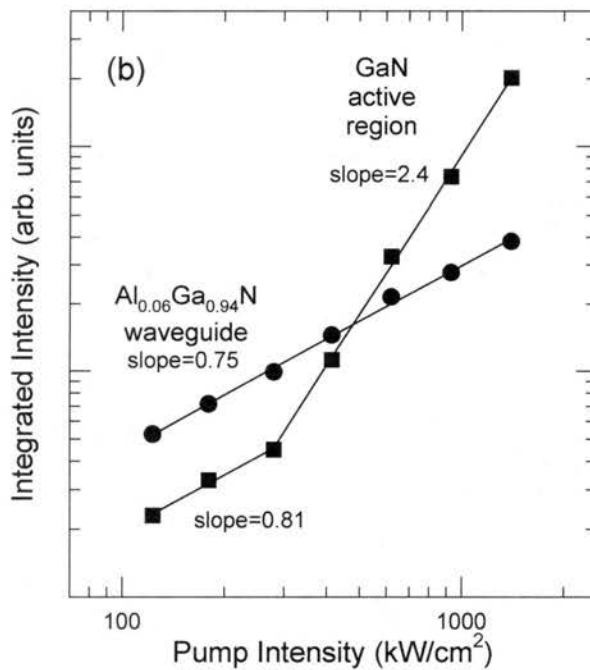
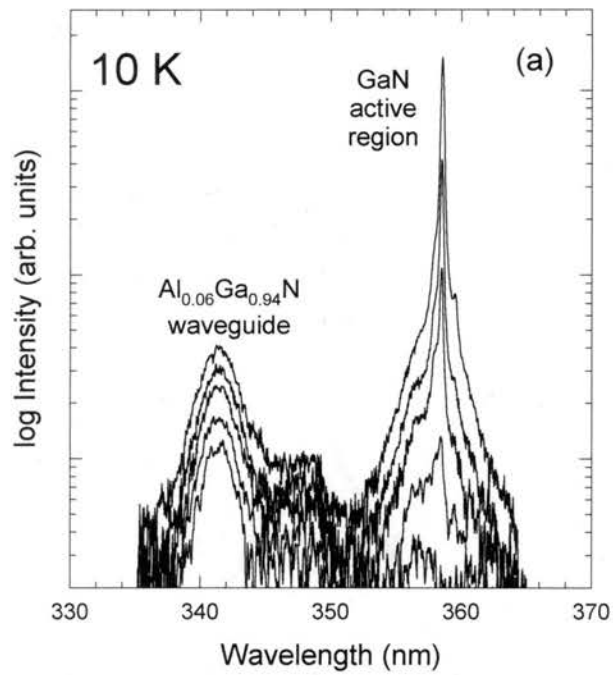


Figure 50. Power dependence of the luminescence from the SCH at 10 K, showing the onset of lasing. The sample was pumped by a XeCl laser at 308 nm.

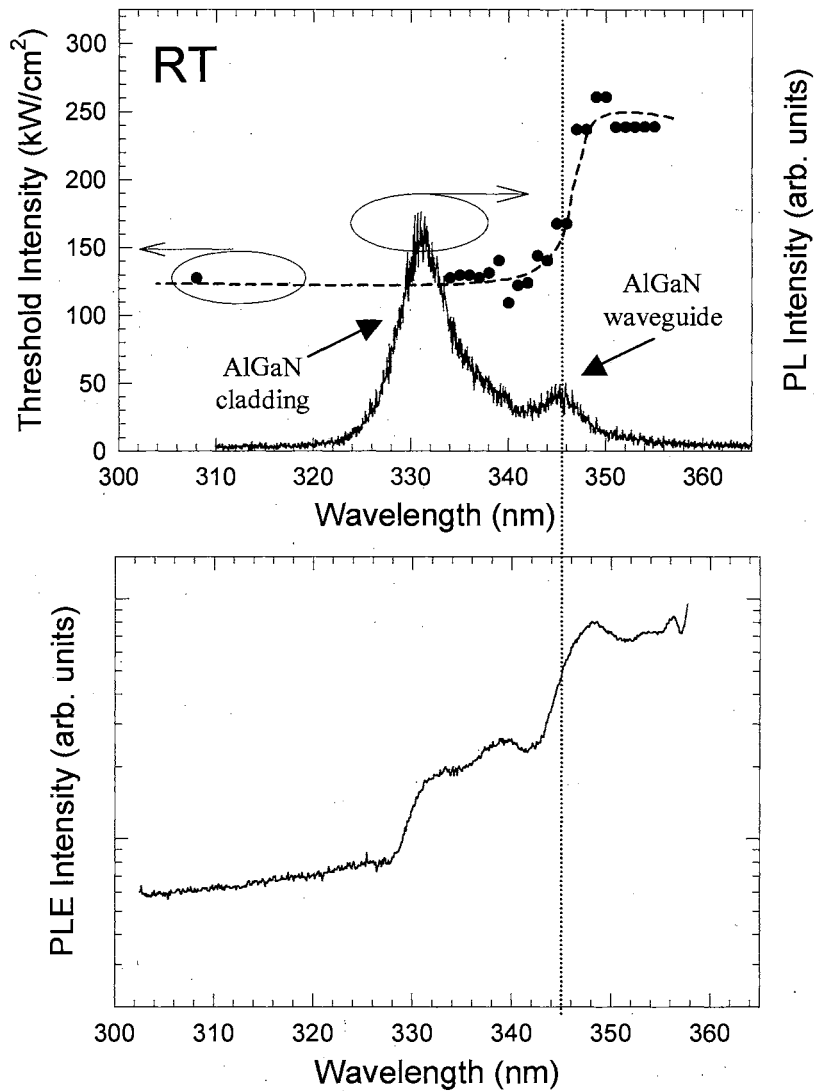


Figure 51. Results of various experiments on the SCH sample at RT: (a) PL (solid line) and pump wavelength dependence of the lasing threshold (data points are given by solid circles, the dashed line is a guide for the eye) and (b) PLE. The dashed vertical line shows the approximate position of the bandedge for the $\text{Al}_{0.06}\text{Ga}_{0.94}\text{N}$ waveguide region.

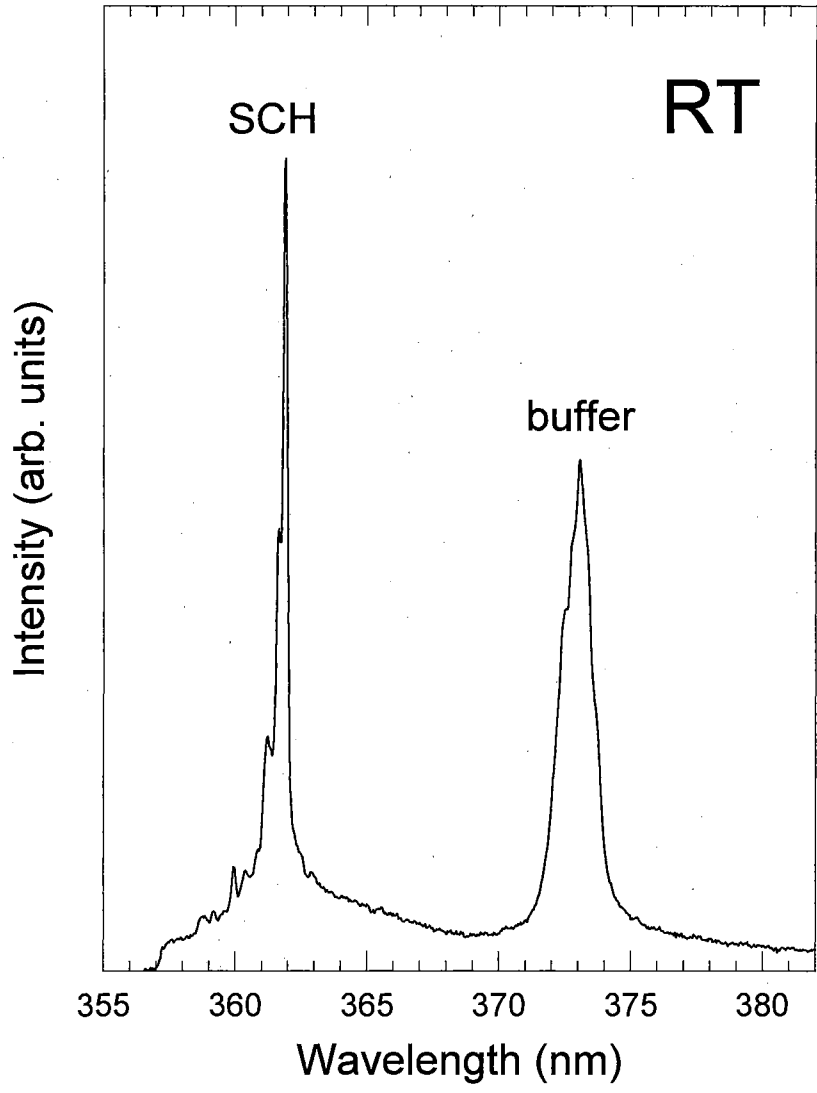


Figure 52. SE/lasing at RT seen simultaneously from the GaN buffer layer and the active region for a near-resonant pumping wavelength.

Comparison of Emission from Highly Excited (In,Al)GaN Thin Films and Heterostructures

(In,Al)GaN epilayers and heterostructures have drawn much attention in recent years due to the potential for blue/UV light emitters and detectors for use in high density data storage, high temperature electronics, solar blind detectors, atmospheric sensing, and medicine.¹ Recently, nearly a dozen research groups have demonstrated lasing in InGaN-based heterostructures, with the lowest reported emission wavelength being 376 nm.¹⁵² To obtain shorter wavelength laser diodes, it is necessary to use AlGaN-based structures. Preliminary studies have shown that the incorporation of Al into GaN increases the SE threshold.¹⁵³ In this work, we demonstrate that the introduction of strong optical and carrier confinement into AlGaN/GaN heterostructures can significantly reduce the SE threshold. We also demonstrate SE in AlGaN epilayers with emission wavelengths as low as 327 nm at room temperature, illustrating that AlGaN is a suitable material for the development of deep UV LDs.

The GaN, InGaN, and AlGaN epilayers studied were grown on (0001) sapphire substrates by MOCVD. The thickness of the $\text{Al}_x\text{Ga}_{1-x}\text{N}$ layers were $\sim 0.8 \mu\text{m}$, and they had alloy concentrations of $x = 0.17$ and 0.26 . For the purpose of comparison, we used GaN and InGaN epilayers with thicknesses ranging from 100 nm to $7.2 \mu\text{m}$. The sample growth parameters have been reported elsewhere.^{154,155} We also studied an AlGaN/GaN SCH grown by MOCVD on SiC (this is the same sample that was discussed in the last section). The active region of the SCH was a 100 Å thick GaN layer, which was sandwiched between 800 Å $\text{Al}_{0.06}\text{Ga}_{0.94}\text{N}$ cladding layers and 2300 Å $\text{Al}_{0.11}\text{Ga}_{0.89}\text{N}$ waveguiding layers. The structure was deposited on top of a $\sim 3 \mu\text{m}$ GaN buffer layer.

The experimental setup for the study of SE was identical to that pictured in Figure 25, with nanosecond tunable dye lasers pumped by either the doubled output of an

injection seeded Nd:YAG laser (~ 7 ns pulsewidth and 10 Hz repetition rate at 532 nm) or the 308 nm XeCl line of an excimer laser (~ 8 ns pulsewidth and 10 Hz repetition rate). In the case of Nd:YAG pumping, the deep orange output of the dye laser was doubled to ~ 310 nm using a nonlinear crystal. The excimer-pumped dye laser emitted directly in the UV. PL was performed using the setup shown in Figure 11 (a), with the 244 nm line of an intracavity frequency doubled cw Ar⁺ laser for excitation.

SE from the AlGa_N epilayers qualitatively resembles that seen in Ga_N epilayers. However, the emission wavelength lies in the deep UV. The RT emission spectra for AlGa_N layers with alloy concentrations of 17% and 26% are shown in Figure 53 (a) and (b), respectively, for excitation densities above and below the SE threshold intensity I_{th} . The dashed line indicates low power cw PL results. As seen from the figure, SE for both samples emerges out of the low energy wing of the spontaneous emission peak as the excitation density is increased. When this data was originally published,¹⁵³ it was the shortest wavelength SE that had been reported for any semiconductor. The spontaneous and stimulated emission peaks are separated by 10.5 and 8.5 nm, respectively, for the 17% and 26% epilayers, which is comparable to the spacing observed in Ga_N epilayers¹⁵⁰ and is considerably smaller than that seen in InGa_N epilayers.¹⁵⁶ The redshift of the spontaneous emission seen under nanosecond excitation in Figure 53 (a) and (b) compared to the cw spontaneous emission peaks is due to a reabsorption of the emitted radiation as it travels along the excitation path in the edge-emission experiments.

Figure 54 illustrates the emission intensity of the spontaneous and stimulated emission peaks as a function of excitation intensity I_{exc} for the AlGa_N epilayers presented in Figure 53. The spontaneous emission is seen to increase roughly linearly across the entire range of I_{exc} . Above I_{th} , we see the emergence of a new peak which exhibits a superlinear increase in emission intensity with I_{exc} , clearly indicating the onset of SE.¹⁵⁷ The values of I_{th} obtained from the AlGa_N epilayers are slightly larger than those obtained from high quality Ga_N epilayers, and are more than an order of magnitude greater than those of InGa_N epilayers. The high SE threshold for AlGa_N epilayers makes the development of LDs using this material rather challenging.

Through this study, however, we show that AlGa_N/Ga_N-based heterostructures can be used to produce lasing with both short emission wavelengths and low lasing

thresholds. The SCH used in this study possesses a high degree of optical and carrier confinement. By pumping the sample at 335 nm, we obtained lasing at 358 nm for 10 K and 362 nm for RT with a lasing threshold as low as 125 kW/cm². Figure 50 shows the RT emission spectra from the SCH at several excitation intensities above and below I_{th} . The shorter wavelength peak at 341 nm is due to spontaneous emission from the $x = 0.06$ AlGaIn waveguide region. As I_{exc} is increased, we see a narrow lasing peak (3 Å FWHM) emerge at a wavelength of 358 nm. We did not observe any broadening of this peak as the temperature was raised up to RT. This indicates that the FWHM of the lasing peak is determined by the finesse of the cavity, which remains independent of temperature. In our previous study, we showed that the cavity is formed by microcracks caused by strain relaxation of AlGaIn grown on SiC.¹⁵⁸ Figure 50 (b) shows the detailed behavior of the emitted intensity as a function of I_{exc} . As can be seen from the graph, the cladding layer emission increases almost linearly with increasing I_{exc} . The emission from the active region behaves linearly until I_{th} is reached, after which a superlinear increase is observed. The RT SE threshold value for this sample was determined to be 125 kW/cm², representing a drastic reduction in comparison to GaN and AlGaIn epilayers. This low threshold value is made possible by the carrier confinement and optical waveguiding properties of the structure. In fact, the lasing threshold is comparable to the best InGaIn epilayers, which makes it suitable for the development of short wavelength LDs ($\lambda_{emission} < 370$ nm at RT). It may be possible to further reduce the threshold by optimizing the sample parameters such as active layer thickness as well as the thickness and alloy concentrations of the cladding and waveguiding region.

In conclusion, we have systematically studied the SE properties of (In,Al)GaIn thin films and heterostructures. The SE threshold of AlGaIn epilayers was found to increase with increasing Al content compared to GaN, in contrast to InGaIn epilayers, where an order of magnitude decrease is observed. RT SE was observed at remarkably short wavelengths, demonstrating that AlGaIn-based structures are a suitable material for deep UV LDs. Furthermore, we achieved a substantial reduction in the lasing threshold for AlGaIn/GaN-based heterostructures. We showed that optical and carrier confinement will play key roles in the reduction of the lasing threshold in these structures.

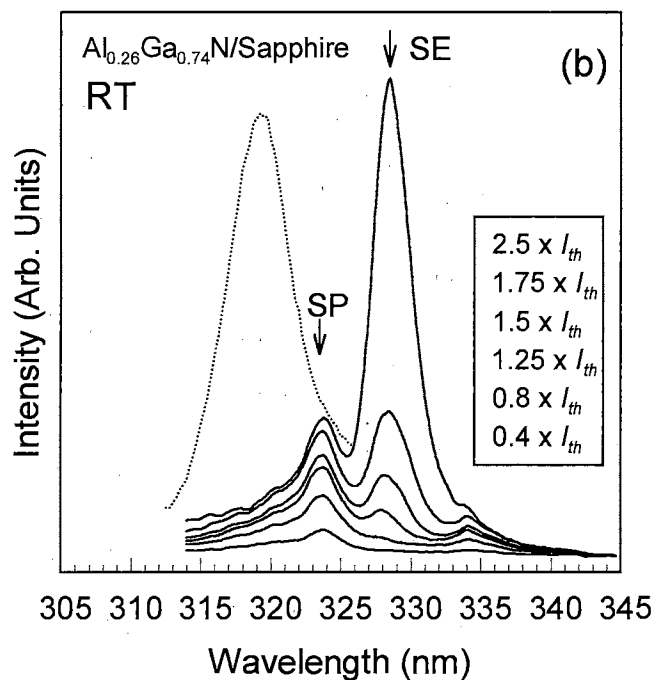
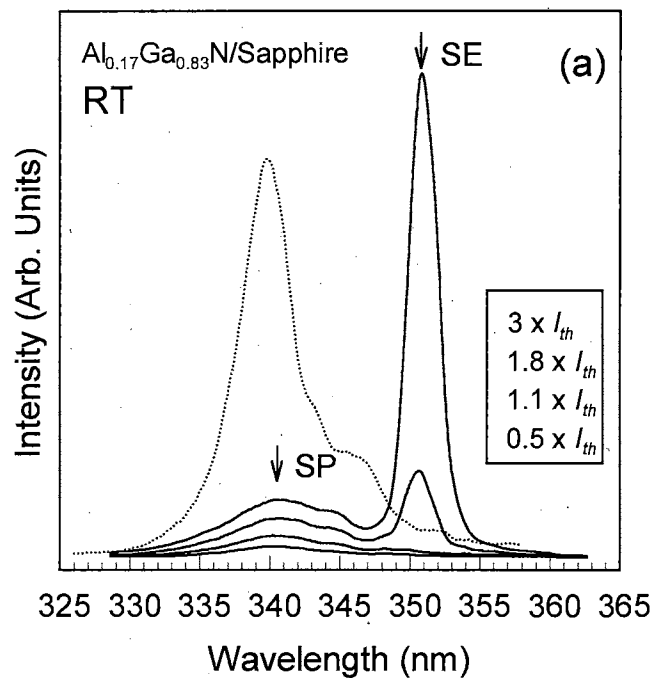


Figure 53. RT SE spectra at pump intensities above and below the SE threshold, I_{th} , for AlGaN layers with alloy concentrations of (a) 17% and (b) 26%. Low power cw spontaneous emission is given by the dashed line for each graph.

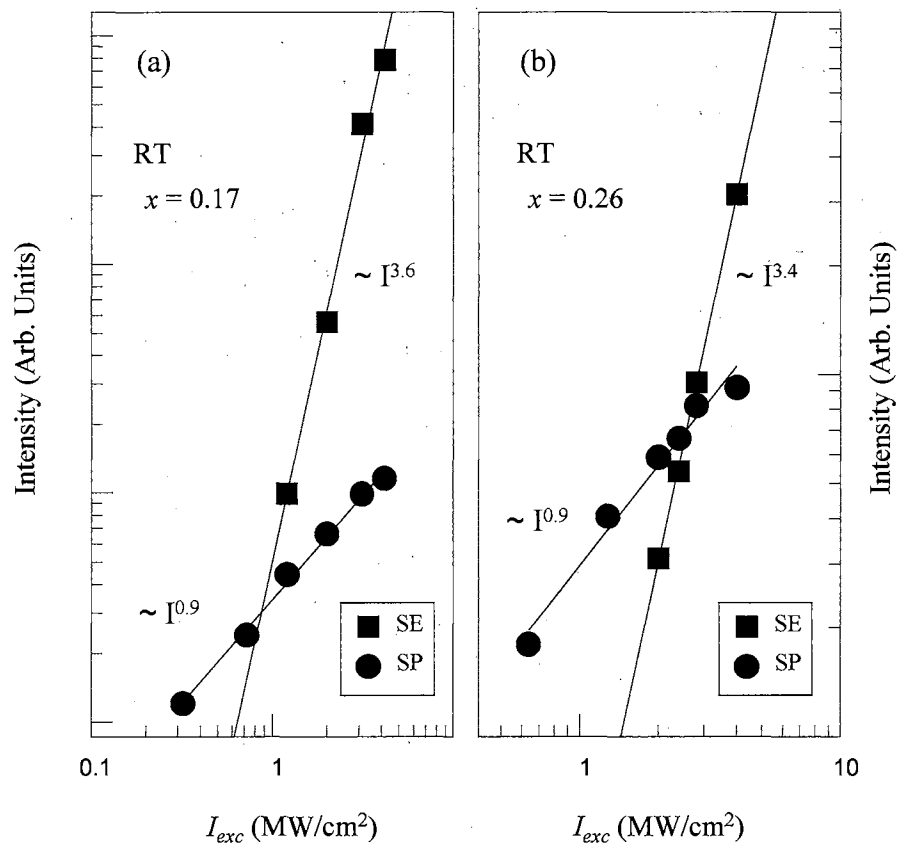


Figure 54. Power dependence of the SE from the AlGaIn alloy samples at RT. The spontaneous emission peaks, denoted by circles, show an approximately linear increase with excitation intensity. SE exhibits a superlinear increase with power, and is represented by squares.

CHAPTER VI

EXPERIMENTAL INVESTIGATIONS OF ZnO

As discussed in the Introduction, ZnO is a potentially useful material whose reputation is quickly escalating. It has the potential to become an important UV-blue light emitting material, however there are still many obstacles to be overcome, such as *p*-doping, contacts, and alloying. The current state of research on ZnO is lagging several years behind the III-Nitrides, but much of the information learned through studying the III-Nitrides can be applied to ZnO,¹⁵⁹ for instance, methods of reducing the background *n*-type carrier concentration, achieving *p*-type doping, and growing high quality alloys. It is likely that we will begin to see functional optoelectronic devices fabricated from this material system in the near future.

Two recent advances in the ZnO research community have been the successful growth of bulk ZnO crystals and the growth of extremely high quality epilayers through the use of a new type of buffer layer. The bulk ZnO crystal was grown using VPT. A 2" diameter wafer with a thickness of 1 mm was cut from the boule, and then lapped and chemomechanically polished to obtain atomically flat surfaces (one Zn-terminated, the other O-terminated).⁷⁹ The epilayer was grown on an O-terminated sapphire substrate using MBE.⁶⁷ To obtain extremely high quality, a 2.5-3 nm MgO buffer layer was used, which facilitates the initial nucleation and promotes lateral growth of ZnO. This results in a smooth surface morphology and layer-by-layer epitaxial growth.

Comparison of the Optical and Structural Properties of Bulk and Epitaxial ZnO Crystals

We studied the optical and structural quality of these two ZnO samples through a combination of PL and XRD experiments. PL was performed using the setup shown in Figure 11 (a) with a 244 nm Ar⁺ laser as the excitation source and a UV-enhanced photon counting PMT for detection. X-ray was performed using a Philips X'Pert diffractometer with Cu K α_1 radiation.

To illustrate the increase in quality of the ZnO epilayer grown using a MgO buffer, we present in Figure 55 the temperature dependent PL of a ZnO epilayer grown using the same method, but with no buffer layer. Shown in Figure 56 is the 10 K PL spectrum of the epilayer with the MgO buffer. In comparison to Figure 55, we see a number of sharp and narrow luminescence peaks, which suggest a significant improvement in the optical quality by the incorporation of the MgO layer. These peaks have been preliminarily attributed to neutral-donor-bound exciton transitions in ZnO where the neutral donors are pair-type complexes.¹⁶⁰ A similar phenomenon is seen in the bulk ZnO crystal, as evidenced in Figure 57, which shows the PL signal at selected temperatures between 10 and 110 K. Accordingly, the bound exciton signatures quench quickly with increasing temperature. Because it is exceptionally pure material, the bulk crystal is expected to show very high quality. The fact that the PL spectrum from the epilayer so closely resembles that from the bulk sample is proof of the high quality of the epilayer.

Even though the epitaxial and bulk samples exhibit similar PL spectra, XRD results show substantial differences in the structural properties of the two samples. Shown in the top graph of Figure 58 are ω - 2θ diffraction curves taken for different X-ray source slit widths from 50 to 300 μm . The spectra exhibit an extremely narrow FWHM

of ~ 30 arcsec, which is unaffected by the increase in slit width. Figure 59 shows the same thing for the bulk sample. In this case, we see a substantial increase in the FWHM value as the slit width increases. The minimum FWHM observed (30 arcsec for 50 μm slits) is consistent with the epilayer sample, but the increase is strikingly different.

The reason for this increase in FWHM can be established by considering what is happening at the sample surface in conjunction with the type of information weaned from XRD measurements. XRD spectra give us information about the lattice parameters in crystalline materials. The FWHM values of XRD spectra give us insight into the spread of lattice parameters of the sample, *i.e.* how much deviation in lattice parameter there is throughout the area probed by the X-ray beam. For small slit widths, we are looking at a small spot near the surface of the sample. When the slit width of the X-ray source is increased, the resultant spot size on the surface of the sample increases proportionally. A large FWHM in ω - 2θ diffraction scans indicates the presence of multicrystalline domains, each with slightly different lattice parameters. Thus, what we are seeing from the bulk sample is the presence of multicrystalline domains. The minimum domain size, assuming the epilayer sample is a perfect single-crystal, is around 50 μm .

Even though the bulk ZnO sample has been found to be multicrystalline, it should not significantly affect its use as a substrate for the homoepitaxial growth of ZnO or the heteroepitaxial growth of the III-Nitrides. Indeed, high quality films are often grown on substrates with significant lattice mismatch. After a few monolayers of crystal growth, it is likely that the multicrystalline domains would merge and undergo three-dimensional growth, producing a single-crystal epilayer.

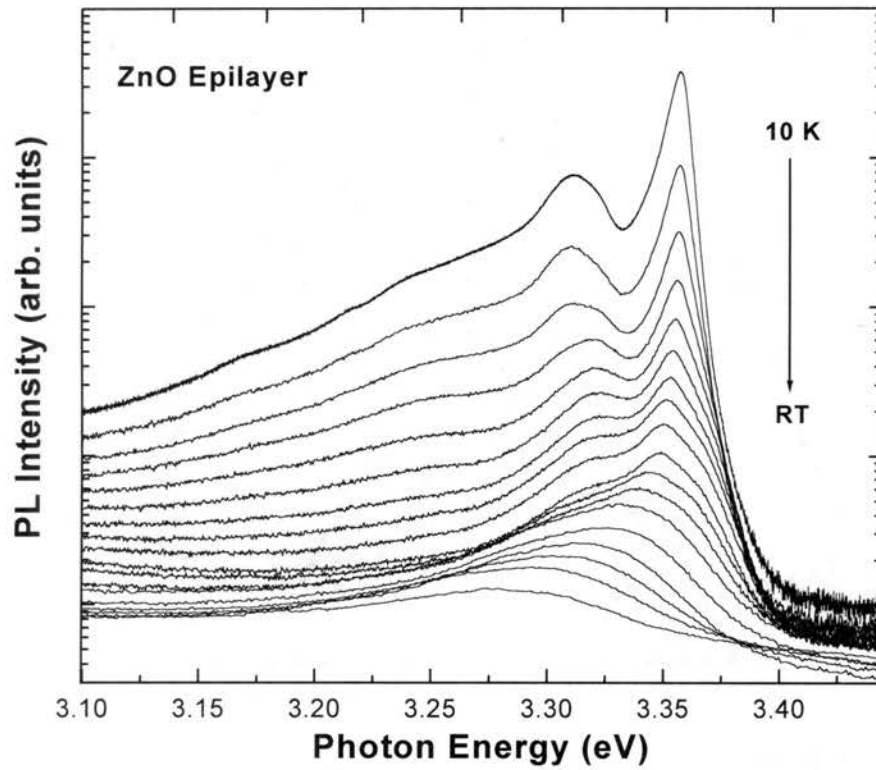


Figure 55. Temperature dependent PL of a ZnO epilayer grown on sapphire with no buffer layer. The 10 K spectrum is dominated by excitonic luminescence. As the temperature increases, the exciton decreases in intensity and broadens, but remains the dominant luminescence peak.

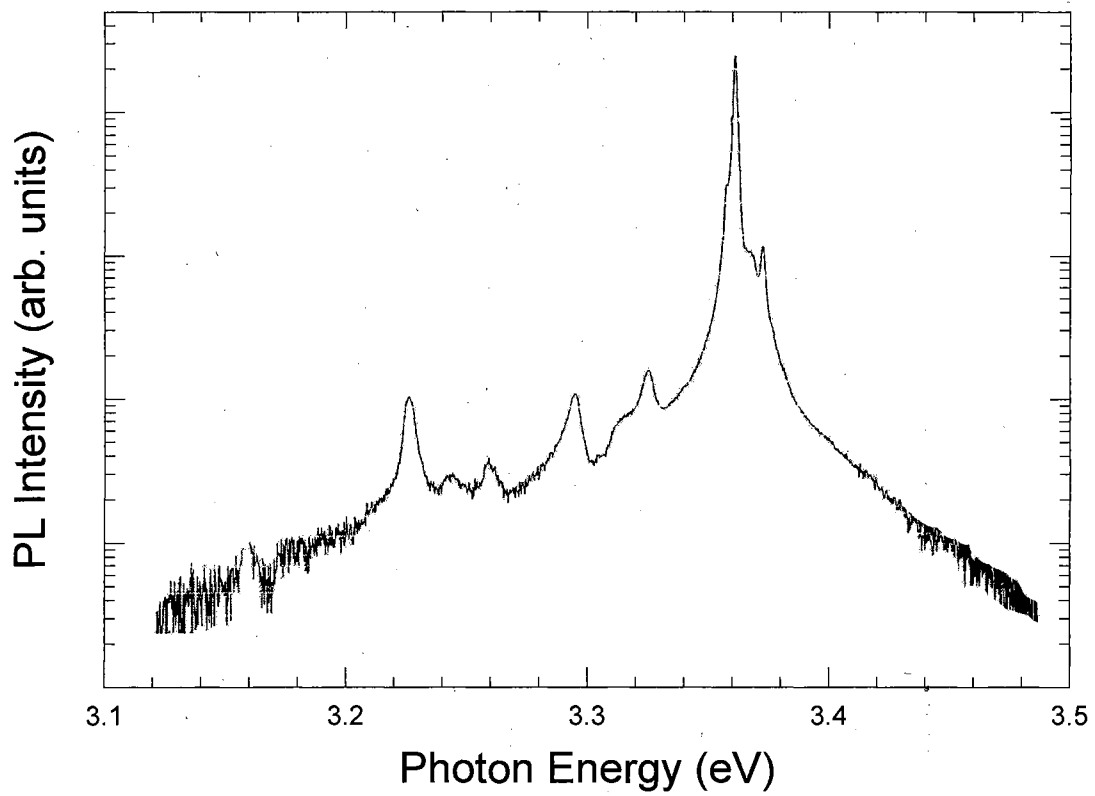


Figure 56. 5 K PL spectrum of a ZnO epilayer grown by MBE using a MgO buffer layer. Several sharp and narrow peaks can be seen in the near bandedge region.

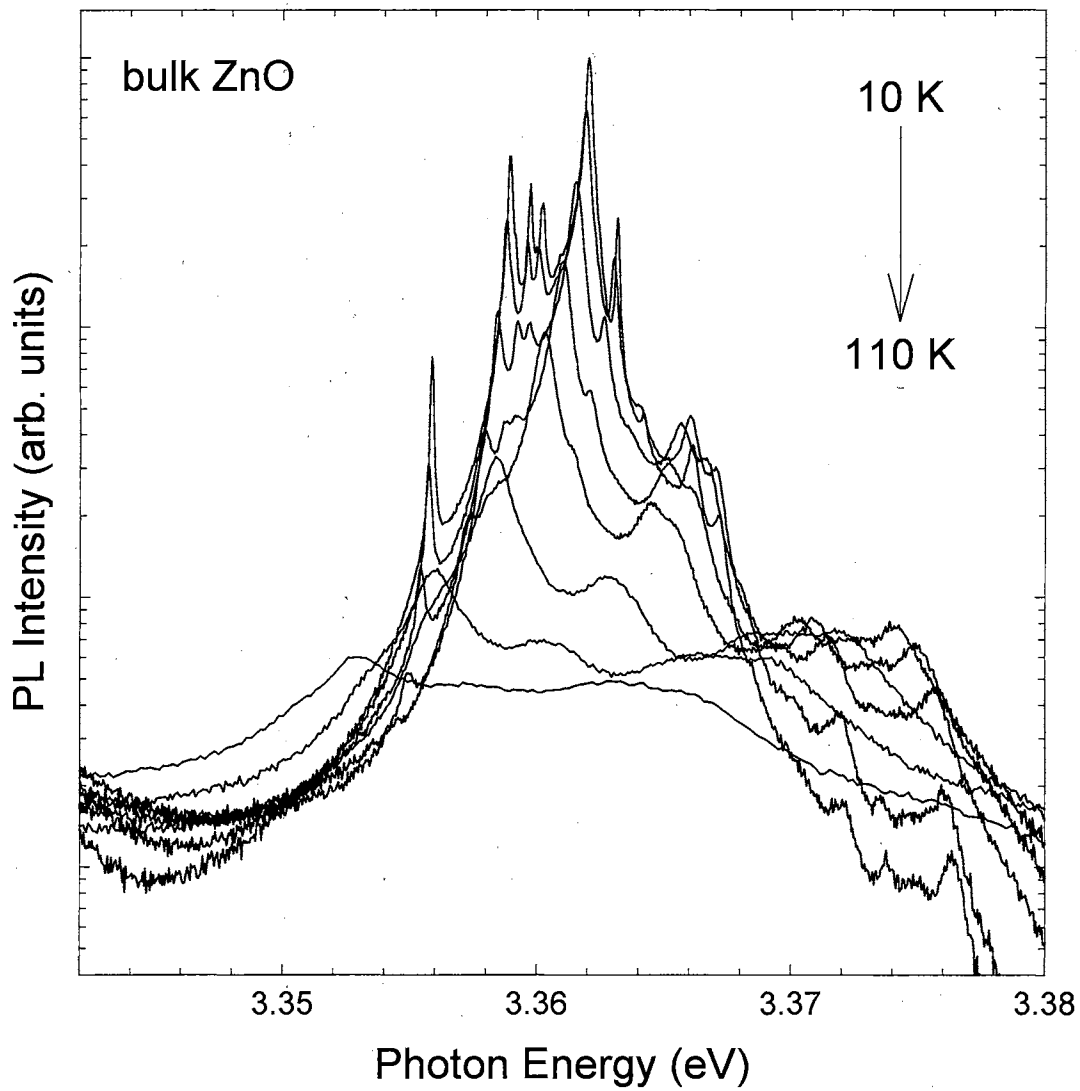


Figure 57. PL spectra of a bulk ZnO crystal at selected temperatures from 10 to 110 K, showing the quenching of the bound exciton luminescence peaks.

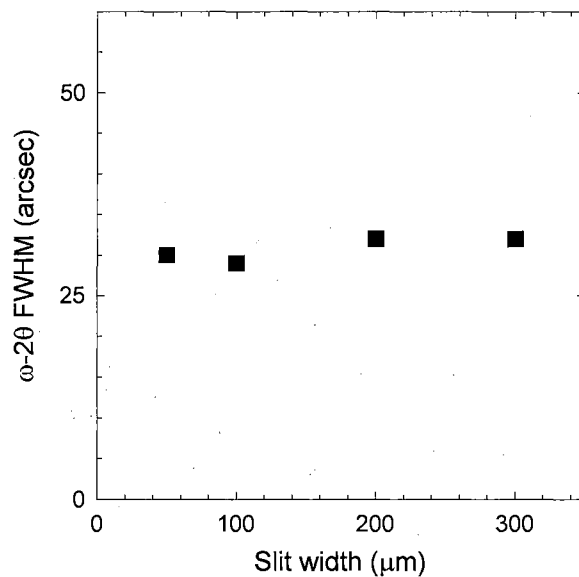
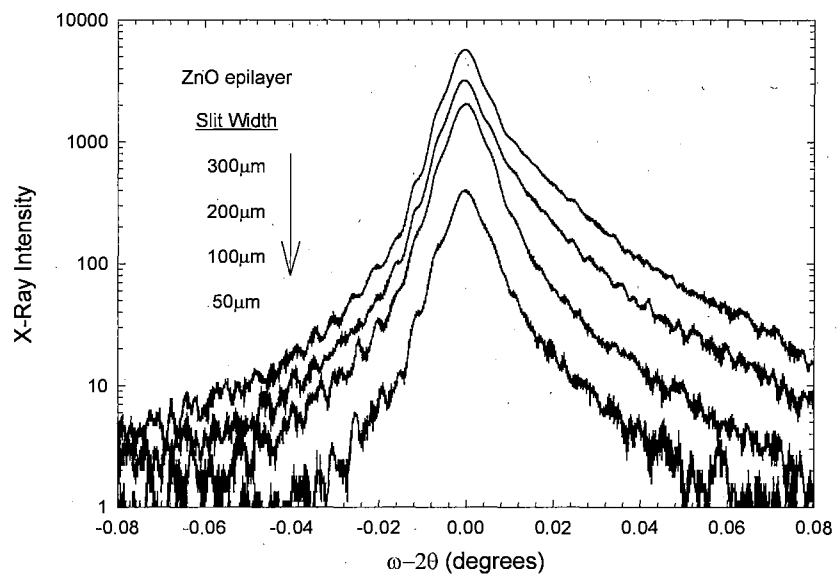


Figure 58. XRD results from a ZnO epilayer grown on sapphire by MBE. As the slit width is increased, the FWHM of the $\omega-2\theta$ diffraction remains constant.

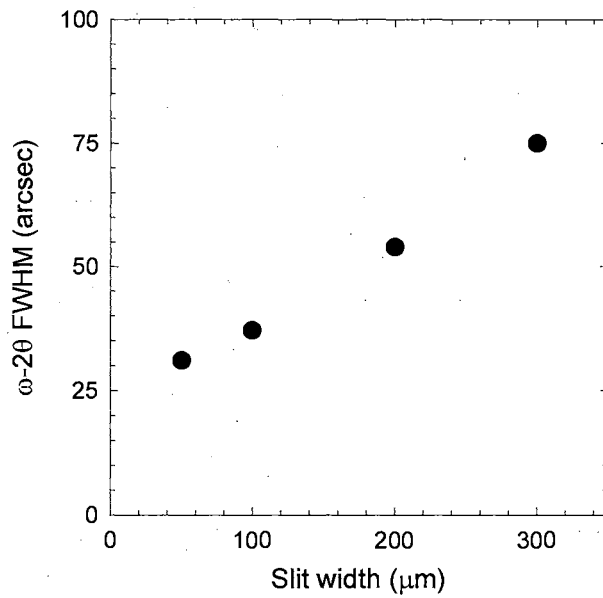
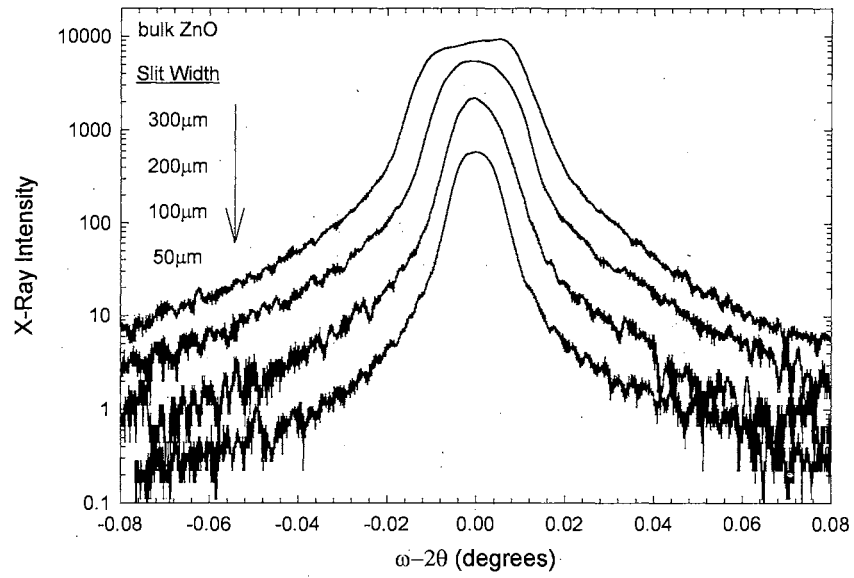


Figure 59. XRD results from a bulk ZnO crystal. As the slit width is increased, the FWHM of the $\omega-2\theta$ diffraction increases.

Stimulated Emission Properties of ZnO

To study the potential of these two new types of high quality ZnO samples for LD applications, we have performed a study of SE. The bulk sample did not exhibit SE, regardless of the temperature or pump intensity used. This is likely due to the presence of multicrystalline domain boundaries, which would scatter the SE and inhibit optical feedback. The epitaxial sample, however, exhibited SE with a threshold density of 340 kW/cm². The optical pumping spectra are seen in Figure 60 for several pump intensities above and below the SE threshold. Although this is not as low a threshold as observed in some of the III-Nitrides as presented in the previous chapters, especially InGaN, it is a respectable threshold value, and should allow for the fabrication of LDs once the doping and contact issues have been worked out. The SE peak is seen to rise out of the tail of the spontaneous emission peak around 3.16 eV. Figure 61 shows the detailed power dependence of the emission from the ZnO epilayer. As seen in the figure, the sample shows a transition to a strongly superlinear increase (slope = 3) in integrated intensity at a pump intensity near 340 kW/cm². Even at low pump intensities, however, the sample exhibits a superlinear (slope = 1.5) increase. This is currently under investigation, but is believed to be due to an enhancement of the emission intensity by the presence of excitons at RT.

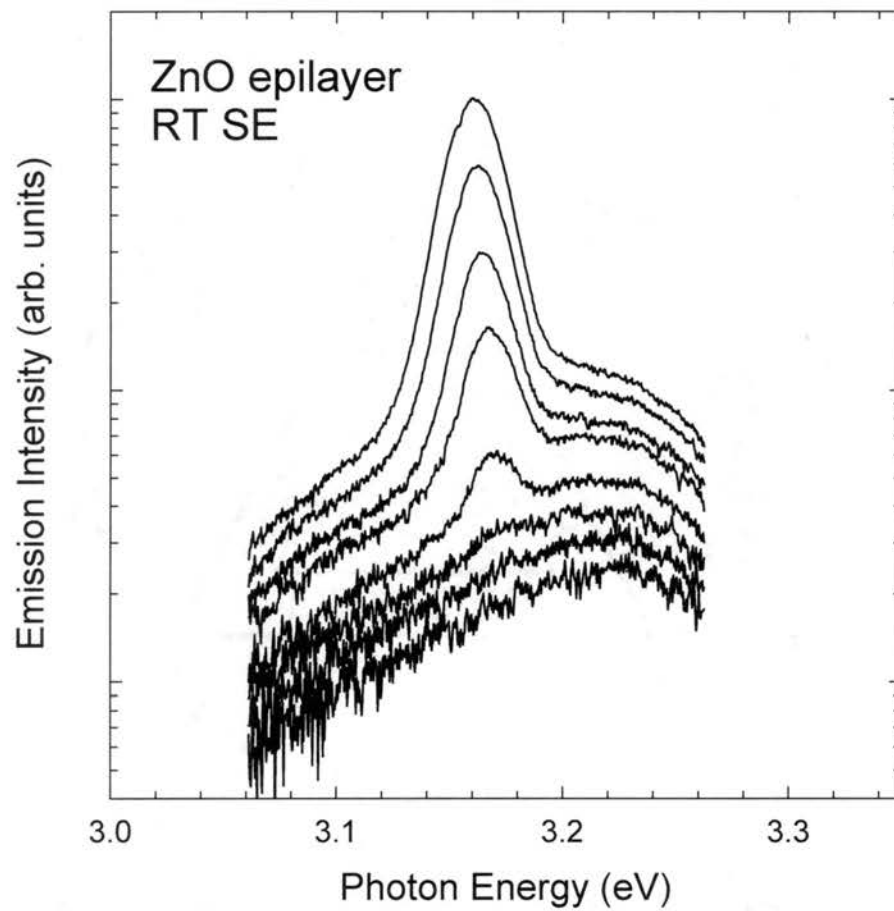


Figure 60. Spectra of ZnO epilayers at RT for several pumping intensities above and below the SE threshold.

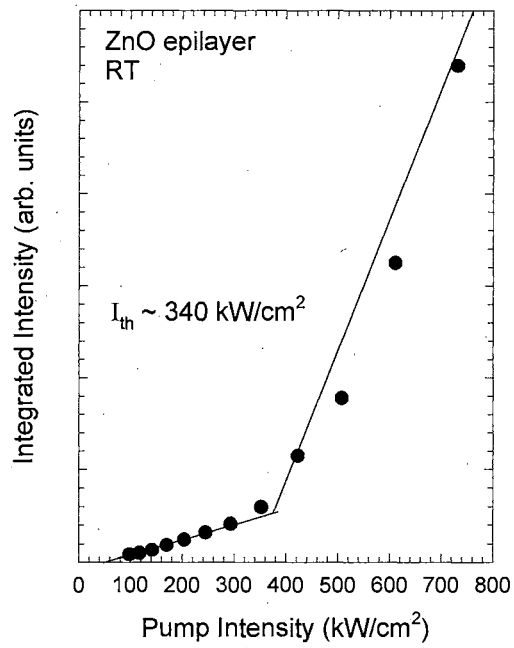
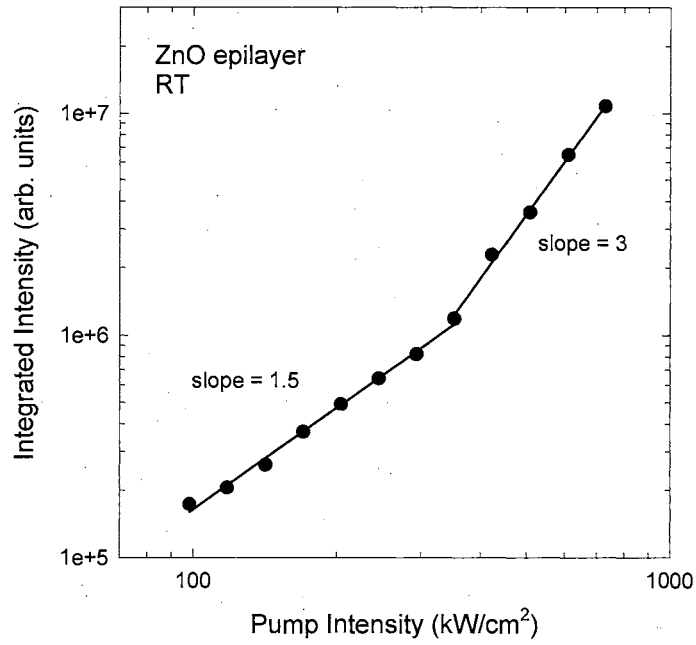


Figure 61. Integrated intensity of the RT emission from ZnO epilayers vs. pump intensity. SE, as seen by the superlinear increase in intensity, occurs above a threshold value of 340 kW/cm².

CHAPTER VII

SUMMARY

The wide bandgap III-Nitride and ZnO semiconductors are extremely important technological materials that will begin to have an ever-increasing influence on our daily lives in the very near future. Indeed, the author has seen a major transformation over the time period he has been in graduate school. From green LED traffic lights to full color outdoor LED displays to the blue LED dashboard backlighting in new Volkswagen automobiles, it is always fun to point at these engineering marvels that so many people take for granted and say, "That's what I do." In the very near future, there will be many more things at which to point, among them high-density optical storage devices (the next generation of DVDs), full color laser light shows, and white LED lighting. In addition, there are many up-and-coming applications of the III-Nitrides and ZnO that remain "hidden" from the general public, such as HFETs for use in high power electronics and wireless devices, as detectors and IR sources for use in telecommunications, as chemical and biological sensors, and medical uses.

In this manuscript, the author has hopefully demonstrated to the reader the paramount importance of the III-Nitrides and ZnO to the field of optoelectronics. We have described the past, current, and future state of research on these material systems, and have presented the author's contributions to the research community. These contributions will now be summarized in detail.

This manuscript, after providing a general background of the properties of semiconductors, the specific crystallographic properties of the III-Nitrides and ZnO, and an overview of the important growth and experimental characterization techniques used,

started by describing studies of excitons in the GaN. Using photoreflectance spectroscopy, we experimentally determined the binding energies for the *A*, *B*, and *C* excitonic transitions in GaN. We also estimated the reduced effective mass of the exciton. The influence of strain in GaN epilayers was investigated, yielding numerical values of the four principle deformation potentials. We demonstrated the novel use of photoconductivity measurements as a spectroscopic tool. By comparing the data with results from other experiments, we discovered that the excitonic transitions in the samples used were not associated with peaks in the PC spectra, but rather with the dips. By fitting the data obtained from these experiments, we determined the transition positions of the *A*, *B*, and *C* excitons.

Next, this thesis went on to describe studies of III-Nitride alloys and heterostructures. We used a variety of experimental techniques to study the properties of InGaN epilayers grown by MOCVD. We determined the bandgap energies for the samples studied, and determined that the low temperature PL emission was due to recombination involving impurity states and alloy potential fluctuations. The strong dependence of the PL decay time on temperature indicated that the trapping and recombination of photogenerated carriers at impurities and defect centers are dominant channels in determining the carrier population decay process. We studied the PL emission properties of AlGaIn and InGaIn alloys as a function of applied pressure. The pressure coefficients for these alloys were found, and it was determined that the near-bandedge emission observed in all the samples originates from the radiative decay of carriers localized in the band tail states of alloy potential fluctuations within the framework of the effective mass approximation. We studied the dynamics of photoexcited carriers in AlGaIn/GaN double heterostructures using picosecond time-resolved PL experiments. A model to explain the dynamics of the system, which included the generation, diffusion, spontaneous recombination, and nonradiative relaxation, was proposed. Using this model, we found values for the carrier capture time and the effective lifetimes of spontaneous recombination for carriers in GaN and AlGaIn. We further determined the diffusion constant and drift velocity for minority carriers in the AlGaIn cladding region. We studied the excitation wavelength dependence of stimulated emission/lasing from AlGaIn/GaN separate confinement heterostructures. We

observed extremely narrow single-mode lasing at both 10 K and RT. By studying the difference in energy positions of the lasing peaks with temperature as well as the narrowness of the emission line, we determined that lasing in the SCH samples is dominated by the exciton-exciton gain mechanism. We observed a decrease in the lasing threshold of the GaN active region when the sample was pumped into the AlGaN waveguide regions, due to the increased absorption cross-section and the efficient drift and diffusion of photoexcited carriers. We compared the emission of highly excited (In,Al)GaN thin films and heterostructures. The SE threshold of AlGaN epilayers was found to increase with increasing Al content compared to GaN, in contrast with InGaN epilayers, where an order of magnitude decrease is observed. RT SE was observed at remarkably short wavelengths, demonstrating that AlGaN-based structures are a suitable material for deep UV LDs. We achieved a substantial reduction in the lasing threshold for AlGaN/GaN-based heterostructures. We showed that optical and carrier confinement will play key roles in the reduction of the lasing threshold in these structures.

Finally, we studied the properties of bulk and epitaxially grown ZnO crystals through a combination of optical and structural characterization techniques. SE was observed in ZnO epilayers grown by MBE on sapphire using MgO buffer layers, and the threshold was determined. The PL spectra of both bulk and epilayers indicated an extremely high optical quality, and a number of sharp and narrow bandgap-related peaks were observed. By studying the slit-width dependence of full-width-at-half-maximum of the (0002) X-ray diffraction, we determined that the ZnO epilayers were single-crystal and of extremely high structural quality, whereas the bulk ZnO, while still of excellent quality, was multicrystalline. SE was observed from the epitaxial ZnO layers with a threshold intensity of 340 kW/cm^2 , but could not be seen in the bulk samples even at very large pump intensities. This is likely related to the multicrystalline nature of the bulk sample.

With this last paragraph, I bring the latest chapter of my life to a close. How to summarize the last 6 ½ years? Well, it's been real and it's been fun...

BIBLIOGRAPHY

1. S. Nakamura and G. Fasol, *The Blue Laser Diode*, (Springer, New York, 1997).
2. *GaN & Related Wide Bandgap Materials & Devices, 1998-2003*, 2nd edition, Elsevier Advanced Technology.
3. Y. Kitaoka, T. Yokoyama, K. Mizuuchi, and K. Yamamoto, *Jpn. J. Appl. Phys. Part 1* **39**, 3416 (2000).
4. J. Palmour, oral presentation at IEEE Cornell University Conference on “Advanced Concepts in High Performance Devices,” Ithaca, New York (2000).
5. *Wide-Bandgap Electronics*, III-Vs Review **13**, 38 (2000).
6. *Nitride News*, Compound Semiconductor **6**, 18 (2000).
7. J. I. Pankove, E. A. Miller, and J. E. Berkeyheiser, *RCA Rev.* **32**, 383 (1971).
8. H. Amano, N. Sawaki, I. Akasaki, and Y. Toyoda, *Appl. Phys. Lett.* **48**, 353 (1986).
9. S. Yoshida, S. Misawa, and S. Gonda, *Appl. Phys. Lett.* **42**, 427 (1983).
10. H. Amano, I. Akasaki, T. Kozawa, K. Hiramatsu, N. Sawaki, K. Ikeda, and Y. Ishii, *J. Lumin.* **40-48**, 121 (1988).
11. H. Amano, M. Kito, K. Hiramatsu, and I. Akasaki, *Jpn. J. Appl. Phys.* **28**, L2112 (1989).
12. S. Nakamura, N. Iwasa, M. Senoh, and T. Mukai, *Jpn. J. Appl. Phys.* **31**, 1258 (1992).
13. J. S. Foresi and T. D. Moustakas, *Appl. Phys. Lett.* **62**, 2859 (1993).
14. S. Nakamura, T. Mukai, and M. Senoh, *Jpn. J. Appl. Phys.* **30**, L1998 (1991).
15. S. Nakamura, T. Mukai, and M. Senoh, *J. Appl. Phys.* **76**, 8189 (1994).
16. S. Nakamura, M. Senoh, S. Nagahama, N. Iwasa, T. Yamada, Y. Matsushita, H. Kiyoku, and Y. Sugimoto, *Jpn. J. Appl. Phys. Part 1* **35**, L74 (1996).

17. A. Usui, H. Sunakawa, A. Sakai, and A. A. Yamaguchi, *Jpn. J. Appl. Phys. Part 2* **36**, L899 (1997).
18. O. H. Nam, M. D. Bremser, T. S. Zheleva, and R. F. Davis, *Appl. Phys. Lett.* **71**, 2638 (1997).
19. S. Nakamura, M. Senoh, S. I. Nagahama, H. Iwasa, T. Yamada, T. Matsushita, H. Kiyoku, Y. Sugimoto, T. Kozaki, H. Umemoto, M. Sano, and K. Chocho, *Appl. Phys. Lett.* **72**, 211 (1998).
20. J. A. Smart, E. M. Chumbes, A. T. Schremer, and J. R. Shealy, *Appl. Phys. Lett.* **75**, 3820 (1999).
21. D. I. Florescu, V. M. Asnin, F. H. Pollak, A. M. Jones, J. C. Ramer, M. J. Schurman, and I. Ferguson, *Appl. Phys. Lett.* **77**, 1464 (2000).
22. G. E. Bulman, K. Doverspike, S. T. Sheppard, T. W. Weeks, H. S. Kong, H. M. Dieringer, J. A. Edmond, J. D. Brown, J. T. Swindell, and J. F. Schetzina, *Electron. Lett.* **33**, 1556 (1997).
23. Cree Inc., press release from PR Newswire on July 29 (1997).
24. M. P. Mack, A. C. Abare, M. Aizcorbe, P. Kozodoy, S. Keller, U. K. Mishra, L. A. Coldren, and S. P. DenBaars, *MRS Internet J. Nitride Semiconductor Res.* **2**, 41 (1997).
25. R. K. Sink, A. C. Abare, P. Kozodoy, M. P. Mack, S. Keller, L. A. Coldren, S. P. DenBaars, and J. E. Bowers, *Mat. Res. Soc. Symp. Proc.* **482**, 1179 (1998).
26. A. Kuramata, K. Domen, and T. Tanahashi, *Appl. Phys. Lett.* **72**, 1359 (1998); Oral presentation at ICNS, Tokushima, Japan (1997).
27. F. Nakamura, oral presentation at ICNS, Tokushima, Japan (1997).
28. L. Sugiura, J. Nishio, M. Onomura, S. Nunoue, K. Itaya, and M. Ishikawa, *Mat. Res. Soc. Symp. Proc.* **482**, 1157 (1998).
29. M. Kneissl, D. P. Bour, N. M. Johnson, L. T. Romano, B. S. Krusor, R. Donaldson, J. Walker, and C. Dunnrowicz, *Appl. Phys. Lett.* **72**, 1539 (1998); M. Kneissl, D. P. Bour, L. T. Romano, C. G. van de Walle, J. E. Northrup, W. S. Wong, D. W. Treat, M. Teepe, T. Schmidt, and N. M. Johnson, *Appl. Phys. Lett.* **77**, 1931 (2000).
30. M. Koike, oral presentation at Photonics West, San Jose, California (2000).

31. *Nitride News*, Compound Semiconductor **5**, 12 (1999).
32. SDL, Inc., press release from PR Newswire on February 13 (1998).
33. W. W. Wenas, A. Yamada, K. Takahashi, M. Yoshino, and M. Konagai, *J. Appl. Phys.* **70**, 7119 (1991).
34. T. Detchprohm, K. Hiramatsu, H. Amano, and I. Akasaki, *Appl. Phys. Lett.* **61**, 2688 (1992).
35. Y. Sato and S. Sata, *Thin Solid Films* **281-282**, 445 (1996).
36. Y. Kanai, *Jpn. J. Appl. Phys. Part 1* **30**, 703 (1991).
37. K. Minegishi, Y. Koiwai, Y. Kikuchi, K. Yano, M. Kasuga, and A. Shimizu, *Jpn. J. Appl. Phys. Part 2* **36**, L1453 (1997).
38. T. Yamamoto and H. Katayama-Yoshida, *Jpn. J. Appl. Phys. Part 2* **38**, L166 (1999).
39. T. Aoki, Y. Hatanaka, and D. C. Look, *Appl. Phys. Lett.* **76**, 3257 (2000).
40. H. K. Kim, S. H. Han, T. Y. Seong, and W. K. Choi, *Appl. Phys. Lett.* **77**, 1647 (2000).
41. J. M. Hvam, *Solid State Commun.* **12**, 95 (1973).
42. D. M. Bagnall, Y. F. Chen, Z. Zhu, T. Yao, S. Koyama, M. Y. Shen, and T. Goto, *Appl. Phys. Lett.* **70**, 2230 (1997).
43. Z. K. Tang, G. K. L. Wong, P. Yu, M. Kawasaki, A. Ohtomo, H. Koinuma, and Y. Segawa, *Appl. Phys. Lett.* **72**, 3270 (1998).
44. H. Cao, Y. G. Zhao, H. C. Ong, S. T. Ho, J. Y. Dai, J. Y. Wu, and R. P. H. Chang, *Appl. Phys. Lett.* **73**, 3656 (1998).
45. G. P. Agrawal, *Fiberoptic Communications Systems*, 2nd edition, (Wiley & Sons, New York, 1997).
46. P. N. Favennec, H. L'Haridon, M. Salvi, D. Moutonnet, and Y. Le Guillou, *Electron. Lett.* **25**, 718 (1989).
47. K. Takahei and A. Taguchi, *J. Appl. Phys.* **74**, 1979 (1993).
48. R. N. Ghosh, J. Shumlovich, C. F. Kane, M. R. X. de Barros, G. Nykolak, A. J. Bruce, and P. C. Becker, *IEEE Photonics Technol. Lett.* **8**, 518 (1996).
49. D. Barbier, M. Rattay, F. Saint André, G. Clauss, M. Trouillon, A. Kevorkian, J. M. P. Delavaux, and E. Murphy, *IEEE Photonics Technol. Lett.* **9**, 315 (1997).

50. Y. C. Yan, A. J. Faber, H. de Waal, P. G. Kik, and A. Polman, *Appl. Phys. Lett.* **71**, 2920 (1997).
51. S. Komuro, T. Katsumata, T. Morikawa, X. Zhao, H. Isshiki, and Y. Aoyagi, *Appl. Phys. Lett.* **76**, 3935 (2000).
52. S. Itoh, H. Toki, Y. Sato, K. Morimoto, and T. Kishino, *J. Electrochem. Soc.* **138**, 1509 (1991).
53. Y. K. Park, J. I. Han, M. G. Kwak, H. Yang, S. H. Ju, and W. S. Cho, *Appl. Phys. Lett.* **72**, 668 (1998).
54. F. A. Ponce, in *Group III Nitride Semiconductor Compounds: Physics and Applications*, edited by B. Gil, (Clarendon Press, Oxford, 1998).
55. O. Madelung, editor, *Semiconductors – Basic Data*, 2nd edition, (Springer-Verlag, Berlin, 1996).
56. S. Sze, *Physics of Semiconductor Devices*, 2nd edition, (Wiley, New York, 1981).
57. K. Koga and T. Yamaguchi, *Progr. Crystal Growth Charact.* **23**, 127 (1991).
58. S. Yamaguchi, M. Kariya, S. Nitto, T. Takeuchi, C. Wetzel, H. Amano, I. Akasaki, *Appl. Phys. Lett.* **76**, 876 (2000).
59. T. Peng, J. Piprek, G. Qiu, J. O. Olowolafe, K. M. Unruh, C. P. Swann, E. F. Schubert, *Appl. Phys. Lett.* **71**, 2439 (1997).
60. F. G. McIntosh, K. S. Boutros, J. C. Roberts, S. M. Bedair, E. L. Piner, and N. A. El-Masry, *Appl. Phys. Lett.* **68**, 40 (1996).
61. M. E. Aumer, S. F. LeBoeuf, F. G. McIntosh, and S. M. Bedair, *Appl. Phys. Lett.* **75**, 3315 (1999).
62. S. R. Lee, A. F. Wright, M. H. Crawford, G. A. Peterson, J. Han, and R. M. Biefeld, *Appl. Phys. Lett.* **74**, 3344 (1999).
63. C. A. Parker, J. C. Roberts, S. M. Bedair, M. J. Reed, S. X. Liu, N. A. El-Masry, L. H. Robins, *Appl. Phys. Lett.* **75**, 2566 (1999).
64. M. C. McCluskey, C. G. van de Walle, C. P. Master, L. T. Romano, and N. M. Johnson, *Appl. Phys. Lett.* **72**, 2725 (1998).

65. M. A. Khan, J. W. Yang, G. Simin, R. Gaska, M. S. Shur, H. C. zur Loye, G. Tamulaitis, A. Zukauskas, D. J. Smith, D. Chandrasekhar, and R. Bicknell-Tassius, *Appl. Phys. Lett.* **76**, 1161 (2000).
66. A. Ohtomo, M. Kawasaki, T. Koida, K. Masubuchi, H. Koinuma, Y. Sakurai, Y. Yoshida, T. Yasuda, and Y. Segawa, *Appl. Phys. Lett.* **72**, 2466 (1998).
67. Y. Chen, H. J. Ko, S. K. Hong, and T. Yao, *Appl. Phys. Lett.* **76**, 559 (2000).
68. J. F. Sarver, F. L. Katnack, and F. A. Hummel, *J. Electrochem. Soc.* **106**, 960 (1959)
69. A. Ohtomo, R. Shiroki, I. Ohkubo, H. Koinuma, and M. Kawasaki, *Appl. Phys. Lett.* **75**, 4088 (1999).
70. C. W. Teng, J. F. Muth, U. Özgür, M. J. Bergmann, H. O. Everitt, A. K. Sharma, C. Jin, and J. Narayan, *Appl. Phys. Lett.* **76**, 979 (2000).
71. A. Ohtomo, M. Kawasaki, I. Ohkubo, H. Koinuma, T. Yasuda, and Y. Segawa, *Appl. Phys. Lett.* **75**, 980 (1999).
72. A. Ohtomo, K. Tamura, M. Kawasaki, T. Makino, Y. Segawa, Z. K. Tang, G. K. L. Wong, Y. Matsumoto, and H. Koinuma, *Appl. Phys. Lett.* **77**, 2204 (2000).
73. T. Makino, C. H. Chia, N. T. Tuan, Y. Segawa, M. Kawasaki, A. Ohtomo, K. Tamura, and H. Koinuma, *Appl. Phys. Lett.* **77**, 1632 (2000).
74. S. Bloom, G. Harbeke, E. Meier, and I. B. Ortenburger, *Phys. Stat. Solidi (b)* **64**, 161 (1974).
75. J. J. Song and W. Shan, in *Group III Nitride semiconductor compounds: physics and applications*, edited by B. Gil, (Clarendon Press, Oxford, 1998).
76. S. Kurai, T. Abe, Y. Naoi, and S. Sakai, *Topical Workshop on III-V Nitrides Abstracts*, Nagoya, B-6 (1995).
77. A. Gassmann, T. Suski, N. Newman, C. Kisielowski, E. Jones, E. R. Weber, Z. Liliental-Weber, M. D. Rubin, H. I. Helava, I. Grzegory, M. Bockowski, J. Jun, and S. Porowski, *J. Appl. Phys.* **80**, 2195 (1996).
78. C. Kirchner, V. Schwegler, F. Eberhard, M. Kamp, K. J. Ebeling, K. Kornitzer, T. Ebner, K. Thonke, R. Sauer, P. Prystawko, M. Leszczynski, I. Grzegory, and S. Porowski, *Appl. Phys. Lett.* **75**, 1098 (1999).

79. M. Suscavage, M. Harris, D. Bliss, P. Yip, S. Q. Wang, D. Schwall, L. Bouthillette, J. Bailey, M. Callahan, D. C. Look, D. C. Reynolds, R. L. Jones, and C. W. Litton, *MRS Internet J. Nitride Semicond. Res.* **4S1**, G3.40 (1999).
80. E. D. Kolb, R. Laudise, *J. Am. Ceram. Soc.* **48**, 342 (1965).
81. E. S. Hellman, D. N. E. Buchanan, D. Wiesmann, and I. Brener, *MRS Internet J. Nitride Semicond. Res.* **1**, 16 (1996).
82. G. B. Stringfellow, *Organometallic Vapor-Phase Epitaxy: Theory and Practice*, (Academic Press, San Diego, 1989).
83. D. Wood, *Optoelectronic Semiconductor Devices*, (Prentice Hall, New York, 1994).
84. M. B. Panish, I. Hayashi, and S. Sumski, *Appl. Phys. Lett.* **16**, 326 (1970).
85. S. L. Chuang, *Physics of Optoelectronic Devices*, (Wiley, New York, 1995).
86. Y. P. Varshni, *Physica* **34**, 149 (1967).
87. W. Shan, S. J. Hwang, J. J. Song, H. Q. Hou, and C. W. Tu, *Phys. Rev. B* **47**, 3765 (1993).
88. W. Shan, A. J. Fischer, S. J. Hwang, B. D. Little, R. J. Hauenstein, X. C. Xie, J. J. Song, D. S. Kim, B. Goldenberg, R. Horning, S. Krishnankutty, W. G. Perry, M. D. Bremser, and R. F. Davis, *J. Appl. Phys.* **83**, 455 (1998).
89. A. J. Fischer, W. Shan, J. J. Song, Y. C. Chang, R. Horning, and B. Goldenberg, *Appl. Phys. Lett.* **71**, 1981 (1997).
90. K. P. Korona, A. Wyszomolek, K. Pakula, R. Stepniewski, J. M. Baranowski, I. Grzegory, B. Lucznik, M. Wroblewski, and S. Porowski, *Appl. Phys. Lett.* **69**, 788 (1996).
91. D. E. Aspnes, in *Optical Properties of Solids*, edited by M. Balkanski, (North-Holland, Amsterdam, 1980).
92. V. B. Sandomirskii, *Fiz. Tverd. Tela.* **6**, 324 (1964) [*Sov. Phys. Solid State* **6**, 261 (1964)].
93. O. J. Glembocki and B. V. Shanabrook, *Superlattices Microstruct.* **5**, 235 (1987).
94. F. H. Pollak and O. J. Glembocki, *Proc. SPIE* **946**, 2 (1988).
95. H. Shen, S. C. Shen, F. H. Pollak, and R. N. Sacks, *Phys. Rev. B* **36**, 3487 (1987).

96. T. S. Moss, in *Semiconductors and Semimetals Vol. 2*, edited by R. K. Willardson and A. C. Beer, (Academic Press, New York, 1966).
97. H. B. DeVore, *Phys. Rev. B* **6**, 3750 (1956).
98. M. Parenteau, W. Fengmei, A. Jorio, C. Carlone, *J. Appl. Phys.* **77**, 5185 (1995).
99. M. I. Nathan, A. B. Fowler, and G. Burns, *Phys. Rev. Lett.* **11**, 152 (1963).
100. R. L. M. Voos and J. Shah, *Optical Properties of Solids*, edited by M. Balkanski, (North-Holland, Amsterdam, 1980).
101. S. Chichibu, A. Shikanai, T. Azuhata, T. Sota, A. Kuramata, K. Horino, and S. Nakamura, *Appl. Phys. Lett.* **68**, 3766 (1996).
102. D. G. Thomas and J. J. Hopfield, *Phys. Rev.* **116**, 573 (1959).
103. W. Shan, T. J. Schmidt, X. H. Yang, S. J. Hwang, J. J. Song, and B. Goldenberg, *Appl. Phys. Lett.* **66**, 985 (1995).
104. R. Dingle and M. Ilegems, *Solid State Commun.* **9**, 175 (1971).
105. R. Dingle, D. D. Sell, S. E. Stokowski, and M. Ilegems, *Phys. Rev. B* **4**, 1211 (1971).
106. B. Monemar, *Phys. Rev. B* **10**, 676 (1974).
107. B. Gil, O. Briot, and R. L. Aulombard, *Phys. Rev. B* **52**, R17028 (1995).
108. W. Shan, A. J. Fischer, J. J. Song, G. E. Bulman, H. S. Kong, M. T. Leonard, W. G. Perry, M. D. Bremser, and R. F. Davis, *Appl. Phys. Lett.* **69**, 740 (1996).
109. W. Shan, R. J. Hauenstein, A. J. Fischer, J. J. Song, W. G. Perry, M. D. Bremser, R. F. Davis, and B. Goldenberg, *Phys. Rev. B* **54**, 13460 (1996).
110. R. J. Elliot, *Phys. Rev.* **108**, 1384 (1957).
111. G. Mahler and U. Schröder, *Phys. Stat. Solidi (b)* **61**, 629 (1974).
112. S. Xu and X. Xie (unpublished).
113. K. N. Tu, J. W. Mayer, and L. C. Feldman, in *Electronic Thin Film Science*, (Macmillan, New York, 1992).
114. V. A. Savastenko and A. U. Sheleg, *Phys. Stat. Solidi (a)* **48**, K135 (1978).
115. G. L. Bir and G. E. Pikus, in *Symmetry and Strain-Induced Effects in Semiconductors*, (Wiley, New York, 1974).
116. E. F. Gross and B. V. Novikov, *Sov. Phys. Solid State* **1**, 321 (1959).

117. S. Strite and H. Morkoç, *J. Vac. Sci. Technol. B* **10**, 1237 (1992), and references therein.
118. J. I. Pankove, *Mat. Res. Soc. Symp. Proc.* **162**, 515 (1990), and references therein.
119. H. Morkoç, S. Strite, G. B. Gao, M. E. Lin, B. Sverdlov, and M. Burns, *J. Appl. Phys.* **76**, 1363 (1994).
120. S. Nakamura, M. Senoh, S. Nagahama, N. Iwasa, Y. Yamada, T. Matsushita, H. Kiyoku, and Y. Sugimoto, *Appl. Phys. Lett.* **68**, 2105 (1996).
121. H. Shen, S. H. Pan, F. H. Pollak, M. Dutta, and T. R. AuCoin, *Phys. Rev. B* **36**, 9384 (1987).
122. O. J. Glembocki and B. V. Shanabrook, in *Semiconductors and Semimetals Vol. 36*, edited by D. G. Seiler and C. L. Little, (Academic, New York, 1992).
123. F. H. Pollak and H. Shen, *Mater. Sci. Eng. R* **10**, 275 (1993).
124. A. F. Wright and J. S. Nelson, *Appl. Phys. Lett.* **66**, 3051 (1995).
125. M. Voos, R. F. Leheny, and J. Shah, in *Optical Properties of Solids*, edited by M. Balkanski, (North-Holland, Amsterdam, 1980).
126. L. Pavesi and M. Guzzi, *J. Appl. Phys.* **75**, 4779 (1994).
127. E. I. Rashba and G. E. Gurgenshvili, *Sov. Phys. Solid State* **4**, 759 (1962).
128. W. Shan, X. C. Xie, J. J. Song, and B. Goldenberg, *Appl. Phys. Lett.* **67**, 2512 (1995).
129. J. J. Song, W. Shan, T. J. Schmidt, X. H. Yang, A. J. Fischer, S. J. Hwang, B. Taheri, B. Goldenberg, R. Horning, A. Salvador, W. Kim, Ö. Aktas, A. Botchkarev, and H. Morkoç, *Proc. SPIE* **86** (1996).
130. S. Lai and M. V. Klein, *Phys. Rev. Lett.* **44**, 1087 (1980).
131. S. D. Baranovski and A. L. Efros, *Fiz. Tekh. Poluprovodn.* **12**, 2233 (1978) [*Sov. Phys. Semicond.* **12**, 1328 (1978)].
132. P. Perlin, I. Gorczyca, N. E. Christensen, I. Grzegory, H. Teisseyre, and T. Suski, *Phys. Rev. B* **45**, 13307 (1992).
133. W. Shan, T. J. Schmidt, R. J. Hauenstein, J. J. Song, and B. Goldenberg, *Appl. Phys. Lett.* **66**, 3495 (1995).

134. S. Kim, I. P. Herman, J. A. Tuchman, K. Doverspike, L. B. Rowland, and D. K. Gaskill, *Appl. Phys. Lett.* **67**, 380 (1995).
135. W. Shan, J. J. Song, Z. C. Feng, M. Schurman, and R. A. Stall, *Appl. Phys. Lett.* **71**, 2433 (1997).
136. N. E. Christensen and I. Gorczyca, *Phys. Rev. B* **50**, 4397 (1994).
137. P. Boguslawski, E. Briggs, and J. Bernholc, *Phys. Rev. B* **51**, 17255 (1995).
138. J. Neugebauer and C. G. van de Walle, *Phys. Rev. B* **50**, 8067 (1994).
139. P. Perlin, T. Suski, H. Teisseyre, M. Leszcynski, I. Grzegory, J. Jun, S. Porowski, P. Boguslawski, J. Bernholc, J. C. Chervin, A. Polian, and T. D. Moustakas, *Phys. Rev. Lett.* **75**, 296 (1995).
140. T. Suski, P. Perlin, H. Teisseyre, M. Leszcynski, I. Grzegory, J. Jun, S. Porowski, P. Boguslawski, J. Bernholc, J. C. Chervin, A. Polian, and T. D. Moustakas, *Appl. Phys. Lett.* **67**, 2188 (1995).
141. E. O. Göbel, H. Jung, J. Kuhl, and K. Ploog, *Phys. Rev. Lett.* **51**, 1588 (1983).
142. B. Deveaud, J. Shah, T. C. Damen, and W. T. Tsang, *Appl. Phys. Lett.* **52**, 1886 (1988).
143. P. W. M. Blom, C. Smit, J. E. M. Haverkort, and J. H. Wolter, *Phys. Rev. B* **47**, 2072 (1993).
144. S. Weiss, J. M. Wiesenfeld, D. S. Chemla, G. Raybon, G. Sucha, M. Wegener, G. Eisenstein, C. A. Burrus, A. G. Dentai, U. Koren, B. I. Miller, H. Temkin, R. A. Logan, and T. Tanbun-Ek, *Appl. Phys. Lett.* **60**, 9 (1992).
145. R. Nagarajan, R. P. Mirin, T. E. Reynolds, and J. E. Bowers, *Electron. Lett.* **29**, 1688 (1993).
146. C. I. Harris, B. Monemar, H. Amano, I. Akasaki, *Appl. Phys. Lett.* **67**, 840 (1995).
147. C. J. Hwang, *J. Appl. Phys.* **40**, 3731 (1969).
148. B. R. Nag, *Electron Transport in Compound Semiconductors*, (Springer, Berlin, 1980).
149. J. Crank, *The Mathematics of Diffusion*, 2nd edition, (Oxford University Press, New York, 1975).
150. S. Bidnyk, T. J. Schmidt, B. D. Little, and J. J. Song, *Appl. Phys. Lett.* **74**, 1 (1999).

151. S. Bidnyk, J. B. Lam, B. D. Little, Y. H. Kwon, J. J. Song, G. E. Bulman, H. S. Kong, and T. J. Schmidt, *Appl. Phys. Lett.* **75**, 3905 (1999).
152. I. Akasaki, S. Sota, H. Sakai, T. Tanaka, M. Koike, and H. Amano, *Electron. Lett.* **32**, 1105 (1996).
153. T. J. Schmidt, Y. H. Cho, J. J. Song, and W. Yang, *Appl. Phys. Lett.* **74**, 245 (1999).
154. S. Keller, A. C. Abare, M. S. Minsky, X. H. Wu, M. P. Mack, J. S. Speck, E. Hu, L. A. Coldren, U. K. Mishra, and S. P. DenBaars, *Mater. Sci. Forum* **264-268**, 1157 (1998).
155. S. Bidnyk, T. J. Schmidt, G. H. Park, and J. J. Song, *Appl. Phys. Lett.* **71**, 729 (1997).
156. Y. H. Cho, T. J. Schmidt, S. Bidnyk, J. J. Song, S. Keller, U. K. Mishra, and S. P. DenBaars, *Mat. Res. Soc. Symp. Proc.* **161**, G6.54 (1998).
157. S. Bidnyk, T. J. Schmidt, Y. H. Cho, G. H. Gainer, J. J. Song, S. Keller, U. K. Mishra, and S. P. DenBaars, *Appl. Phys. Lett.* **72**, 1623 (1998).
158. J. J. Song, A. J. Fischer, T. J. Schmidt, S. Bidnyk, and W. Shan, *Nonlinear Optics* **18** (2-1), 269 (1997).
159. D. C. Reynolds, D. C. Look, B. Jogai, and H. Morkoç, *Solid State Commun.* **101**, 643 (1997).
160. D. C. Reynolds, D. C. Look, B. Jogai, C. W. Litton, T. C. Collins, W. Harsch, and G. Cantwell, *Phys. Rev. B* **57**, 12151 (1998).

APPENDICES

APPENDIX A

PUBLICATIONS AND PRESENTATIONS

The following refereed scientific publications were generated from the material contained in this thesis:

- S. Bidnyk, S. K. Shee, J. B. Lam, G. H. Gainer, B. D. Little, Y. H. Kwon, J. J. Song, G. H. Park, S. J. Hwang, G. E. Bulman, and H. S. Kong, *Optical properties and lasing in (In,Al)GaN structures*, submitted to Phys. Stat. Sol. (b) (2000).
- C. K. Choi, Y. H. Kwon, B. D. Little, J. J. Song, Y. C. Chang, S. Keller, U. K. Mishra, and S. P. DenBaars, *Time-resolved photoluminescence study of InGaN/GaN multiple quantum well structures: Effect of Si doping in the barriers*, submitted to Phys. Rev. B (2000).
- S. K. Shee, Y. H. Kwon, J. B. Lam, G. H. Gainer, G. H. Park, S. J. Hwang, B. D. Little, and J. J. Song, *MOCVD growth, stimulated emission and time-resolved PL studies of InGaN/(In)GaN MQWs: well and barrier thickness dependence*, J. Crystal Growth, in press (2000).
- C. K. Choi, B. D. Little, Y. H. Kwon, J. B. Lam, J. J. Song, Y. C. Chang, S. Keller, U. K. Mishra, and S. P. DenBaars, *Femtosecond pump-probe spectroscopy and time-resolved photoluminescence of a highly excited InGaN epilayer*, submitted to Phys. Rev. B. (2000).

- S. Bidnyk, J. B. Lam, B. D. Little, G. H. Gainer, Y. H. Kwon, J. J. Song, G. E. Bulman, and H. S. Kong, *Microstructure-based lasing in GaN/AlGaN separate confinement heterostructures*, MRS Internet J. Nitride Semicond. Res. **5S1**, W11.22 (2000).
- J. B. Lam, S. Bidnyk, G. H. Gainer, B. D. Little, J. J. Song, and W. Yang, *Study of gain mechanisms in AlGaN in the temperature range of 30 to 300 K*, Appl. Phys. Lett. **77** (2000).
- S. Bidnyk, J. B. Lam, B. D. Little, G. H. Gainer, Y. H. Kwon, and J. J. Song, *Microstructure-based lasing in GaN/AlGaN separate confinement heterostructures*, Mat. Res. Soc. Symp. Proc. **595**, in press (2000).
- J. B. Lam, S. Bidnyk, G. H. Gainer, B. D. Little, J. J. Song, and W. Yang, *Study of gain mechanisms in $Al_xGa_{1-x}N$ in the temperature range of 30 to 300 K*, 2000 CLEO Technical Digest Series, **CMG1**, 33 (2000).
- S. Bidnyk, J. B. Lam, B. D. Little, G. H. Gainer, Y. H. Kwon, and J. J. Song, *Comparative study of near-threshold gain mechanisms in GaN epilayers and GaN/AlGaN separate confinement heterostructures*, SPIE Conf. Proc. **3947**, 24 (2000).
- S. Bidnyk, J. B. Lam, B. D. Little, Y. H. Kwon, J. J. Song, G. E. Bulman, and T. J. Schmidt, *Mechanism of efficient ultraviolet lasing in GaN/AlGaN separate confinement heterostructures*, Appl. Phys. Lett. **75**, 3905 (1999).
- S. Bidnyk, B. D. Little, J. J. Song, and T. J. Schmidt, *A technique for evaluating optical confinement in GaN-based lasing structures*, Appl. Phys. Lett. **75**, 2163 (1999).
- S. Bidnyk, T. J. Schmidt, B. D. Little, and J. J. Song, *Evaluation of optical confinement in GaN-based lasing structures*, Phys. Stat. Sol. (b) **216**, 1 (1999).

- S. Bidnyk, T. J. Schmidt, B. D. Little, J. Krasinski, and J. J. Song, *Novel technique for evaluation of optical confinement in semiconductor laser structures through spatially and spectrally resolved emission spectra*, 1999 CLEO Technical Digest Series, **CTuK52**, 145 (1999).
- B. D. Little, S. Bidnyk, T. J. Schmidt, J. B. Lam, Y. H. Kwon, J. J. Song, S. Keller, U. K. Mishra, S. P. DenBaars, W. Yang, *Comparative study of emission from highly excited (In,Al)GaN thin films and heterostructures*, Mat. Res. Soc. Symp. Proc. **572**, 351 (1999).
- S. Bidnyk, T. J. Schmidt, B. D. Little, J. J. Song, *Study of near-threshold gain mechanisms in MOCVD-grown (In,Al)GaN epilayers and heterostructures*, Mat. Res. Soc. Symp. Proc. **572**, 439 (1999).
- A. J. Fischer, B. D. Little, T. J. Schmidt, J. J. Song, R. Horning, and B. Goldenberg, *Ultrafast carrier dynamics in GaN epilayers studied by femtosecond pump-probe spectroscopy*, SPIE Conf. Proc. **3624**, 179 (1999).
- S. Bidnyk, T. J. Schmidt, B. D. Little, J. J. Song, *Near-threshold gain mechanisms in GaN thin films in the temperature range of 20-700 K*, Appl. Phys. Lett. **74**, 1 (1999).
- S. Bidnyk, B. D. Little, T. J. Schmidt, Y. H. Cho, J. J. Song, B. Goldenberg, W. G. Perry, M. D. Bremser, and R. F. Davis, *Stimulated emission in thin GaN films in the temperature range of 300 K to 700 K*, J. Appl. Phys. **85**, 1794 (1999).
- Y. H. Cho, B. D. Little, G. H. Gainer, J. J. Song, S. Keller, U. K. Mishra, and S. P. DenBaars, *Carrier dynamics of abnormal temperature-dependent emission shift in MOCVD-grown InGaN epilayers and InGaN/GaN multiple quantum wells*, MRS Internet J. Nitride Semicond. Res. **4S1**, G2.4 (1999).
- S. Bidnyk, T. J. Schmidt, B. D. Little, J. Krasinski, J. J. Song, S. Keller, and S. P. DenBaars, *Comparative study of near-threshold stimulated emission mechanisms*

in GaN epilayers and InGaN/GaN multiquantum wells, SPIE Conf. Proc. **3625**, 68 (1999).

- S. Bidnyk, B. D. Little, Y. H. Cho, J. Krasinski, J. J. Song, W. Yang, S. A. McPherson, *Laser action in optically pumped GaN pyramids grown on (111) silicon by selective lateral overgrowth*, MRS Internet J. Nitride Semicond. Res. **4S1**, G6.48 (1999).
- S. Bidnyk, B. D. Little, Y. H. Cho, J. Krasinski, J. J. Song, W. Yang, S. A. McPherson, *Laser action in optically pumped GaN pyramids grown on (111) silicon by selective lateral overgrowth*, Mat. Res. Soc. Symp. **537**, G6.48 (1998).
- S. Bidnyk, B. D. Little, Y. H. Cho, J. Krasinski, J. J. Song, W. Yang, and S. A. McPherson, *Laser action in GaN pyramids grown on (111) silicon by selective lateral overgrowth*, Appl. Phys. Lett. **73**, 2242 (1998).
- S. Bidnyk, B. D. Little, T. J. Schmidt, J. Krasinski, and J. J. Song, *High-temperature stimulated emission studies of MOCVD-grown GaN films*, Proceedings of the SPIE Conference on Optoelectronic Materials and Devices **3419**, 35 (1998).
- W. Shan, W. Walukiewicz, E. E. Haller, B. D. Little, J. J. Song, M. D. McCluskey, N. M. Johnson, Z. C. Feng, M. Schurman, and R. A. Stall, *Optical properties of $In_xGa_{1-x}N$ alloys grown by metalorganic chemical vapor deposition*, J. Appl. Phys. **84**, 4452 (1998).
- W. Shan, J. W. Ager III, W. Walukiewicz, E. E. Haller, B. D. Little, J. J. Song, M. Schurman, Z. C. Feng, R. A. Stall, and B. Goldenberg, *Near-band-edge photoluminescence emission in $Al_xGa_{1-x}N$ under high pressure*, Appl. Phys. Lett. **72**, 2274 (1998).
- W. Shan, A. J. Fischer, S. J. Hwang, B. D. Little, R. J. Hauenstein, X. C. Xie, J. J. Song, D. S. Kim, B. Goldenberg, R. Horning, S. Krishnankutty, W. G. Perry, M.

- D. Bremser, and R. F. Davis, *Intrinsic exciton transitions in GaN*, J. Appl. Phys. **83**, 455 (1998).
- W. Shan, J. W. Ager III, W. Walukiewicz, E. E. Haller, B. D. Little, J. J. Song, B. Goldenberg, Z. C. Feng, M. Schurman, and R. A. Stall, *High pressure study of III-Nitrides and related heterostructures*, Mat. Res. Soc. Symp. Proc. **499**, 361 (1997).
 - J. J. Song, W. Shan, B. D. Little, X. C. Xie, G. E. Bulman, and S. Krishnankutty, *Dynamics study of minority carrier diffusion in $Al_xGa_{1-x}N/GaN$ heterostructures*, Proceedings of the 1997 International Congress on Nitride Semiconductors (ICNS), Tokushima, Japan, October 27-31 (1997).
 - W. Shan, S. Xu, B. D. Little, X. C. Xie, J. J. Song, G. E. Bulman, H. S. Kong, M. T. Leonard, and S. Krishnankutty, *Dynamics of photoexcited carriers in $Al_xGa_{1-x}N/GaN$ double heterostructures*, J. Appl. Phys. **82**, 3158 (1997).
 - B. D. Little, W. Shan, J. J. Song, Z. C. Feng, M. Schurman, and R. A. Stall, *Optical studies of MOCVD $In_xGa_{1-x}N$ alloys*, Mat. Res. Soc. Symp. Proc. **449**, 823 (1997).
 - W. Shan, B. D. Little, A. J. Fischer, and J. J. Song, *Binding energy for the intrinsic excitons in wurtzite GaN*, Phys. Rev. B **54**, 369 (1996).
 - W. Shan, B. D. Little, and J. J. Song, *Optical transitions in $In_xGa_{1-x}N$ alloys grown by metalorganic chemical vapor deposition*, Appl. Phys. Lett. **69**, 3315 (1996).

The author has presented the research contained in this thesis at the following conferences:

- *MOCVD growth, stimulated emission and time resolved PL studies of InGaN/(In)GaN MQWs: well and barrier thickness dependence*, oral presentation at the Tenth International Conference on Metalorganic Vapor Phase Epitaxy (ICMOVPE-X), Sapporo, Japan, June 5-9, 2000.
- *Comparative study of emission from highly excited InGaN, GaN, and AlGaN thin films*, oral presentation at the Materials Research Society Spring 1999 Meeting, San Francisco, CA, April 5-9, 1999.
- *Room temperature deep ultraviolet stimulated emission from MOCVD-grown AlGaN thin films on sapphire*, oral presentation at the American Physical Society 1999 March Meeting, Atlanta, GA, March 17-21, 1999.
- *Excitation wavelength dependence of stimulated emission from AlGaN epilayers*, oral presentation at the American Physical Society 1999 March Meeting, Atlanta, GA, March 17-21, 1999.
- *Carrier dynamics of abnormal temperature-dependent emission shift in MOCVD-grown InGaN epilayers and InGaN/GaN multiple quantum wells*, oral presentation at the Materials Research Society Fall 1998 Meeting, Boston, MA, November 29 - December 4, 1998.
- *Time-resolved luminescence study of dynamics of photoexcited carriers in GaN/AlGaN double heterostructures*, oral presentation at the American Physical Society 1997 March Meeting, Kansas City, MO, March 17-21, 1997.
- *Optical studies of MOCVD $In_xGa_{1-x}N$ alloys*, poster presentation at the Materials Research Society Fall 1996 Meeting, Boston, MA, December 2-6, 1996.

APPENDIX B

LASER INDUCED EPITAXIAL LIFTOFF

In recent years, much research has been performed on the group-III Nitrides and their alloys due to their wide direct bandgaps, which make them promising materials for the development of light emitting and detecting devices operating in the UV-blue spectral region. Currently, the best material properties have been realized by utilizing (0001) sapphire as a substrate. However, epitaxial growth of (In,Al)GaN on sapphire has several significant drawbacks. 1) Only the top surface of the sample can be processed for device applications. For LEDs, this results in a smaller effective emission area due to the absorptive nature of the metallic contacts. For LDs, a mesa structure is usually required, in which large amounts of the sample must be etched away to create the edge-emitting facets and the bottom contact. 2) The cleave planes of the sapphire substrate and the overlying nitride material do not coincide. Thus the sapphire inhibits the cleaving of the epilayer to make high-quality laser cavities. Instead, complicating etching procedures must be employed.

Several groups have recently shown that it is possible to separate nitride epilayers and heterostructures from sapphire substrates using high power pulsed UV radiation from an excimer laser¹ or a wavelength-tripled Nd:YAG laser.² Pieces of the sample are mounted to a host substrate leaving the sapphire, which is transparent to the UV laser wavelength, exposed. Laser light is focused through the sapphire onto the nitride-sapphire interface region samples where it is absorbed. The interface is locally heated to

¹ W. S. Wong, T. Sands, and N. W. Cheung, *Appl. Phys. Lett.* **72**, 599 (1998).

² M. K. Kelly, O. Ambacher, R. Dimitrov, R. Handschuh, and M. Stutzmann, *Phys. Stat. Sol. (a)* **159**, R3 (1997).

temperatures above 800°C, at which GaN begins to decompose into metallic Ga and N₂ gas. To reach such high temperatures, the power density of the absorbed laser light must be in the range of 400-600 mJ/cm². These removed nitride layers have been shown to be of high quality both structurally and chemically.³ The liftoff procedure is shown graphically in Figure B-1.

As the laser induced epitaxial liftoff procedure got more attention due to its applicability in optoelectronic device production, more research began to be published on this technique. As of the writing of this thesis, four research groups had shown the ability to perform this procedure. From the original publications dealing with separation of GaN epilayers on sapphire, the technique has expanded to include resonant cavity InGaN quantum well blue LEDs bonded to Cu host substrates⁴ and InGaN LEDs on Si substrates fabricated by Pd-In metal bonding.⁵ Kelly *et al* recently published results illustrating the removal of an entire 2-inch diameter wafer of 275 μm-thick HVPE-grown GaN from the underlying sapphire substrate.⁶ In addition, several interesting studies have been performed using the results of this technique rather than the technique itself. Perlin *et al* compared the pressure coefficients for the energy gap of epitaxial GaN on sapphire and free-standing films produced by the laser liftoff technique. They found that the presence of sapphire leads to a reduction in the pressure coefficient of approximately 5%.⁷ Miskys *et al* have grown homoepitaxial GaN on top of free-standing 300 μm-thick GaN films that were removed from their sapphire substrate. They found that the epitaxially grown layers were of extremely high quality, characterized by a narrow FWHM in XRD and low dislocation densities as determined through AFM measurements.⁸ Finally, one paper has been published on the laser liftoff technique in a material system other than the III-Nitrides. Tavernier *et al* successfully removed ZnO epilayers grown by PLD on sapphire

³ E. A. Stach, M. Kelsch, E. C. Nelson, W. S. Wong, T. Sands, and N. W. Cheung, *Appl. Phys. Lett.* **77**, 1819 (2000).

⁴ Y. K. Song, M. Diagne, H. Zhou, A. V. Nurmikko, R. P. Schneider, Jr., and T. Takeuchi, *Appl. Phys. Lett.* **77**, 1744 (2000).

⁵ W. S. Wong, T. Sands, N. W. Cheung, M. Kneissl, D. P. Bour, P. Mei, L. T. Romano, and N. M. Johnson, *Appl. Phys. Lett.* **77**, 2822 (2000).

⁶ M. K. Kelly, R. P. Vaudo, V. M. Phanse, L. Görgens, O. Ambacher, and M. Stutzmann, *Jpn. J. Appl. Phys. Part 2* **38**, L217 (1999).

⁷ P. Perlin, L. Mattos, N. A. Shapiro, J. Kruger, W. S. Wong, T. Sands, N. W. Cheung, E. R. Weber, *J. Appl. Phys.* **85**, 2385 (1999).

⁸ C. R. Miskys, M. K. Kelly, O. Ambacher, G. Martinez-Criado, and M. Stutzmann, *Appl. Phys. Lett.* **77**, 1858 (2000).

substrates as well as GaN epilayers grown by HVPE on sapphire. They observed a broadening of the ZnO PL signal after removal, indicating the presence of additional defects induced by the liftoff technique, but did not observe a similar phenomenon in GaN.⁹ This is due to the fact that ZnO has a lower defect formation energy than GaN.

We have successfully separated GaN epilayers from their sapphire substrates. The $\sim 2 \mu\text{m}$ thick epilayers were grown on (0001) sapphire by MOCVD. The epilayer sides of the 2×3 mm samples were mounted to a glass slide using five-minute epoxy. The 308 nm laser light from a XeCl excimer laser was focused through the substrate onto the sapphire-GaN interface. At pump fluences above $\sim 500 \text{ mJ/cm}^2$, a single pulse of laser light removed the substrate. Metallic gallium deposits were visible both on the removed substrate and the bonded epilayer. This was easily removed by an HCl bath.

⁹ P. R. Tavernier, P. M. Verghese, and D. R. Clarke, *Appl. Phys. Lett.* **74**, 2678 (1999).

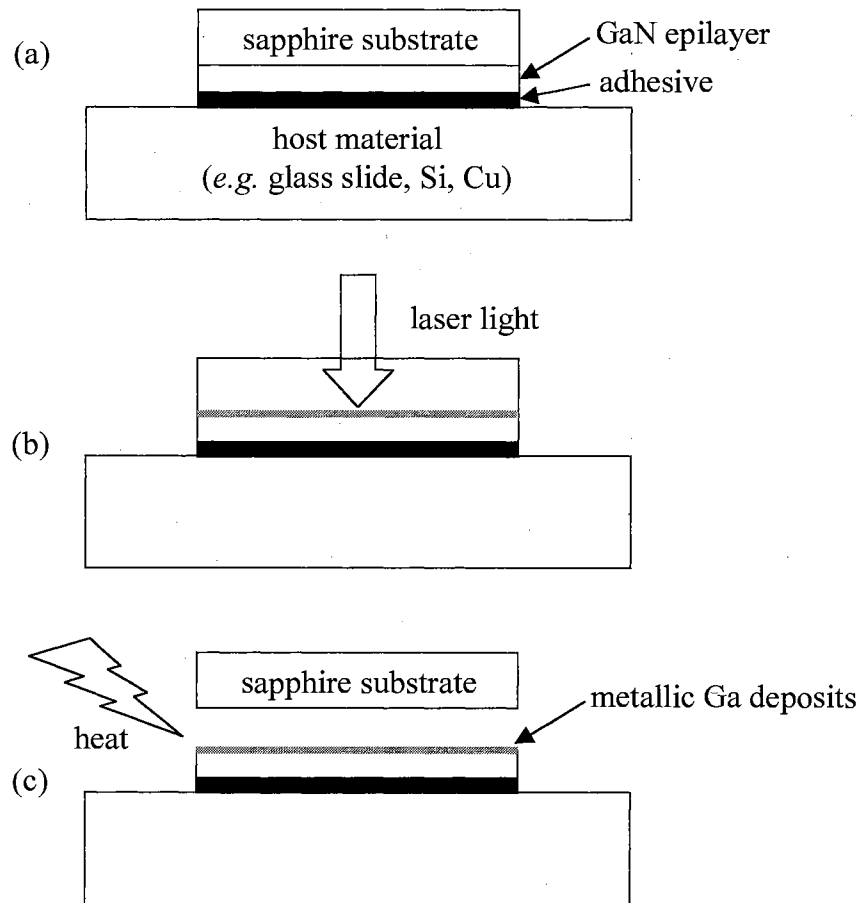


Figure B-1. Illustration of the laser induced epitaxial liftoff process for GaN on sapphire. (a) The sample is mounted to a host substrate (sapphire side up) with an adhesive. (b) High intensity UV laser radiation is sent through the substrate and is absorbed at the GaN/sapphire interface, locally heating the epilayer to a temperature at which it decomposes. (c) After melting any remaining Ga from the interface, the substrate is removed. Excess metallic deposits are easily removed in an HCl bath, and if desired, the epilayer can be removed from the host substrate by dissolving the solvent with the appropriate solvent.

VITA^a

Brian Dean Little

Candidate for the Degree of

Doctor of Philosophy

Thesis: OPTICAL PROPERTIES OF WIDE BANDGAP III-NITRIDE- AND ZINC OXIDE-BASED EPILAYERS, ALLOYS, AND HETEROSTRUCTURES

Major Field: Physics

Biographical:

Personal Data: Born in Hot Springs, Arkansas, on May 25, 1972, the son of Joe and Mary Little.

Education: Graduated from Hot Springs High School, Hot Springs, Arkansas in June 1990; received Bachelor of Arts degree in Physics (cum laude with distinction) from Hendrix College, Conway, Arkansas, June 1994; obtained a Master of Science Degree in Photonics from Oklahoma State University, Stillwater, Oklahoma in December 1997. Completed the requirements for the Doctor of Philosophy Degree with a major in Physics at Oklahoma State University in December 2000.

Professional Experience: Employed by Oklahoma State University, Center for Laser and Photonics Research and Department of Physics as a graduate research assistant, August 1994 to December 2000.

Professional Memberships: American Physical Society, American Vacuum Society, Optical Society of America, Materials Research Society.